DE GRUYTER OPEN

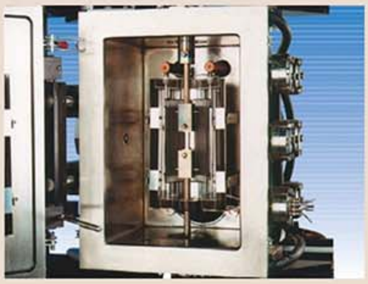

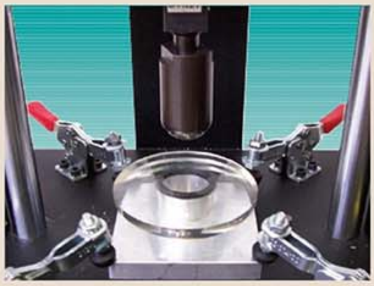

The Scientific Bulletin of Valahia University MATERIALS and MECHANICS

2017

Vol. 15 No. 13

DE GRUYTER OPEN

The Scientific Bulletin of VALAHIA University
MATERIALS and MECHANICS –Vol. 15, No. 13

DOI 10.1515/bsmm-2017-0011

STUDY OF 7075 ALUMINIUM ALLOY JOINTS

Ildiko PETER[*1] **, Mario ROSSO**[1]

Department of Applied Science and Technology, Politecnico di Torino
Corso Duca degli Abruzzi 24
10129 Torino, Italy

E-mail[*]: ildiko.peter@polito.it

Abstract. *High-strength EN AW 7075 Al-based alloy (Al-Zn-Mg-Cu) is currently employed in many industrial fields where excellent mechanical performances of structural components are required. In contrast to the many positive features this alloy presents, it is not fusion weldable, because it is subjected to solidification and liquation cracking. In this paper, the possibility to weld low thickness plates, made of 7075 aluminum alloy, by the tungsten inert gas welding technique will be presented. Two types of welding have been performed: for the former one, welding involves only one surface, while for the second one, welding has been carried out on both faces of the plates. After welding, microstructural analysis and mechanical properties investigations have been carried out. The present research highlights that the mechanical properties evolution is affected by the welding procedure. In particular, the mechanical strength reached for the samples welded on both faces, in the proposed setting, is comparable to that of the un-welded alloys.*

Keywords: *EN AW 7075 Al-based alloy, tungsten inert gas welding technique*

1. INTRODUCTION

Due to the precipitation of Mg_2Zn and Al2CuMg phases 7075 aluminum alloy presents good machinability, mainly high mechanical strength and specific stiffness [1-3], which makes it suitable for the fabrication of structural components for aerospace and automotive industries. Due to its chemical composition this alloy is susceptible to various forms of localized corrosion [4-6]. In particular, the presence of many different constituents, define the heterogeneity, which plays a crucial role in influence the corrosion resistance. Another important limitation of this alloy concerns its weldability, because of the content of copper, the wide range of solidification temperature and the low solidus temperature [2-7-8] it can not be welded be welding fusion techniques. This because 7xxx as 2xxx series of aluminum alloys are sensitive to hot cracking [8], and solidification and liquation cracking [9]. During the solidification of weld metal solidification cracking can occur in the fusion zone, while for as regard the liquation cracking, it can takes place in the partially melted zone during the solidification of the liquated metal. So recently many solid-state welding process, such as friction welding and friction stir welding, have been widely studied and developed [7-8-10-11-12-13]. In these processes parts to be joined are rotated against each other, while applying some axial force (friction force). These welding processes, with respect to the tradition fusion welding techniques, allow to reduce residual stresses and distortion caused by the welding process [10] and are characterized by the absence of voids and cracking in the weld and no filler material is necessary. However, their most important feature is that melting and solidification are not involved and there are not creates any problems in terms of solidification and liquation cracking. Nevertheless, in these processes is extremely important to control carefully three welding parameters: tool's rotation speed, welding speed and welding pressure. Inadequate control and setting of these parameters can determine defects in the joint and deteriorate the mechanical properties of the joints [14].

In the present paper the effect of single and double welding pass on the microstructure and the mechanical properties on Tungsten Inert Gas welded 7075 aluminum alloy joints have been investigated and presented.

2. EXPERIMENTAL PROCEDURE

Samples with a single or a double welding pass have been realized in order to evaluate the effect of different welding passes on both the microstructure and the mechanical properties of the 7075 aluminum alloy. Argon has been used as shielding gas. The microstructure of the samples, prepared by a standard metallographic technique by mounting and polishing procedures, has been investigated using an optical microscope, (OM, MeF4 Reichart-Jung) and Scanning Electron Microscopy (SEM, Leo 1450VP) equipped with Energy X-rays Dispersive Spectroscopy unit (EDS, Oxford microprobe) used for compositional analysis. Vickers micro-hardness test have been performed, using an applied load of 500 gf and a time of load application equal to 15 s. Hardness has been measured in numerous points from the weld center line along the heat affected zone to the base metal. Tensile tests have been carried out, according to the UNI EN ISO 4136 Standard. Finally, by fracture surface analysis, some causes related to the samples failure can be determined.

Table 1. Chemical composition (wt%) of the 7075 alluminum alloy

Elements	Chemical composition (wt%)
Zn	5.6
Mg	2.5
Cu	1.5
Mn	0.04
Fe	0.3
Si	0.08
Al	bal.

3. RESULTS AND DISCUSSION

3.1 Microstructural analysis

Figures 1 and 2 report the optical micrographs of the welded joints obtained by single and double welding pass.

Both the two types of joints show similar microstructure in all the typical zones: fusion zone (FZ), heat affected zone (HAZ) and finally in the base metal (BM). The fusion zone shows a fine and equiaxed microstructure, due to the fast cooling rate, to which is subjected during the welding and the following solidification process. The heat affected zone has a coarser microstructure because it is submitted to higher peak temperatures. In the HAZ not only the grain coarsening occurs, but also other important phenomenon takes place, such as the dissolution of precipitates and the transformation of precipitates from metastable phase to a stable one.

3.2 Mechanical characterization

Vickers micro-hardness profiles are reported in Fig. 3. For both type of welded plates, the hardness profile shows four different areas: FZ, HAZ I, HAZ II and the base metal, as discussed below. The fusion zone reveals the lowest Vickers micro-hardness values because in this area the straightening precipitates are not present. In the HAZ I zone, where a slow increase of hardness value is observable, only the Guinier-Preston (GP) zones are present, which are clusters that contain a high fraction of solute atoms. In the other zone, HAZ II, a sharp increase of hardness value has been obtained, due to the partial dissolution of the initially present precipitates, and furthermore to the transformation of metastable phases to more stable forms [8]. Finally, the base metal zone, as expected, has the highest hardness values, since it is unaffected by the welding process. Plates welded on both faces show a slightly higher hardness value in the heat affected zones compared to the plates welded on only one face.

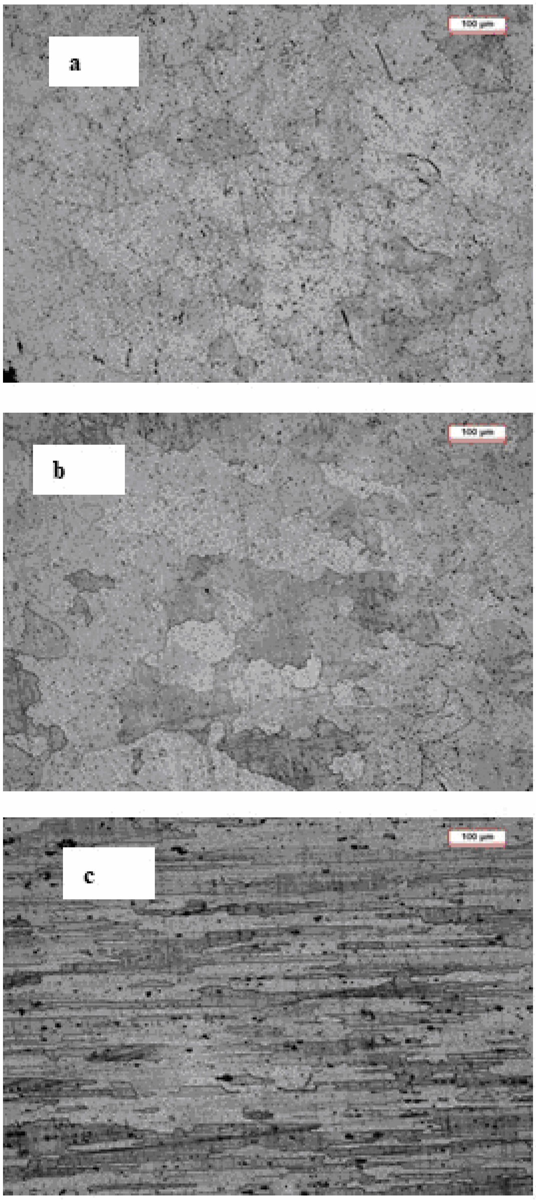

Figure 1. Optical micrographs of single pass welded joints: a) fusion zone, b) heat affected zone and c) base metal

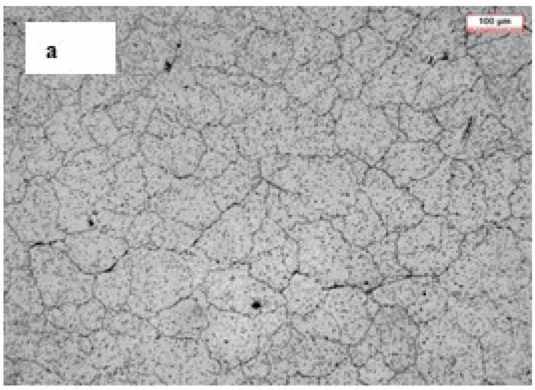

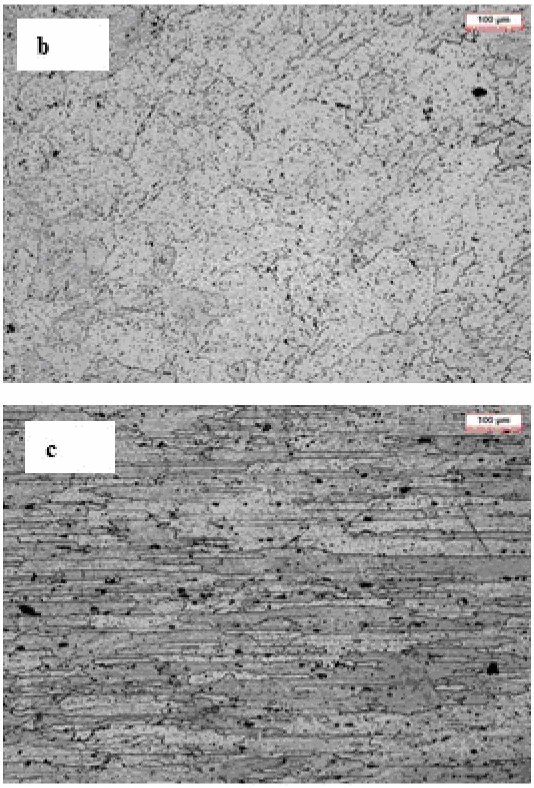

Figure 2. Optical micrographs of the double pass welded joints: a) fusion zone, b) heat affected zone and c) base metal

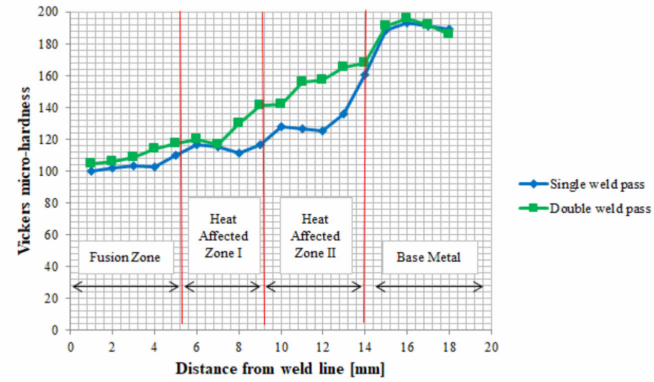

Figure 3. Vickers micro-hardness profiles on the cross section of samples welded by single and double welding pass

The obtained average results of the tensile test are summarized in Table 1. The obtained results are compared to those obtained for the base T6 heat treated 7075 aluminum alloy with no welding. The plates welded on both faces show high mechanical strength, in terms of the ultimate tensile strength, yield strength, Young's modulus and elongation to fracture. The plates welded on only one face have very low mechanical properties caused by the uncompleted welding penetration; actually only about 50% of the cross section has been welded (Fig. 4a). On the contrary, the plates welded on both faces, as reported in Fig. 4b, show a completely welded cross section and can be correlate to their good mechanical performances, which are comparable with those related to the base 7075 un-welded alloy.

For the plates welded on only one face many defects occur: very long cracks and gas porosities are developed (Fig.5a and Fig.5b), which have a harmful impact on the mechanical strength of the plates. In the plates welded by TIG welding process on both faces, the development of some gas porosities involves only a small area close to the external surface (Fig.5c) and as localized defect do not affect negatively the whole behavior of the material. The plates welded on both faces reveal high mechanical strength, without the need to apply a post-weld aging treatment or a post-weld natural ageing, which are generally applied, after the welding process, to recover the mechanical properties [8, 16].

The low gas porosity content can be correlated to the delay of solidification obtained by increasing the temperature by the second welding pass realized, in line with [16, 18], provides enough time for the growth of the gas bubbles, which can overflow before the complete solidification. Using a laser-arc hybrid welding process in [16], comparable results have been reached. According to the delayed solidification, the plates welded on both faces are characterized by an average grain size of about 171.54 µm, around 20% higher than that presented by samples welded on only one face (139.78 µm).

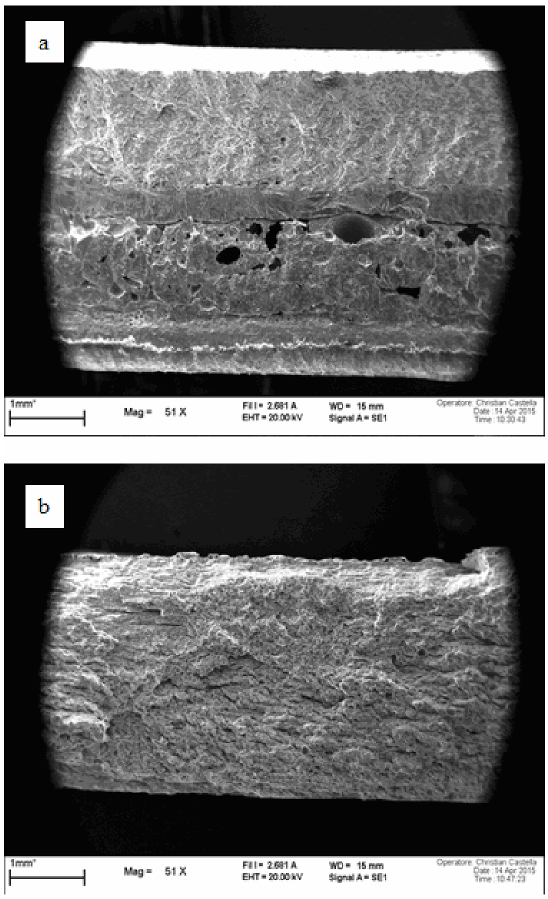

Figure 4. SEM images of the fractured surface of: a) plates welded on only one face and b) plates welded on both faces

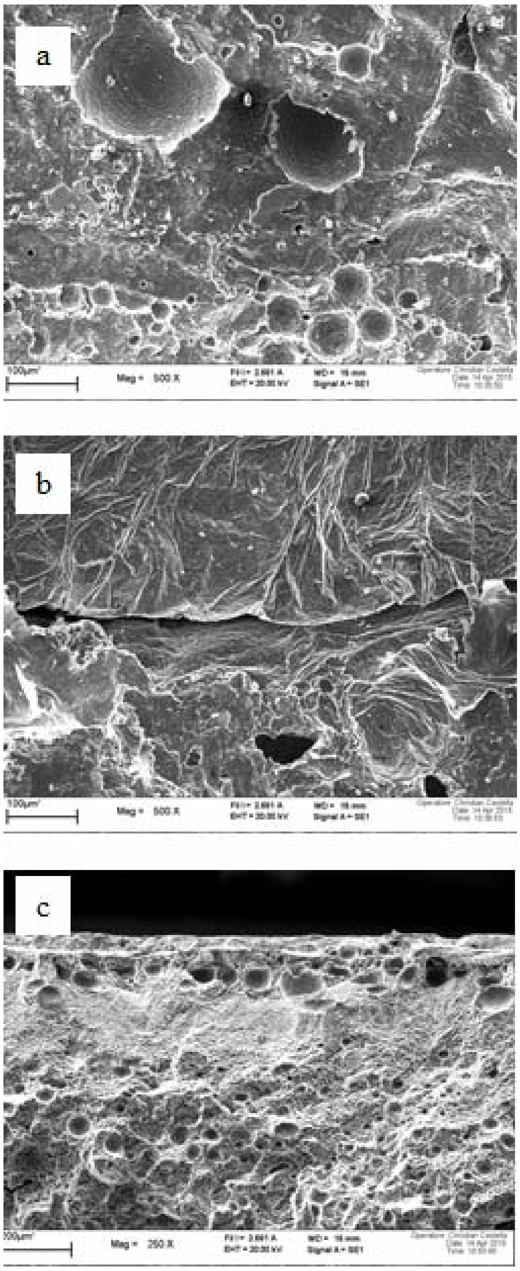

Figure 5. SEM micrographs showing: long crack development (a) and many gas porosities (b) on the plate welded on only one face and gas porosities, detected in a small area close to the external surface, in the plates welded on both faces (c)

4. CONCLUSIONS

In this paper, low thickness plates of about 3 mm made of 7075 aluminum alloy were joined by Tungsten Inert Gas welding process. Two types of samples were obtained and analyzed: (i) welding was realized on only one face and (ii) some other samples were obtained welding them on both faces. Microstructural analysis and mechanical properties evaluation were carried out and the obtained results are very promising. The fusion zone, in both type of samples, reveals a fine and equiaxed microstructure, due to the fast cooling rate to which it is subjected, while the heat affected zone has a coarser microstructure because it is submitted to higher peak temperatures. The plates welded on both faces reveal higher mechanical properties compared to those welded on only one face and their cross section are completely welded containing only few gas porosities individuated close to the external surfaces The low gas porosity content was correlated to the delay of. Many defects, especially cracks and gas porosities were detected in the plates welded on only one face. In this case, only 50% of the cross section is repaired conferring to the alloy low mechanical performances. Based on the results achieved, EN AW 7075 Al-based alloy plates welded on both faces by Tungsten Inert Gas technique reveal good welding appearance and the mechanical properties reached are comparable to those obtained in case of un-welded alloys.

REFERENCES

[1] Ding-Ni Zhang, Qian-Qian Shangguan, Can-Jun Xie, Fu Liu, A modified Johnson–Cook model of dynamic tensile behaviors for 7075-T6 aluminum alloy, Journal of Alloys and Compounds 619 (2015) 186–194.

[2] S. Rajakumar, C. Muralidharan, V. Balasubramanian, Influence of friction stir welding process and tool parameters on strength properties of AA7075-T6 aluminium alloy joints, Materials and Design 32 (2011) 535–549.

[3] Mohan Kumar S, Pramod R , Shashi Kumar M E , Govindaraju H K, Evaluation of Fracture Toughness and Mechanical Properties of Aluminum Alloy 7075, T6 with Nickel Coating, Procedia Engineering 97 (2014) 178 – 185.

[4] Amjad Saleh El-Amoush, Investigation of corrosion behaviour of hydrogenated 7075-T6 aluminum alloy, Journal of Alloys and Compounds 443 (2007) 171–177.

[5] U. Zupanc, J. Grum, Effect of pitting corrosion on fatigue performance of shot-peened aluminium alloy 7075-T651, Journal of Materials Processing Technology 210 (2010) 1197–1202.

[6] LI Jinfeng, PENG Zhuo-wei, LI Chao-xing, JIA Zhi-qiang, CHEN Wen-jing, ZHENG Zi-qiao, Mechanical properties, corrosion behaviors and microstructures of 7075 aluminium alloy with various aging treatments, Trans Nonferrous Met. Soc. China 18 (2008) 755–762.

[7] H. Khalid Rafi, G.D. Janaki Ram, G. Phanikumar, K. Prasad Rao, Microstructure and tensile properties of friction welded aluminum alloy AA7075-T6, Materials and Design 31 (2010) 2375–2380.

[8] M. Temmar, M. Hadji, T. Sahraoui, Effect of post-weld aging treatment on mechanical properties of Tungsten Inert Gas welded low thickness 7075 aluminium alloy joints, Materials and Design 32 (2011) 3532–3536.

[9] S. Kou, Solidification and liquation cracking issues in welding, JOM 55 (2003) 37-42.

[10] Yue Yang, Leilei Zhou, Improving Corrosion Resistance of Friction Stir Welding Joint of 7075 Aluminum Alloy by Micro-arc Oxidation, J. Mater. Sci. Technol., 2014, 30(12), 1251–1254.

[11] E. Cerri, P. Leo, Aging of medium strength aluminum alloy friction stir welds produced by different process parameter after tensile strain hardening, Materials Chemistry and Physics 147 (2014) 1123–1133.

[12] S. Suenger, M. Kreissle, M. Kahnert, M. F. Zaeh, Influence of Process Temperature on Hardness of Friction Stir Welded High Strength Aluminum Alloys for Aerospace Applications, Procedia CIRP 24 (2014) 120–124.

[13] S. Rajakumar, V. Balasubramanian, Establishing relationships between mechanical properties of aluminium alloys and optimised friction stir welding process parameters, Materials and Design 40 (2012) 17–35.

[14] R. K. Shukla1 and P. K. Shah, Comparative study of friction stir welding and tungsten inert gas welding process, Indian Journal of Science and Technology Vol. 3 No. 6 (June 2010) 667–671.

[15] I. Peter, M. Rosso, Effect of the filler metals on aluminium alloy joints, Metalurgia International, 4 (2011) 157–160.

[16] O.T. Ola, F.E. Doern, Fusion weldability studies in aerospace AA7075-T651 using high-power continuous wave laser beam techniques, Materials and Design 77 (2015) 50–58.

[17] T. Ishide, S. Tsubota, M. Watanabe, K. Ueshiro, Latest MIG, TIG Arc-YAG laser hybrid welding system, J. Japan Weld. Soc. 72 (2003) 22–26.

[18] M.M. Shtrikman, A.V. Pinskii, A.A. Filatov, V.V. Koshkin, E.A. Mezentseva, N.V. Guk, Methods for reducing weld porosity in argon-shielded arc welding of aluminium alloys, Weld. Int. 25 (6) (2011) 457–462.

The Scientific Bulletin of VALAHIA University
MATERIALS and MECHANICS –Vol. 15, No. 13

DOI 10.1515/bsmm-2017-0012

STUDY ON INFLUENCE OF MICROSTRUCTURE AND THERMAL TREATMENT ON MAGNETIC LOSSES FROM NON-ORIENTED SILICON ELECTRICAL STEEL

Elena Valentina STOIAN[1], Maria Cristiana ENESCU[1], Vasile BRATU[1], Carmen Otilia RUSANESCU[2], Florina Violeta ANGHELINA[1]

[1]Valahia University of Targoviste, Faculty of Materials Engineering and Mechanics,
Department of Materials Engineering, Mechatronics and Robotics
13 Aleea Sinaia Steet, Targoviste, Romania
[2] Politehnica University of Bucharest, Faculty of Biotechnical Systems Engineering, 313 Splaiul Independentei, 060042, Bucharest, Romania

E-mail: elenastoian22@gmail.com

Abstract. *Non/oriented electrical sheets are sheets tailored to produce specific properties and are produced from Fe-Si or Fe-Si-Al alloys. Non-oriented electrical steel sheets are incorporated into a wide range of equipment, from the simplest domestic appliances to hybrid and pure electric vehicles. In studying about the magnetic, there have a lot of method can be used for the different experiment requirement such as measuring magnetic flux, nominal loss and other objectives.*
During electrical steel processing, there are usually small variations in both chemical composition and thickness in the hot-rolled material that may lead to different magnetic properties for the same steel grade. Therefore, it is of great importance to know the effects of such variations on the final microstructure and magnetic properties of these steels.The purpose of this work was to study microstructural changes of the bands investigated during processing occurring siliceous strips with non-oriented grains.The second aim was to study the influence of grain size on the total magnetic losses at 1.0 T and 1.5 T. Materials 10 rolls intended to be processed into quality electrical steel M400-50A (according to EN 100027-1) were analyzed with metallographic microscope Neophet 32 and the magnetic characteristics was made with Epstein frame according IEC 6040/4-2, with an exiting current frequency of 50Hz at 1.5T and 1.0T induction after aging treatment of 225^{0}C for 24 hours. Sample for light microscopy observation were prepared by polishing and etching in 5% Nital.

Keywords: *magnetic losses, grain size, cold rolled strip.*

1. INTRODUCTION

In cold rolling, the properties of products obtained from hot rolling , eg. mechanical and technical characteristics, are changed by compression between rollers without previous heating of the input.

Cold rolled products are mainly strips and sheets with a high quality surface finish and precise metallurgical properties for use in high specification products.

In 1996 the production of cold rolled strip (sheets and plates) was about 39.6 million tons. [1]. The main producing countries were Germany with about 10.6 million tons, France with 6.3 million tons , Italy with 4.3 , UK with 4.0 million tons and Belgium with 3.8 million tons.

Cold rolled strip industry in the EU is concentrated and fragmented. The largest 10 companies account for 50 % of production while another 140 companies account for the remaining 50 %. Most large companies are located in Germany, which dominates the market with about 57 % of EU production (2.57 million tons in 2012), while the remaining companies are classified as small and medium sized enterprises (see figure 1 and table 1). [2]

In 2012 , Germany produced about 45 % of the total cold rolled strip, with 1.9 million tonnes, followed by Italy and France each with a production of 0.9 million tons.

Total production of cold rolled flat products in 2010 was 39.7 million tonnes , represented by 15 EU member states. Production of stainless and electrical sheet mean 2.3 and respectively 1.13 million tons , representing 6.4 % and 3.2 % of the total [3, 4, 5].

Non-oriented electrical steel cold rolled electrical steel have approximately equal magnetic properties in all directions tape (isotropic materials) and are used for electrical motors and generators , small transformers and other equipment [4, 5 ,6 , 13].

Electrical steel is the most important soft magnetic material currently used. Its use as an alloy to improve magnetic properties was patented by Sir Robert Hadfield at the end of the century XIX [10, 12, 13, 14].

Table 1. Production of cold rolled sheet and strip [1000 t]

Austria	1289
Belgium	3852
Denmark	0
Finland	890
France	6296
Germany	10615
Greece	380
Ireland	0
Italy	4271
Luxembourg	336
Netherlands	2088
Portugal	202
Sweden	1174
Spain	3093
UK	4026

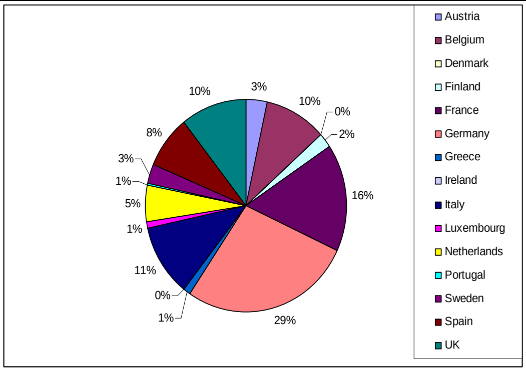

Figure 1. Production of cold rolled sheet and strip [1000t]

The continuous development of the industry producing electricity required for steel manufacture with superior properties in order to decrease power dissipation as heat in electric devices to reduce the physical size of the equipment and also to improve their performance.

Most of the electrical energy produced in the entire world is consumed in electrical motors [10,11,13,16,17,20], which are rotating machines that employ nonoriented electrical steels as soft magnetic materials.

2. MATERIALS AND METHODS

From to brand of steel 5542 are obtained 5 types of electrical steel sheet. They are: M330-35A, M330-50A, M350-50A, M400-50A and M400-65A.

From a sample of 40 rolls we analyzed 10 rolls intended to be processed into quality electrical steel M 400-50A (according to EN 100027-1).

So for mark M 400-50A we have a non-oriented electrical steel magnetic strip with specific losses at 1,5T maximum of 400 [W/kg] at 50 [Hz] , a nominal thickness of 0,50 mm .

The study of metallographic structure is important because it gives us information on how to develop on heat treatments, mechanical and thermo, putting into evidence the defects (microporosity, nonmetallic inclusions).

The resultant magnetic proprietes were measured via Epstein testing according IEC 60404-2, with an exciting current frequency of 50 [Hz] at 1,5 T and 1,0 T induction after aging treatment of 225^{0}C for 24 hours. Samples for light microscopy observation, were prepared by polishing and etching in 5% Nital.

2.1 Determination of remagnetization losses using Epstein frame, wattmeter method

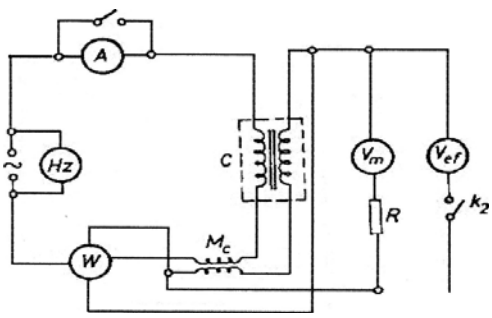

Figure 2. Main scheme of the system for the determination of remagnetization losses

C = Epstein frame of 25 cm, W = Wattmeter, A = effective value ammeter, Vm = average value voltmeter, Vef = effective value voltmeter, MC = mutual inductance for flow compensation in air, Hz = frequency meter, R = resistance additional, k1, k2 = switches

The standard method for characterization of electric steels is the Epstein test. Alternating losses occur predominately along the outer periphery of machine stators and in machine teeth. High frequency losses occur in machine teeth and rotor surfaces. Rotational losses occur at the roots of stator teeth and all along the inner portions of the stator core. At a given induction level, rotational losses may be several times larger than alternating losses. To a lesser extent, rotational losses also occur in the rotors of induction motors due to the difference in rotational velocity between the rotor and the field due to the stator [21].

The Epstein frame consists of four solenoids with the same mechanical and electrical characteristics so as to form the sides of a square. Each solenoid has two windings, made on a non-magnetic insulating casing, a primary (magnetizing) wrapping and a secondary one (measuring). Each coil has two windings, one primary and one secondary. The coils are in the form of a square. Inside the bobbins are placed a number of materials weighing about 2.5 kg each. The sheets are cut into strips, half along the lamination, and the other half perpendicular to the lamination direction to obtain a mean loss.

The average values of the electromagnetic stresses induced in the secondary winding of the Epstein frame at induction values of 1,0 and 1,5 [T], the mean voltage at the secondary winding terminals, the correction of the secondary voltage are determined.

The determined results are considered satisfactory if they meet the condition whic is presented in equation 1:

$$\frac{P_{i\,max} - P_{i\,min}}{2} = P_w \frac{Z}{100} \qquad (1)$$

where: P_{imax} = the maximum value indicated by the wattmeter within the determinations string, [W];

P_{imin} = the minimum value indicated by the wattmeter in the determinations string, [W];

P_w = average value of the wattmeter indication string, [W];

Z = coefficient with values between (1 - 2.5).

It is determined the mean values for P_W at 1.0 and 1.5 T and are calculate the remagnetization losses.

2.2 The microstructure and heat treatment influence over the magnetic loses

Microstructural analysis of electrical cold rolled strip was made for one chemical compositions of electrical steel, namely for example strip A, chemical composition was, according to Table 2:

Table 2. Chemical composition of the strip A

C	Mn	Si	S	P	Al
0.024	0.216	1.224	0.004	0.071	0.23

The cold rolling hot rolled strip suffer 4-5 high passes each pass deformation of 20-25% and a total degree of reduction of 80%. For strip A, rolling finish temperature was 923^{0}C.

The strips were subjected to an annealing treatment duplex. Thus, the strips were subjected to recrystallization heat treatment followed by a decarburization treatment.This treatment helps to increase non-oriented grains.[7, 8] Decarburization treatment was conducted at 830^0 C temperature, and the recrystallization at 940^0 C .

Magnetic loss includes hysteresis losses and eddy current losses. They are determined with Epstein frame, at certain induction and frequency. For lot analised frequency measurements were performed at the induction J = 1500 mT and frequency f = 50 Hz .

In Table 3 are shown the characteristics of the non-oriented electrical steel sheet, which has represented the base of research.[10]

The cold rolling hot rolled strip suffer 4-5 high passes each pass deformation of 20-25% and a total degree of reduction of 80%. For strip A, rolling finish temperature was 923^{0}C.

Table 3. The characteristics of the non-oriented electrical steel sheet analysed

No.of roll	Grain size [μm]	Magnetic loss at 1.0T	Magnetic loss at 1.5T	H_{max} [A/m]	J_{max} [mT]	H_c [A/m]
55447	27	2.11	4.66	1142.8	1500.4	96.669
56161	30	2.1	4.61	1149.6	1500.5	95.668
56162	31	1.91	4.2	1241.8	1500.1	96.653
56160	33	1.92	4.28	1242.2	1500.6	95.539
56147	46.5	1.89	4.24	1312.3	1500.2	95.649
55409	47	1.88	4.24	1344.7	1500.2	75.009
56158	45	1.85	4.20	1221.9	1500.7	76.837
56159	46	1.86	4.13	1408.7	1500.2	76.357
55408	47.5	1.87	4.16	1142.0	1500.6	77.423
56152	48.5	2.01	4.16	1257.1	1500.3	78.337

According to table 3. we find that the magnetic losses specific to 1.0T are located around 2 [W/kg]. with a maximum value of 2.11 [W/kg] and a minimum value of 1.85 [W/kg].

Loss magnetic at 1.5T for non-oriented electrical steel silicon steel are located close range of 4 [W/kg] with a maximum value of 4.66 [W/kg] and a minimum value of 4.13 [W/kg].

In terms of standards. we found that all rolls analyzed have noticeable loss in accordance with EN 10027-1 falling. namely for lot M 400A -50A magnetic Loss of around 4.00 [W/kg].

Following decarburization and annealing heat treatments for band A. a grain size ranges around 50μm .Under the same conditions of heat treatment for decarburization and annealing (the line speed of treatment is 32 m/min and the temperature of decarburization and annealing are 830^{0}C respectively 940°C) for the other bands were obtained grain sizes much finer. by approximately 27 μm.

This difference is reflected later in grain values total magnetic losses. Thus. band A. the total magnetic losses are 4.16 [W/kg] for the tape while the finer particle size of the magnetic losses. are 4.66 [W/ kg] .

It is noted that the carbon content after decarburization and annealing is around 0.003 %.

Subsequently. the microscopic analysis was performed and a band in which the non-oriented grain silicon steel. which was decarburized and annealed conditions. obtaining the following values of microstructures with different grain size. shown in figures 3-7:

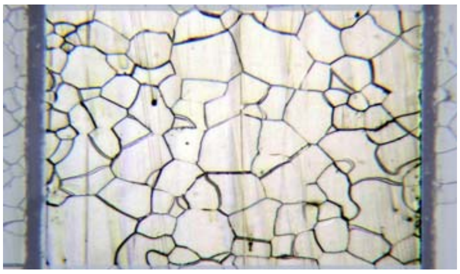

Figure 3. Band thickness 0.5mm;
(Grain size: 48.5µm;Total loss at 1.5T = 4.16 [W/kg];Attack: Nital 5%; Magnification: x 200)

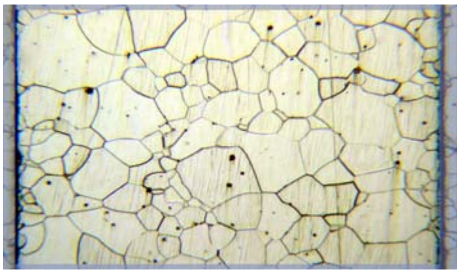

Figure 4. Band thickness 0.5mm;
(Grain size: 45 µm.Total loss at 1.5T = 4.20[W/kg]. Attack: Nital 5%.Magnification: x 200)

The microstructure of Figure 2 was obtained after a holding time of 619 seconds . yielding a grain size of 48.5µm and total loss at 1.5 T of 4.16 [W / kg] .

The microstructure of Figure 3. was obtained after a holding time only 578 seconds . and the particle size was fine . resulting in a size of grain of 45 micrometres and the value of the total loss at 1.5 T being 4.20 [W/kg] .

Treatment line speed was between 28 m/min (for figure2) and 30 m/min (for figure 3).

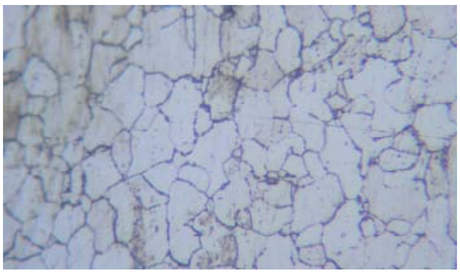

Figure 5. Band thickness : 0.5mm;
(Grain size: 33µm;Total loss at 1.5T=4.28 [W/kg];Attack: Nital 5%;Magnification: x 200)

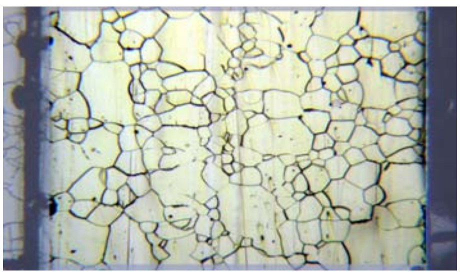

Figure 6. Band thickness: 0.5mm;
(Grain size: 30 µm;Total loss at 1.5T =4.61 [W/kg];Attack: Nital 5%; Magnification: x 200x)

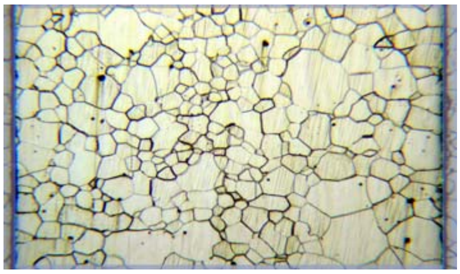

Figure 7. Band thickness : 0.5mm;
(Grain size: 29 µm;Total loss at 1.5T =4.66 [W/kg];Attack: Nital 5%;Magnification: x 200)

3. RESULTS AND DISCUSSION

The microstructure of figure 5 has been obtained after a holding time of 542 seconds . the line speed of treatment is 32 m / min obtaining a size of grain of 33µm . and the total loss at 1.5 T being 4.28 [W/kg] .

For the microstructure of figure 6 are the same as the conditions for maintaining only that. there was obtained a grain size of 30µm and the value of the total loss at 1.5 T being 4.61 [W/kg] .

Microstructure of figure 7 was obtained after a holding time of 510 seconds. of treatment line speed was 34 m/min . Obtained a grain size of 29µm and the total loss at 1.5 T were 4.66 [W/kg].

For all 10 types of strip thickness. was 0.5 mm strips. measurements were made of the grain size and the magnetic losses. specifice at 1.5T and 1.0T respectively . and the results are presented in Table 3.

Based on the results summarized in Table 3 in terms of grain size bands analyzed and Loss magnetic at 1.0T and 1.5T . we could draw graphs on the influence of grain size on the total magnetic losses. the 1.0T (figure 8) and 1.5T (figure 9) .

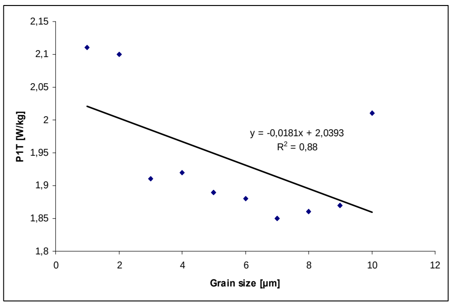

Figure 8. The influence of grain size on the total magnetic losses at 1.0T

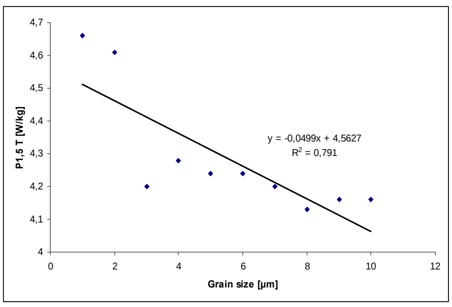

Figure 9. The influence of grain size on the total magnetic losses at 1.5T

Increasing the grain size is desirable for non-oriented electrical steel strips electro. Magnetitc total losses are much lower since the grain size is larger. For lot examined. a size of grain of 27 µm afforded the total magnetic losses at 1.0T and 1.5T. 2.11[W/kg] respectively 4.66 [W/kg] .

Also loss magnetic at 1.0 T and 1.5T increase with increasing concentration of carbon to silicon steel non-oriented electrical steel analyzed. [10]

4. CONCLUSIONS

Therefore. it can be concluded that decarburization and annealing steps leading played an important role in the final grain size strip.

If after hot rolling the main constituent was ferrite. after annealing heat treatments besides the main constituent ferrite in the strips studied appear the tertiary cementite with a score of 3/5.

After analyzing silicon steel non-oriented electrical steel annealed and decarburized treatmnets. hold time treatment varied between 510-619 seconds. and the line speed was between 28-34 [m /minutes].

For group analyzed magnetic losses decreases with increasing grain size. Thus loss magnetic lowest are 2.01 to 1.0 T [W/kg] and 1.5T to 4.16 [W/kg].

Total magnetic losses are even lower since the grain size is larger. For lot examined. a size of grain of 27 µm it led to obtaining the total magnetic losses at 1.0 T is 2.11 [W/kg] and at 1.5 T respectively 4.66 [W/kg].

For a larger grain size of 48.5 µm magnetic losses to 1.5 T and 1.0 T decreased values 2.01 [W/kg] respectively 4.16 [W/kg]. according table 3. For the correlation coefficients were obtained significant values. namely $R_{1T} = 0.88$ and $R_{1.5T} = 0.79$.

Since in both cases were obtained correlation coefficients wich tends to value one . we can say that between the two variables (size of grain and magnetic losses total at 1.0 T and 1.5 T. respectively) there is a linear relationship of positive slope or directly proportional.

The properties required of these steels are a high permeability and induction. low magnetic losses. and low magnetostriction.

Current research aims to increase the performance of the electrotechnical panels used in the range wide frequency. in order to achieve efficient structures of electrical machines. hybrid electric vehicles since being environmentally friendly is one of the essential requirements for the future.

REFERENCES

[1] Rehman S.- Solar radiation over Saudi Arabia and comparisons with empirical models. Energy 1998; 23(12). pp. 1077 – 1082.

[2] I. Petryshynetsa. F. Kovaca . V. Stoykaa and J. Borutab. Influence of Microstructure Evolution on the Coercive Forces in Low Silicon Non-Oriented Steels. 14th Czech and Slovak Conference on Magnetism. Košice. Slovakia. July 6–9. 2010. Vol. 118 (2010) Acta Physica Polonica a No. 5.

[3] Lyudkovsky. G. Effect of Antimony on Recrystalization Behaviour and Magnetic Properties of a Nonoriented Silicon Steel.Metallurgical and Materials Transaction A. Vol. 15. No.2. February 1984.

[4] J. Hunady . M. Cernik . E. J. Hilinski . M. Predmersky . A. Magurova. Influence of Chemistry and Hot Rolling Conditions on High Permeability Non-Grain Oriented Silicon Steel. Journal of Metals. Materials and Minerals. Vol.15 No.2 pp.17-23. 2005.

[5] Darja Steiner Petrovic. Non-oriented electrical steel sheets. ISSN 1580-2949 MTAEC9. 44(6)317(2010).

[6] T. Shimazu. M. Shiozaki. K.J. Kawasaki. J. Magn. Magn. Mater. 133. 147 1994.

[7] R.H. Heyer. D.E. McCabe. J.A. Elias. Flat Rolled Products. Interscience New York 1962. p. 29.

[8] F.E. Werner. R.I. Jaffee. J. Mat. Eng. Perf. 1 (1992) 227.

[9] M.F. de Campos et al. The optimum grain size for minimizing energy losses in iron. Journal of Magnetism and Magnetic Materials 301 (2006) 94–99.

[10] C.O. Rusănescu. M. Rusănescu. F.V.Anghelina – Variation of mechanical properties with temperature for an ecomaterial; Optoelectronics and advanced materials – rapid communications. Vol. 7. No. 11-12. 2013. p. 947-951.

[11] E. Cazimirovici. ş.a.. Machinery and processes in steel. Didactic and Pedagogic Publishing. Bucharest 1974.

[12] A. Nanu. Materials technology. Didactic and Pedagogic Publishing. Bucharest. 1977.

[13] C.O. Rusănescu. C. Jinescu. G. Paraschiv. St. Biris. M. Rusănescu. O. Ghermec -Influence of the Nb. V and Mo Elements on the Ecological Micro-alloyed Steel Properties. Revista de chimie 66. no. 5 (2015): 754-757. ISSN: 0034-7752.

[14] Nicolae Cănănău. Victor Petrescu. Plastic deformation technology. Macarie Publisher. Târgovişte. 2002.

[15] Erdemir România SRL/ Working procedure for cold rolling .

[16] C.O. Rusănescu. M. Rusănescu. T. Iordănescu. F. V. Anghelina – Mathematical relation ships between alloying elements and technological deformability indexes. Journal of optoelectronics and advanced materials. Vol. 15. No. 7-8. 2013. p. 718-723.

[17] F.V.Anghelina. V. Bratu. I. N. Popescu. Estimating the stacking faults of high alloyed steels. pp. 7 - 11. The Scientific Bulletin of Valahia University. Materials Science and Mechanics. Nr. 8 (year 11). ISSN 1844-1076. 2013.

[18] C. O. Rusănescu. M. Rusănescu. F. V. Anghelina. V. Bratu - The influence of the micro-alloying elements on physical and structural characteristics of the some steel destined for manufacturing the oil pipes. Romanian Reports in Physics. Vol. 68. No. 1. P. 278–293. 2016. ISSN: 1221-1451 ; eISSN: 1841-8759.

[19] F.V.Anghelina. Correlation Between Primary Recrystallization Texture And Goss Texture For The Electrotechnical Steel. Magazine JOSA-Journal of Science and Arts. Nr. 1 /2014. ISSN 1844-9581. Ed. Bibliotheca.Targoviste.

[20] C. O. Rusănescu. M. Rusănescu - The influence of the residual copper on the pipes steel hot plasticity according to environmental requirements. Journal of Mining and Metallurgy. Section B: Metallurgy; J. Min. Metall. Sect. B-Metall. 49 (3) B (2013) 353 – 356; ISSN: 1450-5339.

[21] R.D. Findlay. et.al. "Losses Due to Rotational Flux in Three Phase Induction Motors." IEEE Transactions on Energy Conversion. Vol. 9. No. 3. September 1994.

DE GRUYTER OPEN

The Scientific Bulletin of VALAHIA University
MATERIALS and MECHANICS –Vol. 15, No. 13

DOI 10.1515/bsmm-2017-0013

A COMPARATIVE STUDY ON THE PROPERTIES OF POTENTIALLY BIOACTIVE GLASSES OBTAINED BY SOL-GEL TECHNIQUE AND BY MELTING MIXTURES OF OXIDES

Daniela AVRAM[1], Dan UNGUREANU[2*], Nicolae ANGELESCU[2], José BARROSO DE AGUIAR[3]

[1] Faculty of Environmental Engineering and Food Science, Valahia University, Targoviste, [2] Faculty of Materials and Mechanical Engineering, Valahia University, Targoviste, [3] Minho University, Portugal

E-mail: danungureanu2002@yahoo.com

Abstract. *Phosphocalcic glasses, based on ternary system SiO_2 - CaO- P_2O_5 and those doped with copper (SiO_2 – CaO - P_2O_5 - Cu_2O) can be obtained by the traditional method of sub-cooling melts or modern methods such as process that uses mechanical energy, neutrons action, deposition in thin layers or by sol-gel technique. This paper shows the experimental results of three compositional phosphocalcic glasses: 50% SiO_2 - 43% CaO - 7% P_2O_5 , 50% SiO_2 - 38% CaO - 7% P_2O_5 - 5% Cu_2O obtained through sol-gel method and 45% SiO_2 - 22.5% CaO - 22.5 Na_2O - 5% P_2O_5 - 5% Cu_2O obtained by melting. In order to study their bioactivity, the three compositions were structural analyzed by X-ray diffraction method. In this case the apatite formation was highlighted after soaked in simulated body fluid, but also other compounds ($CaCO_3$ and CuO) resulting from the same process were observed. In case of the melting glass apatite formation has not been highlighted. The functional groups present in the structure of glasses before and after soaking (PO_4^{3-}, CO_3^{2-} and HO^-) were highlighted by the Fourier Transform Infrared Spectroscopy (FTIR). The elemental chemical composition was confirmed by elemental analysis WD-XRF. The morphology of sol-gel glass powders was revealed by SEM analysis. All glass compositions were tested in terms of antibacterial activity in vitro.*

Keywords: *phosphocalcic glasses, WD-XRF, XRD, FTIR, SEM, antibacterial activity, copper*

1. INTRODUCTION

Research on bioactive glasses continues today, nearly 50 years after patenting of the first composition, 45S5, by Hench and Clark in 1968. After they showed the osteointegration potential of phosphocalcic glass composition, the next step was to study the possible antimicrobial, anti inflammatory and healing properties. That can be conferred by modification of chemical composition, thermal treatments, but especially by doping with different metals with such already known properties [1, 2, 3, 4].

The reparative and reconstructive medicine has as main objective the use of biofunctionally, biomechanically and, last but not least, bioprofilactic materials for the hard tissues, but also for the soft tissues adjacent to the implant [5].

Bioactive and prophylactic glasses represent a relatively new class of inorganic biocompatible materials that are far from demonstrating their full applicative potential in implantology. They induce the postimplantation formation of a carbonated hydroxyapatite layer at their surface, easy to colonize by skeletal cells (osteoblasts, tenocytes, chondrocytes), which leads to a strong bond with bone tissue [6,7].

Hydroxyapatite (HAp) is the mineral component of bones and teeth with applications for conservation and restoration of these tissues [8]. Due to the poor mechanical characteristics, this biomaterial along with the bioactive glasses is used for coating applications, especially on metallic biomaterials [9].

The introduction of silver, copper and other bactericidal metals into the biomaterial composition was preferred to the introduction of antibiotics (gentamicin, vancomycin, cefalexin etc.) [10-14] because most strains of microorganisms became resistant to drugs and their effectiveness in preventing and the fight against infections has become limited, not to mention the extremely high costs of using them [15].

The doping of biomaterials with copper began to be practiced only after 2005 [16], although its antimicrobial capacity has been known since the Hippocratic time (400 BC) which prescribes it in the treatment of pulmonary, psychic and water problems.

2. EXPERIMENTAL PROCEDURE

Three glass compositions from SiO_2-CaO-P_2O_5 system were synthesized. The composition of bioactive glasses obtained and analyzed in this paper is shown in Table 1.

The two glasses denoted S1 and S2 were synthesized by the sol-gel method using the following precursors:

- tetraethylortosilicate ($Si(OC_2H_5)_4$ - TEOS)
- triethylphosphate ($(C_2H_5)_3PO_4$ - TEP)

- calcium nitrate tetrahydrate ($Ca(NO_3)_2 \cdot 4H_2O$)
- copper chloride (CuCl)

Table 1. Composition of sol-gel glasses

Oxidic composition [% wt.]	SiO_2	CaO	P_2O_5	Cu_2O	Na_2O
S1	50	43	7	-	
S2	50	38	7	5	
S3	45	22.5	5	5	22.5

A third phosphocalcic glass composition, S3, was synthesized by the melting of oxide mixtures by using the following precursors:

- sand (quartz): 95% SiO2
- calcium carbonate: 98.5% $CaCO_3$
- diammonium hydrogen phosphate: 98% $(NH_4)_2HPO_4$
- sodium carbonate: 99.8% Na_2CO_3
- cuprous chloride (CuCl)

The raw materials were mixed, milled and melted in alumina crucibles at 1415 °C. The molten glass obtained was partially cast on a metal plate, and the remainder in a crucible with water. In the next step both glasses obtained by melting method were annealed in order to relieve residual internal stresses. Finally, the two samples were milled in order to achieve the bioactivity test by soaked in simulated body fluid.

The synthesis of sol-gel glasses is carried out in four steps [17]:

- hydrolysis and condensation of precursors in order to obtain sol
- gelling and aging of the gel (Figure 1a);
- drying of the gel with formation of xerogel at temperatures below 180 ° C for 48-72 hours (Figure 1b);
- stabilization of xerogels by calcination at 600 ° C for 8 hours. (Figure 1c).

a b c

Figure 1. Sinthesis of S2 doped glass by using the sol-gel method: a - gels, b - xerogels, c – bioglass powders

3. METHODS OF ANALYSIS

The evaluation of the three samples was carried out by: X-ray diffraction, X-ray fluorescence spectroscopy (WD-XRF), infrared spectroscopy (FTIR), SEM (electronic scanning microscopy); microbiological assessment required the testing of the antibacterial properties of copper-doped bottles (S2 and S3) on two reference bacteria cultures most commonly found in nosocomial infections: Staphylococcus aureus (pathogen bacteria) and Escherichia coli (conditionally pathogenic bacteria).

The chemical composition was determined by X-ray fluorescence spectroscopy by using Advant'X ARL-Thermo Scientific spectrometer with the X-ray tube (2400 W, 60 kV and 80 mA).

The structural characterization of bioactive glass powders was performed by X-ray diffraction with Rigaku Ultima IV diffractometer, having the following characteristics: scanning range: $20\text{-}60^0$ (2θ), scanning speed: 0.04 degree / sec, X-ray tube: power 3KW, U = 40KV, I = 40mA.

The chemical groups specific to bioactive bottles were highlighted by infrared spectroscopy (FTIR) with the Bruker Vertex 80 spectrometer having the following characteristics: scanning interval: 4000-400 cm^{-1}, spectral resolution: 2 cm^{-1}.

The morphological study of the glasses before and after immersion was performed by using the Hitachi SU-70 scanning electron microscope with a minimum resolution of 1.0 nm and acceleration voltage of 15 kV.

In order to achieve the antimicrobial properties of copper-doped glass Koch culture method to incorporate the germs into nutrient environments and incubate them in a Nitech (+/- 0.1 °C) adjustable electric thermostat at the temperatures and durations specific to each type of culture.has been used.

The manipulation of bacterial cultures was performed in a microbiological niche by using sterile Pasteur pipettes, Petri dishes and sterile glassware.

4. RESULTS AND DISCUTION

4.1 XRD analysis

At the initial moment it can observe the predominantly amorphous structure, characteristic of the vitreous materials. For glass composition S1 were found three peaks specific to hydroxyapatite (HAp) at 25.74 2θ, 46.7 2θ and 53.12 2θ (Fig. 2).

In case of copper doped (S2) sample, a single specific hydroxyapatite peak was identified at 31.8 2θ. The peaks at 35.6 2θ, 38.8 2θ and 48.8 2θ are specific to copper oxide (ICDD-PDF 2: 00-041-0254).

After 14 days of immersion in SBF solution (Figure 3) there was an increase of HAp peaks (25.88 2θ; 31.79 2θ; 31.1 2θ; 39.57 2θ; 43.8 2θ; 46,66 2θ; 49,44 2θ and 53,33 2θ and the occurrence of calcite at 29.28 2θ.

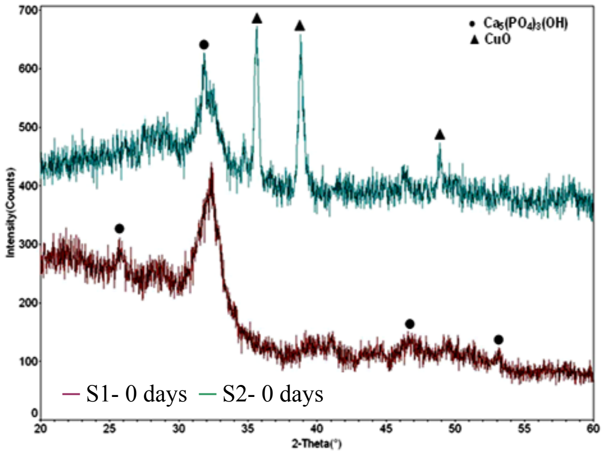

Figure 2. X-ray diffraction spectra for unsoaked S1 and S2 glasses

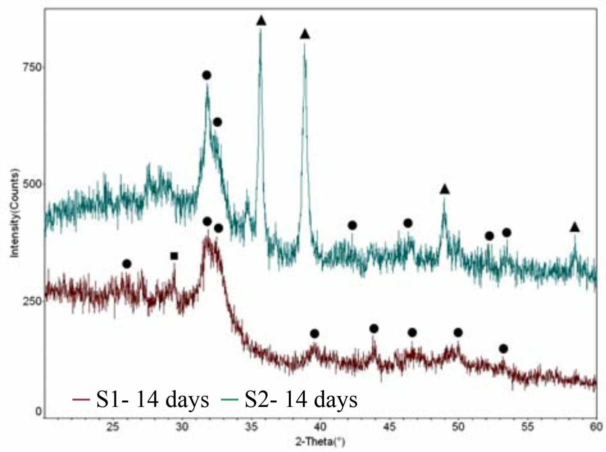

Figure 3. X-ray diffraction spectra for S1 and S2 glasses soaked for 14 days in SBF

For the copper doped sample (S2) specific hydroxyapatite peaks were found at 31.78; 32.2; 41.97; 46.6; .53,11 and 53,3 2θ. The peaks located at 35,6 2θ, 38,8 2θ, 46,5 2θ and 58,3 2θ are specific to copper oxide.
In the case of melt derived phosphocalcic glass doped copper (S3) no specific hydroxyapatite peaks were identified (Figure 4).

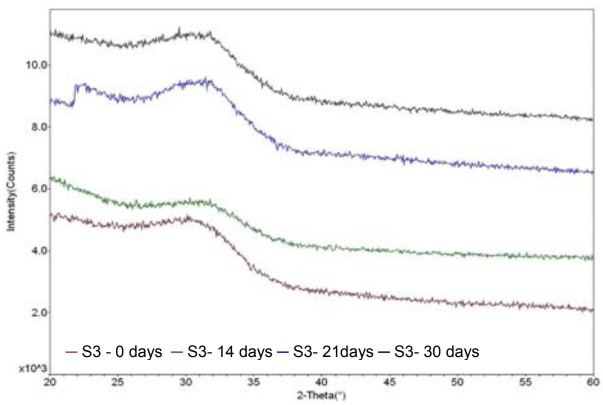

Figure 4. X-ray diffraction spectra for S3 glass before and after soaked in SBF for different time periods

4.2 Determination of elemental composition by WD-XRF analysis

The result of the WD-XRF analysis for the three synthesized glass samples is shown in Table 2.

Table 2. Chemical composition of glasses

Sample	Oxides [% wt.]				
	SiO_2	CaO	P_2O_5	Cu_2O	Na_2O
S1	49,95	41,02	8.06		
S2	51	36	7.01	6.1	
S3	44,8	26,7	3,1	2,6	15,9

In the case of the samples obtained by the sol-gel method (S1 and S2), the results are very close to the theoretical ones, which confirms the correctness of the adopted synthesis method [17, 18].

For WD-XRF analysis, the results of the WD-XRF analysis revealed the presence of alumina (Al_2O_3) - 3.7% and magnesium oxide (MgO) - 1.7% as impurities from alumina crucibles or other materials used to further processing.

4.3 Infrared spectroscopy analysis – FTIR

Molecular groups found in case of unsoaked S1 glass structure (Figure 5) has been identified by the following wave numbers: 448 cm^{-1} and 1012 cm^{-1} for Si-O and Si-O-Si bridges; 559 cm^{-1}, 595 cm^{-1} and 872 cm^{-1} for PO_4^{3-} groups; 1444 cm^{-1} in case of CO_3^{2-} groups; 1627 cm^{-1} for crystallisation water; 2846 cm^{-1}, 2920 cm^{-1} and 3579 cm^{-1} were associated with HO^- groups and water of crystallization present in HAp structure.

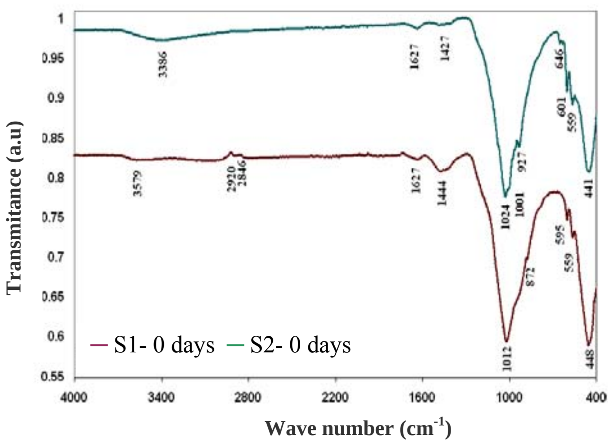

Figure 5. FTIR spectra for unsoaked S1 and S2 glasses

In case of glass S2 analyzed before soaked in SBF solution, the specific molecular groups has been identified at: 441 cm^{-1}, 1001 cm^{-1} and 1024 cm^{-1} for Si-O and Si-O-Si bridges; 559 cm^{-1}, 601 cm^{-1}, 927 cm^{-1} for phosphate groups PO_4^{3-}; peak located at 1427 cm^{-1}

confirm presence of CO_3^{2-}; peak at 1627 cm^{-1} is associated with presence of water in glass structure; 646 cm^{-1} and 3386 cm^{-1}: confirm the presence of HO^- groups and associated water in the same structure.

After soaked in SBF solution for 14 days (figure 6) at the surface of SiO_2-CaO-P_2O_5 glass structure newly formed hydroxyapatite were identified by the following molecular groups: PO_4^{3-} at 561 cm^{-1}, 599 cm^{-1}, 783 cm^{-1} and 873 cm^{-1}; CO_2^{3-} at 1460 cm^{-1}; 1630 cm^{-1}, broaded band from 2356 to 3579 cm^{-1} confirm the presence of hydroxyl groups (OH^-) and water of crystallization in glass and HAp powder structure. Also, the presence of silica has been identified by the peaks at at 443 cm^{-1} and 1020 cm^{-1} associated with Si-O and Si-O-Si bridges.

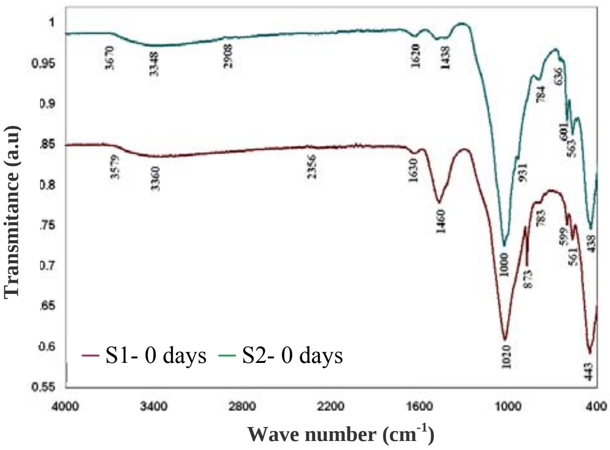

Figure 6. FTIR spectra for S1 and S2 glasses soaked for 14 days in SBF

For S2 glass specific molecular groups were identified at the following wave numbers: 438 cm^{-1} and 1000 cm^{-1} for Si-O and Si-O-Si bridges; 563 cm^{-1}, 601 cm^{-1}, 592 cm^{-1}, 784 cm^{-1}, 931 cm^{-1} for PO_4^{3-} groups; 1438 cm^{-1} for carbonate groups CO_3^{2-}; peak located at 1620 cm^{-1} has been associated with presence of crystallization water and broad band from at 2908 - 3670 cm^{-1} with presence of OH^- from Si-OH associated water of crystallization present in HAp structure.

Hydroxyapatite formation on the surface of S1 and S2 glasses synthesized by the sol-gel technique after in vitro soaking test in SBF highlighted by XRD and FTIR analysis confirms the bioactivity of the two compositions [19, 20, 21].

4.4 Morphological analysis of glass samples

In the case of the first glass composition, S1, unsoaked in SBF solution (Figure 7a), SEM analysis shows particles of different sizes and shapes (10 and 100 µm). The SEM micrograph of Figure 7.b highlights the formation of apatite on the surface of the glass powder, their size are between 0.5 µm and 2 µm. Also, it can be observed a increase in the coverage of the glass surface with apatite particles, which confirms the bioactivity of the glass after SBF immersion, also evidenced by the X-ray diffraction analysis (Figure 3).

The SEM analysis, for unsoaked S2 glass sample 2 (Figure 8a), reveals the irregular appearance of the particle surface. This suggests obtaining a material with a large specific surface area, ideal for nucleation and growth of apatite new formation at glass surface. The SEM micrograph of Figure 8a shows the formation of agglomerations with size between 1µm and 3µm at surface of the glass powder.

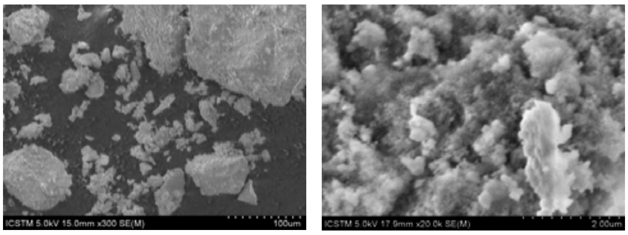

(a) unsoaked sample (b) soaked sample for 14 days

Figure 7. SEM analysis in case of S1 sol-gel glass powders

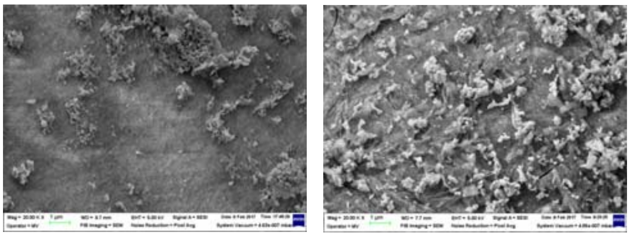

(a) unsoaked sample (b) soaked sample for 14 days

Figure 8. SEM analysis in case of S2 sol-gel glass powders

After immersion for 14 days in SBF solution (Fig.8b), form SEM analysis can be observed that a large number of apatite particles appear on the surface of the glass surface, their tendency is to form agglomerations in areas with rough surface.

4.5 Study of antimicrobial activity for copper-doped glasses

Two strains of bacteria were selected for this study: Escherichia coli MG1655 – Gram-negative conditionally pathogenic bacteria, extremely resistant to antibiotic treatment and Staphylococcus aureus ATCC reg. 25923 - Gram-positive conditionally pathogenic bacteria with the highest risk of post-operative infection, especially in prosthetic and bone reconstruction surgery [22 - 24].

Antimicrobial activity was determined at various concentrations of bioactive glass, maintaining a constant inoculation of microorganisms ($3x10^8$ UFC / ml).

Petri dishes with nutritive media, bioactive glass and inoculum bacteria were aerobically incubated, for different periods of time and temperatures, depending of the type of bacteria used: for Staphylococcus aureus: 48 hours at 37 °C and for Escherichia coli: 24 hours at 44 °C. The volume of culture medium used was constant

(15 ml), and the glass powder concentrations varied from 0.1 g glass / 10 ml physiological saline solution.

The first test has been performed with 0.1 ml of each pure culture of inoculums and 0.1 g of copper doped glass S2. After maintaining at constant temperature, no colonies of bacteria for any strain were found in the Petri dishes (Figure 9a).

In the plates presented in fig. 9b and 9c doped glass has not been added but only pure cultures of each bacterium - they have a control role, to check the purity of culture media and strains of microorganisms. It can be seen that the bacteria has been developed optimally. Also the infection of plaques has been achieved (colonies could not be counted).

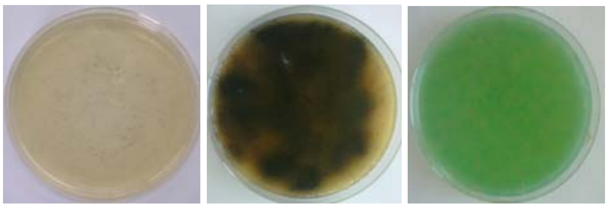

a b c

Figure 9. Plate with 0.1g copper doped glass (S2) (a) control plates without S2 glass for Staphylococcus aureus (b) and Escherichia coli (c)

The test has been repeated for lower concentrations of bioactive glass, after elution of S2 glass for 6 hours in sterile physiological saline solution and subsequent to decimal dilutions. All this results are presented in Table 3.

Table 3. Results of microbiological study for copper doped glass

Dilution of glass sample	Staphylococcus aureus	Escherichia coli
	Number of colonies	
S2(10-1)	13-19	35-39
S2(10-2)	93-162	> 300
S2(10-3)	> 300	> 300
S3(10-1)	19	88-106
S3(10-2)	179-215	> 300
S3(10-3)	> 300	> 300

For both bacterial cultures it is noted that the bioactive glass antimicrobial activity changes according to the concentration (dilution) of copper ions (Figure 10 and Figure 11).

From Table 3, it can be seen that Escherichia coli is more resistant than Staphylococcus aureus at the action of copper ions, because from the dilution of 10-2 g / ml the number of colonies approaches to 300, this phenomenon reveals a massive infection of the plaque.

In the case of the glass obtained by melting metod, the first test, the control test, has been achieved with 0.1 g of S3 glass in the culture medium, led to super infection of plates for both bacterial strains. This indicates that copper ions do not diffuse from the structure of the molten glass, although it has been milled and brought to the same granulation as the S2 glass synthesized by the sol-gel technique.

In order to test the bacteriostatic activity of S3 melted glass, elutions in physiological saline solution for 6 and 24 hours has been performed. For the 6 hours eluted samples, the results were the same as for the non-eluted sample - the glass had no bacteriostatic activity, indicating that the copper ions which migrated from the glass did not have a sufficient concentration for a minimal bactericidal dose. After 24 hours of elution in sterile physiological saline solution and repeating the assay set, it was found that S3 glass samples began to have antimicrobial activity. As can be seen from Table 3, it is noted that they have minimal bactericidal doses of 10^{-2} g / ml Staphylococcus aureus and 10^{-1} g / ml for Escherichia coli, with an order of magnitude smaller (ten times) than the S2 sol-gel glass.

a - d1 (10^{-1}) *b – d3 (10^{-3})* *c – d4 (10^{-4})*

Figure 10. Plates with Staphylococcus aureus at different dilutions of S2 glass

a – d1 (10^{-1}) *b – d2 (10^{-2})* *c – d3 (10^{-3})*

Figure 11. Plates with Escherichia coli at different dilutions of S2 glass

Microbiological tests were also performed for the S1 sol-gel glass composition, without copper ions. The obtained results did not show any antimicrobial activity for any strain of bacteria tested.

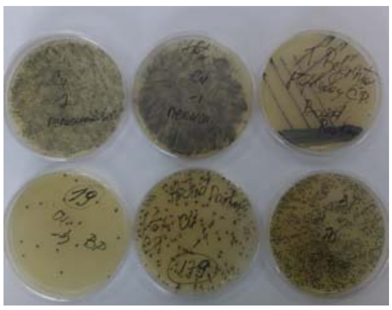

Figure 12. The bacteriostatic effect on Staphylococcus aureus of S3 glass powder

5. CONCLUSIONS

Three glass compositions from SiO_2-CaO-P_2O_5 system has been obtained by the sol-gel and melting of the oxide mixtures methods with rather low production costs.

One of the few advantages of the melting method is the much shorter synthesis time, about 4 hours. By comparison the sol-gel technique required about 136 hours.

The advantages of sol-gel synthesis consist in the ease of controlling glasses compositions, by adding doping materials, the possibility of obtaining powdered materials with a high specific surface and appropriate bioactivity for a wide range of compositions by comparison with melting method.

X-ray fluorescence spectroscopy confirmed a chemical composition very close to that calculated theoretically for both samples synthesized by the sol-gel technique.

In the case of melt glass the chemical composition determined by WD-XRF reveals differences from the theoretical and a relatively high degree of impurification (low conversion of precursors and the presence of undesired oxides - Al_2O_3 and MgO).

The bioactivity of the glasses was revealed by XRD analysis. This method showed a different degree of reactivity in case of the two sol-gel compositions. Hydroxyapatite formation was highlighted in both compositions after immersion in the SBF solution. Copper ion doping does not cancel bioactivity of glass S2, but the number of HAp peaks shown is considerably lower by comparison with composition S1.

In the case of glass obtained by melting method, the XRD analysis did not show the formation of hydroxyapatite, therefore the composition is not bioactive.

Formation of $CaCO_3$ after immersion of sample S1 can be attributed to the degree of saturation of SBF solution in Ca^{2+} and HCO_3 ions and on the decrease of the pH of the medium, which favors the precipitation of basic pH compounds.

In the case of S2 glass composition has been identified the formation of CuO in considerable quantities, which is due to the oxidation of cuprous ions and the change of the balance $Cu^+ \rightarrow Cu^{2+}$ which does not influence the antimicrobial activity of the glass.

CuO format partially collapses the pores of the hydrated silica network, which can reduce the rate of hydroxyapatite formation, but this process does not cancel out the bioactivity of doped glass S2.

The FTIR analysis of the two glasses confirms the presence of PO_4^{3-}, CO_3^{2-} and HO^- specific HAp and HApC groups in SBF-immersed samples but also the presence of Si-O and Si-O-Si groups characteristic of phosphocalcic glasses.

XRD and FTIR analyze show that the formation of the implant-tissue interface is initiated in vitro at 14 days after surgery.

Scanning electron microscopy (SEM) analysis revealed the formation of hydroxyapatite at the surface of the two sol-gel glasses after immersion in the SBF solution.

Glass S1 does not influence the viability of the bacterial strains investigated, and it does not exhibit either bactericidal or bacteriostatic activity. Developed colonies has been infected the plaque and could not be counted.

Copper doped glass by the sol-gel technique (S2) has a bactericidal effect for both strains, up to a minimum bactericidal dose of 10^{-2} g / ml.

Considering the elution time, 4 time higher, for the S3 composition, it can be stated that the melt glass has a much lower bacteriostatic activity than the S2-sol-gel composition.

The antimicrobial activity of Cu is not diminished by the presence of other ionic species (Ca^{2+}, phosphates, silicates) that diffuse with it in the physiological saline solution.

Bacteriostatic activity of the glass has been found to increase directly proportional with the copper concentration diffused in the copper doped glasses structure.

In the case of real graft conditions, in vivo, in order to benefit from the synergistic action of the two compositions synthesized by the sol-gel technique (bioactive and antimicrobial activity), both compositions can be used in the mixture.

The copper content of the S2 composition can not be greatly reduced without affecting the bactericidal capacity of the glass since the copper diffusion rate is slow enough and the bactericidal concentrations may be much lower under real implantation conditions. However, at ion concentrations released in the area of the implant, the critical post-surgical period can be exceeded without significantly reducing the bioactivity of the glass.

REFERENCES

[1] L. L. Hench – *„Bioactive Ceramics”* , in Bioceramics: Material Characteristics vs In Vivo Behaviour, 523, p. 54, Ed. P. Ducheyne and J. Lemons, Annals of N.Y. Academy of Science, New York, 1998.

[2] A. L. Andrade, P. Valerio, A. M. Goes, M. de Fatima Leite, R. Z. Domingues, J. Of Non-Crystalline Solids, 352:3508 -11, 2006.

[3] M. G. Cerruti, D. Greenspan, K. Powers, Biomaterials, 26:4903-11, 2005.

[4] E. Saiz, M. Goldman, J. M. Gomez-Vega, A. P. Tomsia, G. W. Marshall, S. J. Marshall, Biomaterials, 23:3749-56, 2002.

[4] P. N. De Aza, A. H. De Aza, P. Pena, S. De Aza - Bioactive glasses and glass-ceramics, Bol. Soc. Esp. Ceram. 46, p. 45–55, 2007

[6] C. Ohtsuki, T. Kokubo, K. Takatsuka, T.Yamamuro - Compositional dependence of bioactivity of glass in the system $CaO-SiO_2-P_2O_5$: its in vitro evaluation , J. Ceram. Soc. Japan, 99, p.1-6, 1991.

[7] L. L. Hench – Ceramics, Glasses, and Glass–Ceramics in Biomaterials Science, An Introduction to Materials in Medicine; B. D. Ratner, A. S. Hoffman, F.J . Schoen, J. E. Lemons, Ed. Academic Press: San Diego, p. 73–84, 2004.

[8] V. Despa, A. Catangiu, D.N. Ungureanu, I.A. Ivan- Surface structure of CoCrMo and Ti6Al4V parts obtained by selective laser sintering, Journal of Optoelectronics and Advanced Materials, Vol. 15, No. 7- 8: 858 – 862, 2013.

[9] F.V.Anghelina, D.Ungureanu, V.Bratu, I.N. Popescu, C.O.Rusanescu, Fine Structure Analysis of Biocompatible Ceramic Materials Based Hydroxyapatite and Metallic Biomaterials 316L, APPL SURF SCI, 285 A: 65-71, 2013.

[10] U. Joosten, A. Joist, T. Frebel, B. Brandt, S. Diederichs, C. Von Eiff - Evaluation of an in situ setting injectable calcium phosphate as a new carrier material for gentamicin in the treatment of chronic osteomyelitis: studies in vitro and in vivo. Biomaterials,. 25:4287–95, 2004.

[11] W. C. Liu, C. T. Wong, M. K. Fong, W. S. Cheung, R. Y. T. Kao, K. D. K. Luk, ş. a. - Gentamicin-loaded strontium-containing hydroxyapatite bioactive bone cement—an efficient bioactive antibiotic drug delivery system. J Biomed Mater Res B Appl Biomater., 95:397–406, 2010.

[12] S. Hesaraki, R. Nemati - Cephalexin-loaded injectable macroporous calcium phosphate bone cement, J Biomed Mater Res B Appl Biomater., 89:342–52, 2009.

[13] T. Sasaki, Y. Ishibashi, H. Katano, A. Nagumo, S. Toh - In vitro elution of vancomycin from calcium phosphate cement, J Arthroplasty, 20:1055–9, 2005.

[14] P. J. Jiang, S. Patel, U. Gbureck, R. Caley, L. M. Grover - Comparing the efficacy of three bioceramic matrices for the release of vancomycin hydrochloride. J Biomed Mater Res B Appl Biomater., 93:51–8, 2010.

[15] A. Sugawara, K. Asaoka, S. J. Ding - Calcium phosphate-based cements: clinical needs and recent progress, J Mater Chem B., 1:1081–9, 2013.

[16] N. Cioffi et al. - Copper nanoparticle/polymer composites with antifungal and bacteriostatic properties. Chem. Mater. 17:5255–62, 2005.

[17] D. Avram, N. Angelescu, D. N. Ungureanu, V. Bratu - Obtaining simple and doped phosphocalcic glasses by using sol-gel technique, JOAM, Vol. 17, No. 7-8, p. 1038 – 1043, July – August 2015.

[18] D. Avram , D. N. Ungureanu, N. Angelescu, A. Gheboianu, I. Bancuţă, M. G. Bratu - Study of bioactivity and antimicrobial activity in case of glasses from SiO_2 -CaO - P_2O_5 ternary system, The Scientific Bulletin of Valahia University – Materials and Mechanics – No. 10 (year 13), 2015.

[19] D. Avram , N. Angelescu, D. N. Ungureanu, I. Ioniţă, A. Gheboianu, I. Bancuţă - Study of phosphocalcic glasses SiO_2 - CaO - P_2O_5 system with and without silver, part I. Synthesis of glasses and characterization by WD- XRF and XRD, Rev. Ch. Română, vol.68, nr. 5, mai 2017.

[20] D. Avram , N. Angelescu, D. N. Ungureanu, I. Ioniţă, A. Gheboianu, I. Bancuţă, E. M. Lungulescu - Study of phosphocalcic glasses SiO_2 - CaO - P_2O_5 system with and without silver, part II. The bioactivity analysis by FTIR, SEM methods and microbiological study of silver-doped glasses, Rev. Ch. Română, vol.68, nr. 6, iunie 2017.

[21] T. Kokubo, H. Kushitani, S. Sakka, T. Kitsugi, T. Yamamuro - Solutions able to reproduce in vivo surface-structure changes in bioactive glass-ceramic A-W, J. Biomed. Mater. Res., 24, p. 721-734, 1990.

[22] V. Prisacari, A. Paraschiv, C. Jucovschi - Evaluarea epidemiologică a factorilor de risc în infecţiile septico-purulente nosocomiale, Buletinul AŞM, Ştiinţe medicale, Nr 2, pag. 73-86, 2005.

[23] V. Prisacari, S. Stoleicov - Particularităţi epidemiologice şi etiologice în osteita posttraumatică,. Buletinul AŞM, Ştiinţe medicale, Nr 3(7), p. 261-270, 2006.

[24] A. Paraschiv - Pronosticarea apariţiei complicaţiilor septico-purulente. Sănătate publică, economie şi management în medicină, Nr 4, p. 45-48, 2005.

DE GRUYTER OPEN

The Scientific Bulletin of VALAHIA University
MATERIALS and MECHANICS –Vol. 15, No. 13

DOI 10.1515/bsmm-2017-0014

DENTAL CEMENTS

Nicolae ANGELESCU[1], Vasile BRATU[1], Elena Valentina STOIAN[1], Dan Nicolae UNGUREANU[1], Ana-Maria GURBAN[2]

[1] Valahia University of Targoviste, Faculty of Materials Engineering and Mechanics, Department of Materials Engineering, Mechatronics and Robotics
13 Aleea Sinaia Steet, Targoviste, Romania
[2] Metallurgical Research Institute - ICEM Bucharest

E-mail: elenastoian22@gmail.com

Abstract. *Calcium-phosphate cements is one of the most popular types of biomaterials, both due to their specific properties of self - setting and of their superior biocompatibility.*
Although in general the phosphocalcic cements, which are the subject of the present paper, have somewhat lower mechanical properties than other biomaterials based on calcium and phosphorus, or even other dental cements of the same nature. The ceramic compositions presented in the present paper constitute a special category of biomaterials due to other notable advantages that characterize them. Thus, this category of materials is defined by a near-perfect adaptation to the surface of the biological tissue, as well as by a convenient resorption rate, processes followed by the generation of optimal bone formation. In this paper are presented principles of realization of the calcium-phosphate cements (raw materials and conditions of production), as well as the properties of these biomaterials, insisting, in particular, on the chemistry of the setting reactions. At the same time, informations regarding the possibilities of clinical use, such as implants are presented.

Keywords: *calcium-phosphate cements, biomaterials, implants, dental cements*

1. INTRODUCTION

The cements presented in this article consist mainly of calcium phosphate constituents. Reactions that occur at normal temperature involve phase transformations of the constituents, transformations underlying the strengthening process of these biomaterials.

It is a process of self-setting of calcium - phosphate cements. This process takes place by the formation of hydroxyapatite following the hydrolysis reactions of some reagents of phosphocalcic nature.

Data on the use of hardening agents such calcium and phosphorus materials it isn`t subject of this paper. Due to the low solubility of hydroxyapatite in an acid medium, this substance is not used directly for calcium - phosphate cements.

For this reason, in this paper, one may use other phosphocalcic substances by hydrolysis in which causes the hardening of the calcium - phosphate cement by precipitation of hydroxyapatite.

2. RAW MATERIALS

In order to obtain the calcium - phosphate cements, they start from orthophosphate salts, which have PO_4^{3-} groups in their composition. Table 1 shows a series of phosphatic salts of interest in starting materials for the cements discussed in this paper, in order of basicity. Fluorapatite presents of interest in this paper only because biological tissues much of solid solution of bone containing hydroxyapatite and fluoroapatite. [1]

Table 1. Series of phosphatic salts

Salt	Formula	Ca/P molar ratio
Mono-calcium phosphate hydrate	$Ca(H_2PO_4)_2 \cdot H_2O$	0.5
Calcium hydrogen phosphate dihydrate	$CaHPO_4 \cdot 2H_2O$	1.0
Anhydrous calcium hydrogen phosphate	$CaHPO_4$	1.0
Phosphate octocalcic	$Ca_8H_2(PO_4)_6 \cdot 5H_2O$	1.33
α – tricalcium phosphate	$\alpha - Ca_3(PO_4)_2$	1.5

β – tricalcium phosphate	β – $Ca_3(PO_4)_2$	1.5
Hydroxyapatite	$Ca_5(PO_4)_3OH$	1.67
Fluorapatite	$Ca_5(PO_4)_3F$	1.67
Tetracalcium phosphate	$Ca_4(PO_4)_2O$	2.0

The strengthening of the ceramic calcium phosphate is produced when, after hydrolysis of calcium phosphate compounds hydroxyapatite precipitates.

3. SYNTHESIS OF HYDROXYAPATITE BY USING A SINGLE CALCIUM-PHOSPHATE REACTANT

For this purpose it can use all phosphocalcic substances shown in Table 1, whose Ca / P ratio is lower than that of hydroxyapatite. [1]

Hydrolysis reactions of these materials result in H_3PO_4 as a by-product, such as the use of monohydrate phosphate monohydrate, calcium hydrogen phosphate, octocalcium phosphate or tricalcium phosphate:

$$5Ca(H_2PO_4)_2.H_2O \rightarrow Ca_5(PO_4)_3OH + 7H_3PO_4 + 4H_2O$$
$$5CaHPO_4 + H_2O \rightarrow Ca_5(PO_4)_3OH + 2H_3PO_4$$
$$5Ca_8H_2(PO_4)_6.\ 5H_2O \rightarrow 8Ca_5(PO_4)_3OH + 6H_3PO_4 + 17H_2O$$
$$5\ Ca_3(PO_4)_2 + 3H_2O \rightarrow Ca_5(PO_4)_3OH + H_3PO_4$$

Since, after a long time since the reactions described above, the phosphocalcic compounds used as reactants (e.g., calcium phosphate) are found to be excess in solution, the composition of the solution remains on the isothermal solubility of these reactants. [1]

However, the accumulation of H_3PO_4 in time, in reaction solution, will decrease the pH value and also to reduce the degree of supersaturation with hydroxyapatite. Under these conditions, the hydrolysis reaction will stop when the isotherms of solubility of the two compounds present in the solution will intersect Figure 1 (a and b) (intersection of the hydroxyapatite isotherm with the calcium hydrogen phosphate anhydrous, which is a single point) because the solution becomes saturated in both salts (hydroxyapatite and the reactant, respectively).

Overall, a good hardening bioceramic materials in this category takes place while the hydrolysis reactions occur quickly and achieve a degree of interaction as higher completion percentage. Or, in the case described above, these requirements do not occur in the absence of any additions of acidic or basic nature. [1]

When tetracalcic phosphate is used as the reactant, the hydrolysis process results in calcium hydroxide as a by-product along with hydroxyapatite:

$$3Ca_4(PO_4)_2O + 3H_2O \rightarrow 2Ca_5(PO_4)_3OH + 2Ca(OH)_2,$$

as $Ca(OH)_2$, it influences the increase in the pH value of the solution and consequently the degree of saturation in hydroxyapatite also decreases as shown in Figure 1b.

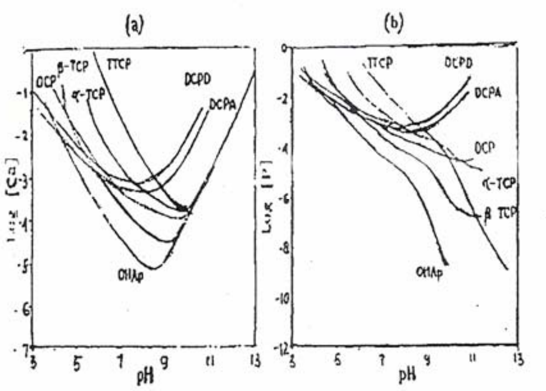

Figure 1. The diagrame of solubility phase to the ternary system $Ca(OH)_2 – H_3PO_4 – H_2O$ at 37^0C, in the case of saturated solutions, depending on the pH value: a.isothermal solubility of the solution based on the total Ca concentration (expressed as log); b.isothermal solubility depending on the solubility of the total phosphorus concentration (expressed as log); OCP=$Ca_6H_2(PO_4)_6$, α - TPC=α – $Ca_3(PO_4)_2$, β- TPC=β-$Ca_3(PO_4)_2$, TTCP=$Ca_4(PO_4)_2O$, DCPA=$CaHPO_4$, DCPD=$CaHPO_4.2H_2O$, OHAp=$Ca_5(PO_4)_3$ .OH

This is explained by the fact that the solubility isotherm has negative slope [2]. The information presented suggests that when using only one calcium phosphate salt as a reactant and precipitats hydroxyapatite, it is necessary to eliminate the H_3PO_4 or $Ca(OH)_2$ by-products to complete the hydrolysis reaction.

3.1 SYNTHESIS OF HYDROXYAPATITE BY USING TWO CALCIUM PHOSPHATE COMPOUNDS

The tetracalcium phosphate $Ca_4(PO)_2O$ is the only salt shown in Table 1 with a Ca/P ratio higher than that of hydroxyapatite. Consequently, this phosphate plays a special role in the production of cement phosphates by being able to react with another phosphocalcic salt (but with a lower C/P ratio) to form a reaction product with apatite stoichiometry. [1]

As a result of this reaction, will not form the acids or bases as a second reaction products result, aspects that results of the interaction of tetracalcium phosphate with anhydrous calcium phosphate or with calcium hydrogen phosphate dihydrate:

$$Ca_4(PO_4)_2O + CaHPO_4 \rightarrow Ca_5(PO_4)_3OH$$

$$Ca(PO_4)_2O + CaHPO_4.2H_2O \rightarrow Ca_5(PO_4)_3\ OH + 2H_2O.$$

From the example described by the first of these reactions, both tetracalcium phosphate and anhydrous calcium phosphate are present in excess, and their rate of dissolution is higher than the rate of hydroxyapatite formation. Accordingly, the composition of the reactant solution is in the vicinity of the point of intersection of the solubility isotherms (singular point) of Figure 1a and 1b, since the process of converting them into hydroxyapatite continues to occur. Under such conditions, the near-constant pH value indicates that the cement setting reaction continues at a constant rate.

The advantage of using tetracalcium phosphate and anhydrous calcium phosphate or calcium hydrogen phosphate dihydrate respectively as reactants is that the pH values of the singular points are very close to the physiological pH value - which contributes to achieving a good biocompatibility, a prerequisite for biomedical applications. The biomaterials thus obtained have the property of complete setting to 37^0 in 4 hours. [3, 4]

4. MICROSTRUCTURE

Electron microscopy studies have shown that cements produced by the reaction between tetracalcium phosphate and anhydrous calcium phosphate are characterized in the first part of the setting process through a morphology where there is an "amorphous" phase present in the interstitial spaces. [3]

In fact the crystalline phase consists of small flat formations consisting of hydroxyapatite, which is formed during the setting reaction of the cement and, at the same time, the property to adhere to one another during the setting process.

These crystalline formations in a quantitative increase in time division at the end of this curing process the morphology of the ceramic biomaterial consists essentially of needle shaped crystals with flat crystals that are present in a smaller quantity.

The crystals formed during the calcium - phosphate cement setting is very small (about 50 nm thick and 100 nm length) are able to adapt perfectly to the tooth surface.

5. CLINICAL APPLICATIONS

The results of experiments carried out on animals have shown [5], as it was expected that tetracalcium phosphate cements based on calcium phosphate anhydrous or hydrated acid are not toxic and does not cause such genetic mutations.

Experimental studies on dogs and monkeys have shown that these types of cements used to obturate dental canals have been well tolerated by periapical tissue [6], or even the formation of new bone formation has been found. [7]

The use of these ceramic biomaterials as implants and various other types of bone tissue did not reveal rejection phenomena.

At the same time, it has been shown that, over time, these implants are progressively replaced by the formation of new bone tissue. [8]

5. CONCLUSIONS

The phosphate cements presented in this paper consist of compositions capable of self-setting reaction and with a very good biocompatibility. Almost perfect adaptation of these biomaterials in tissue surface and an optimal resorption, followed by generating new bone formation, is the distinct advantages of these biomaterials.

REFERENCES

[1] Chow, C.L, Journal of the Ceramic Society of Japan, 99/10/, 954-964, 1991.

[2] Chow, C.L, s.a. – Mat.Res. Symp.Proc., 179, 3-24, 1991.

[3] Fukase, Y., s.a. – J.Dental.Res., 69, 1852-1856, 1990.

[4] Dei, Y, s.a. – J.Japan Soc.Dent.Mat. Devices, 6, 53-38, 1987.

[5] Gruninger, C.,s.a. – J.Dent. Res., 63, (Special Issue) 200, Abstr.no.270, 1984.

[6] Hong, Y.C., s.a. – J. Biomed.Mat. Res., 25, 485-489, 1991.

[7] Sugawara, A., s.a. – J.Dent.Res., 69, (Special Issue), 312, Abstr.no.1628, 1990.

[8] Constantino, P.D., s.a. – Arch. Otolaryngol. Head Neck Surg., 117, 379-384, 1991.

DE GRUYTER OPEN

The Scientific Bulletin of VALAHIA University
MATERIALS and MECHANICS –Vol. 15, No. 13

DOI 10.1515/bsmm-2017-0015

POROUS METALLIC BIOMATERIALS PROCESSING (REVIEW) PART 1: COMPACTION, SINTERING BEHAVIOR, PROPERTIES AND MEDICAL APPLICATIONS

Ileana Nicoleta POPESCU [1], Ruxandra VIDU [2,3,*]
Vasile BRATU [1]

[1]Valahia University of Targoviste, Faculty of Materials Engineering and Mechanics, Str. Aleea Sinaia, No. 13, Targoviste, Romania
[2]University of California, Davis, Electrical and Computer Engineering, One Shields Ave, Davis, USA
[3]University POLITEHNICA Bucharest, ECOMET-UPB, 313 Splaiul Independentei, Bucharest, Romania

E-mail: pinicoleta24@yahoo.com, *rvidu@ucdavis.edu

Abstract. *Over the last few decades, researchers has been focused on the study of processing using different methods of new biocompatible and/or biodegradable materials such as permanent or temporary medical implants in reconstructive surgery. The advantages of obtaining biomedical implants by Powder Metallurgy (P/M) techniques are (i) obtaining the near-net-shaped with complex forms, (ii) making materials with controlled porosity or (iii) making mechanically resistant sintered metallic materials used as reinforcing elements for ceramic/polymeric biocompatible materials. In this first part of the 2-part review, the most used and newest metallic biomaterials obtained by P/M methods are presented, along with their compaction and sintering behavior and the properties of the porous biomaterials studied in correlation with the biomedical domain of application.*

Keywords: *Porous metallic biomaterials, Powder Metallurgy (P/M) techniques, Compaction-Sintering behavior, Biomaterias properties, Medical applications.*

1. INTRODUCTION

Metallic biomaterials such as stainless steel, magnesium, tantalum, titanium etc, have been widely used in many medical applications [1-9] for their good biocompatibility, good electrical conductivity, high strain energy (toughness), good wear resistance and outstanding combination of strength and ductility, compared with other materials. In terms of corrosion resistance, the most used metallic biomaterials are 316L stainless steel, Co-based alloys, and Ti-based alloy. Recent studies have shown that Zr-based alloys could be used as potential material for implants [2-11]. These characteristics along with relatively simple and common fabrication techniques (casting, forging, machining), or alternative conventional/advanced Powder Metallurgy techniques make metallic biomaterials suitable candidates for medical applications.

Biomaterials are used in orthopedic load-bearing application (e.g. screws, bone plates and joint replacement), as well as in cardiovascular devices and dental implants (e.g. artificial hearts, cardiac valve prostheses, vascular stents etc.), as porous scaffolds or neuro-vascular implants (aneurysm-clips). In the last years, biodegradable materials based on Mg, Fe or Zn for temporary implants such as stents and orthopedic fixation elements were also developed [1-11]. In Figure 1, the most used metallic biomaterials in the medical field are presented.

Porous materials are important for biomedical applications because they provide two major benefits for long-term clinical performances: (i) the porous structures on metallic materials allows for the bone to grow into the holes and help the artificial implant to lock in place and (ii) the rough surface acts as an interface for the stress transfer from the bone to implant. Also, porosity decreases material modulus of elasticity closer to those of human bone, which prevents the stress-shielding effect and enhances mechanical biocompatibility. The interconnected or open-cell porosity is more advantageous because it allows transport of body fluid through the implant to the healing tissue and will help adhesion of the cell while maintaining the growth of the cell into implant [3, 10, 12]. The general advantages of porous materials are *property combinations* and *tailoring of properties* [13]. In the first case, we can achieve unusual properties by combination; the porous metals can be thought of as composites and can display some of the properties of metals (such as high electrical and thermal conductivity, ductile failure at high stress, etc) with some of the properties of a porous structure (such as permeability to fluids, low density, etc) [13,14]. The second advantage refers to the properties that can be tailored to suit a certain need of a particular application and depends on the properties of both constituents: the metal in dense (non-porous) form, the metal with a porous structure. As a result, small structural changes can be used to adjust the properties (within certain limits), allowing the precise properties that are required to be obtained [13-15].

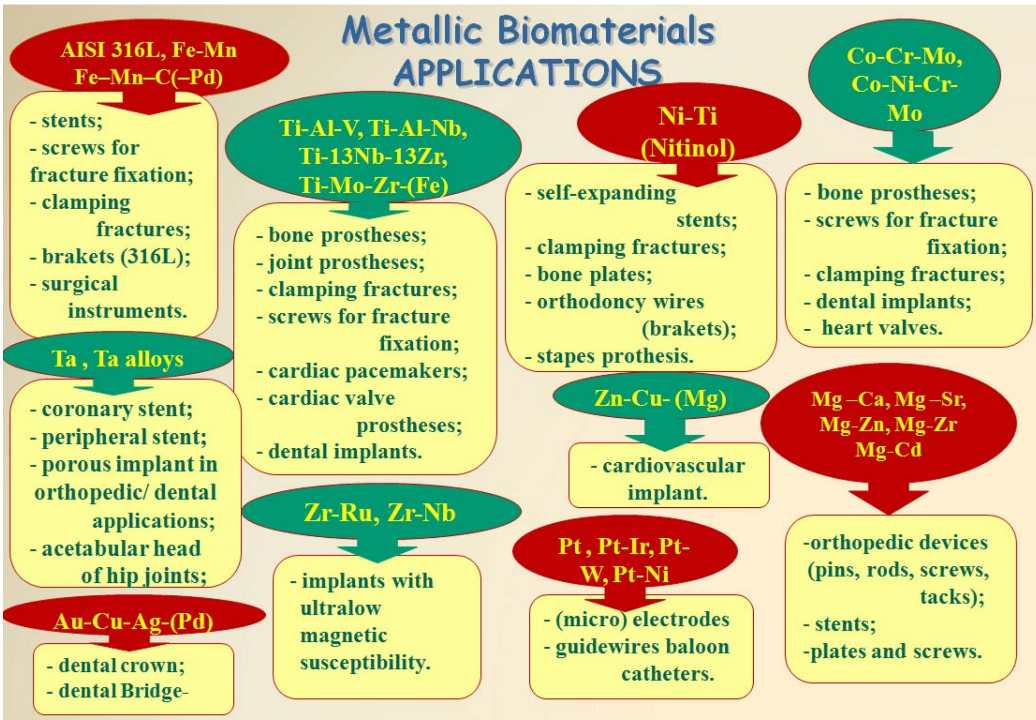

Figure 1. Schematic metallic biomaterials applications in medical fields

Porous metallic biomaterials are used as porous implants in living tissues. There are three distinct types of porous implants: (1) partly or fully porous-coated solid substrates; (2) fully porous materials; (3) porous metal segment joined to a solid metallic part [15-18]. Implants are designed with solid cores and porous coating when mechanical strength is required to stand physiological loads [15]. Porous metallic biomaterials can be made using different powder-based fabrication methods of porous alloys, such as: Conventional Press-and–Sinter Techniques [1, 3, 16, 19, 20-36] combined or not with advanced P/M methods. Considering the advanced P/M techniques, many other methods have been developed over time to obtain porous or non-porous biomaterials, such as: Hot Isostatic Pressing (HIP) [1, 3, 13, 14, 22, 34-42], Porous Coatings such as: Vacuum Plasma Spraying (VPS), or Spark Plasma Sintering (SPS) [13, 14, 22, 40, 43- 46], Microwave Sintering [10, 22, 47, 48], Reactive Sintering (including Self-Propagating High Temperature Synthesis, SHS) [3, 14, 49-52], Additive Layer Manufacturing (Selective Laser Melting/ Sintering (SLM/SLS) or Electron Beam Melting (EBM) [5, 10, 13-15, 20, 22 , 36, 40, 53-56]. Additionally, advanced P/M techniques also use Metal Injection Molding (MIM) [13, 18, 22, 36, 56-61], Space Holder Method [3, 13, 15, 20, 39, 48, 62, 63], Foaming of Metallic Powders [3, 10, 13-15, 20, 39], and Replication Method [14, 15, 20].

All these types and properties of the metallic biomaterials studied in correlation with the biomedical domain of their applicability are important aspect of the study of materials and are briefly presented in the following sections of this paper**.**

2. METALLIC BIOMATERIALS USED IN MEDICAL APPLICATIONS

Iron-based alloys are considered very good candidates for biodegradable medical materials [1]. Alloys are of interest as biodegradable medical materials due to the fact that neither the corrosion rates nor the mechanical properties of pure iron do not meet the criteria required for medical use. Therefore, alloying can improve both corrosion rate and mechanical properties [64]. *The Fe-Mn system* is investigated as a promising material for biodegradable stents [1, 4, 29-31], and *Fe-P system* seems to be interesting for the temporary replacement of bones [32]. Both phosphorus and iron are biogenic elements, so that the human body should tolerate well the implant itself and the decomposition products. Phosphorus brings into the picture an additional beneficial effect between osteogenic cell populations and Fe-P alloy. P-alloying of Fe allows controlling mechanical properties and corrosion rate [27].

Currently, metallic biomaterials used for long-term implantation are *SS 316L* corrosion resistant alloys as the most widely used alloy and it is often considered the standard reference for mechanical properties in developing new biomaterials. Over time, SS 316 L has been used as implant in medical field for joint replacement, screws and bone plates for fracture ficxations. According to Dewidar's study [16] the lifetime of hip synthetic hoints is about 10 years, due to polymer degradation, wear of metallic materials or other factors. Because to the growing number of young people (up to 40 years of age) with osteoarthritis, the demand for such implants that have a life more then 25 years has increased [16].

Co-Cr alloys are used for artificial joints including hip joints and knee due to their biocompatibility and high corrosion resistance and wear-resistance. Co-Cr alloy has been widely used in the manufacture of stents and other surgical implants as Co-Cr alloy demonstrates excellent biocompatibility with blood and soft tissues. Cobalt-chrome has a very high specific strength and is commonly used in dental implants, and orthopedic implants [5]. In comparison with other biomaterials used in medical applications such as stainless steel and Ti alloys, the wear resistance of Co alloys is higher. The head of the joint in the artificial hip joints is exposed to wear. Thus, high strength and ductility Co alloys, such as *Co-Cr-Mo alloys* were used in hip joints. To increase the resistance to wear of these alloys, carbide has been dispersed in Co alloys [5, 65].

Titanium alloys are the most attractive metallic materials for biomedical applications. Examples include pacemakers, cardiac valve prostheses, artificial knee joints, bone plates, artificial hip joints, screws for fracture fixation and valve of artificial hearts (Figure 1). Titanium alloys with aluminum and vanadium (Ti-6Al-4V) have been widely used as implant materials, but certain studies revealed that the release of the Al and V ions can be harmful to the human body [5, 12, 17]. Consequently, other alloy stabilizers were searched to decrease the hostile biological impacts. Also, introducing biocompatible alloying element could improve the mechanical properties of the implant. That is why V and Al-free alloys have been announced for implant applications, based on the Ti-6Al-4V (ASTM F 1295, ISO 5832-11) implants. New alloying elements in Ti alloys are tantalum (Ta), tin (Sn), niobium (Nb), and zirconium (Zr) [12, 66], to form new biocompatible Ti based alloys as: Ti-6Al-7Nb (ASTM F1295, ISO 5832-11), Ti-13Nb-13Zr (ASTM F1713), and Ti-12Mo-6Zr-2Fe (ASTM F1813-97) [5, 66]. The choice of these new alloying elements is based on the fact that they are non-cytotoxicity elements that have revealed good corrosion resistant and biocompatibility, and they form solid solution with Ti. [12, 66**]**

Nickel-Titanium Alloys have the property to trans-form plastically deformed specimens in to their original shape by just heating it. This feature is called the shape memory effect. Some biomaterials applications where the shape memory effect is required are as follows: orthodoncy wires, dental bridges, self-expanding stents, and orthopedic prostheses to artificial heart.

Porous NiTi shape memory alloys have recently attracted extensive interest for their potential use as biomedical materials. Stress–strain behaviors of porous NiTi alloy [21] fabricated by element powder sintering in argon atmosphere and investigated by compression and flexural tests has indicated that the ultimate compressive strength and the flexural strength of the porous NiTi alloy depended on the densities of the porous NiTi alloy and the sintering conditions [19, 21].

Nickel-Chrome based Dental Alloys. At present, Ni-based alloys are increasingly used for economic reasons as substitutes for precious metal dental alloys. In terms of their biocompatibility, although new requirements and limitations have been imposed by the European Union on the use of dental alloys, especially Ni-Cr alloys, the demand for such materials is increasing.

Thus, in this context, recent studies and researches have been made regarding corrosion behaviour, cytotoxic effects or inflammatory response on 8 Ni-Cr dental alloys [67]. The results of research have shown that the amount of nickel ions released is higher than EU required limitation, but the corrosion behavior was poor. Also, biological tests on Nickel-Chrome based dental alloys revealed that: there are no cytotoxic effects on Hella and L929 cells, nor do they have a pro-inflammatory response in endothelial cells [67].

Tantalum alloys. The open-cell porous Ta materials are best suited for use as coatings or non-load-bearing implants because of their low mechanical properties. Recent studies (e.g. in vitro, in vivo, and clinical) have demonstrated that tantalum is a bioactive metal that recommended it as a promising metal for load-bearing orthopedic applications [68]. Tantalum is a ductile, hard, and chemically resistant material with good apposition to human bone. Tantalum spontaneously form a passive oxide layer with a very good adherence to the metal, which facilitate the bone in-growth under *in vivo* conditions via the development of bone-like apatite that promotes hard- and soft-tissue adhesion [69]. Generally, both bulk form (usually porous) and in coating form are available for the tantalum based implants, depending on the required application [62].

Magnesium alloys are of great interest as new degradable biomaterials. The foremost advantages of magnesium alloys used as provisional biomaterials are their biocompatibilities and good mechanical properties. *The magnesium and Mg alloys* are lightweight metals (1.74 to 2.0 g/cm^3). The elastic modulus (41–45 GPa) is close to that of the bone while the fracture toughness of magnesium is greater than ceramic biomaterials, which avoids the stress shielding effect. Magnesium is the fourth most abundant cation in the human body and it is essential to human metabolism. Research directions of the biomedical magnesium alloys are built on both self-designed biomedical and industrial magnesium alloys system [70].

Zinc alloys. The newly developed *Zn-xCu binary* alloys (x = 1, 2, 3, and 4 wt%) could be promising candidates for biodegradable cardiovascular implant application due to their excellent combination of strength and ductility, low degradation rates, acceptable cytotoxicity and good antibacterial property [71]. In the work of Vojtech *et al.* [6], *Zn-Mg alloys* containing up to 3 wt% Mg were studied for their mechanical and corrosion properties and were compared with pure Mg, casting Zn-Al-Cu and AZ91HP alloys, as potential bio-degradable materials. Mechanical properties (tensile and hardness) were discussed in correlation with the structural features of these alloys and they found that the corrosion rates of the Zn-Mg alloys were lower than those of pure Mg and AZ91HP alloys. Zn-Mg alloys corroded at rates of the order of tens of microns per year, while the corrosion rates of Mg and AZ91HP alloys were of the order of hundreds of microns per year. Zinc toxicity was assessed from the corrosion performance and it was found that the toxicity is minor compared with the tolerable biological daily limit of zinc [6].

Zirconium *(grade 702, 99.2%)* is not commonly used as a medical material, but has several properties in common with titanium and it is chemically closely related to it. For example, both are transition metals with similar outer shell valence electron structure. They both are typically covered by thin, chemically stable, surface oxides. However, most chemical and physical properties, such as oxidation rates, transport properties, crystal structures, and water interactions of the two metals and/or their oxides differ quantitatively [72].

***Zr–Ru** alloys* with various content of Ru were proposed and fabricated for new biomedical Zr alloys with ultralow magnetic susceptibility, enhanced mechanical properties, improved corrosion resistance, excellent biocompatibility and Magnetic Resonance Imaging (MRI) compatibility. Li *et al.* [11] have demonstrated that both the Yield Strength (YS) and the Ultimate Tensile Strength (UTS) of the Zr-Ru alloys are higher than that of pure Zirconium. Also, Ru alloy additions improved the corrosion resistance of pure Zr. Furthermore, the breakdown potentials (Etran) of Zr-Ru alloys are much higher than that of pure Zr, indicating the enhanced pitting corrosion resistance by adding the Ru alloying element. Among the Zr-Ru alloy series, Zr-1Ru is the optimal Zr-Ru alloy system as therapeutic devices under MRI diagnostics environments [11].

Niobium alloys. Nb and Zr are desirable elements in biological systems and biomedical applications thanks to their biocompatibility, resistance to corrosion, mechanical integrity and ionic cytotoxicity. The synthesized nano/sub-micron grain structured Nb-Zr alloy exhibited higher corrosion resistance in Simulated Body Fluids (SBF) medium, implying that these alloy specimens can be used as excellent implant materials [73].

Gold* and *gold alloys are useful metals in terms of stability, corrosion resistance, odontotherapy (because of its long-lasting). Since gold alloys have more mechanic property than pure gold, it is subjected to alloying process. These alloys consist of 75% or more than 75% gold, the remaining is comprise of noble metals. Copper increases strength, platinum also increases strength, but if it add more than 4%, the processing of this material gets difficult due to increase in melting temperature. Soft alloys which have more than 83% gold are used as packing material [5].

Gold is distinctly different from the other two metals (Zr and Ti). It is a noble metal which does not form surface oxides (except under extreme conditions). Thus, it exposes a real metallic surface to the biological environment, in contrast to titanium and zirconium which expose oxide (i.e. ceramic) surfaces. The surfaces of gold, zirconium and titanium have in common the fact that they are chemically very stable and highly corrosion resistant in most environments and therefore products released from the implants would probably not influence the biological response [72].

Platinum is inert. Unlike other metals, such as copper and nickel, platinum does not decompose inside the body and does not cause allergic reactions. Platinum can be fabricated into very tiny, complex shapes and it has some important properties not shared by base metals [74].

Platinum alloys have low corrosion rates, high biocompatibility and good mechanical resistance which make them suitable for medical applications [75]. Platinum biocompatibility makes it ideal for temporary and permanent implantation in the body, a quality which is exploited in a variety of treatments in addition to the heart implants, such as: catheters containing platinum components to detect the cardiac arrhythmia, Pt-Ir alloy rings for shocking electrodes, guidewire with coiled Pt-W tip and marker band (Pt, Pt-Ir or Au) of balloon-mounted stent used in percutaneous transluminal coronary angioplasty [74].

3. CONVENTIONAL PRESS-AND-SINTER METHODS OF POROUS ALLOYS

Powder Metallurgy (P/M) techniques has the advantage, in comparison with casting methods, to form near-net-shaped products and also to allow obtaining porous materials with tailored porosity, pore size and pore distribution [3]. The well-known technological steps of P/M are obtaining the raw material, dosing and homogeneous mixing of powders followed by their consolidation. Mixing depends on various factors, such as those related to powder characteristics, especially the different component densities. Consolidation can be accomplished by pressure-based densification (e.g., die pressing), densification based on sintering (e.g. MIM) or densification combining both press and simultaneous heat treatment (HIP). Following the application of P/M techniques, 80% densification of the powders can be obtained, resulting a dense, non-porous material. In this case, PM is advantageous to other techniques for obtaining materials with complex configurations at the final shape, so minimizing costs by eliminating intermediate operations.

Powder metallurgy has developed in the medical field as a technique alternative to conventional ones, especially in the production of materials for bone implants in surgery, such as in orthopedics and dentistry. In the latter two areas it is necessary load bearing ability and especially a rigid fixation of the implant to the bone [10].

The porous implants provide a more efficient fixation compared to dense materials due to the bone host via the growth of new bone tissue into the pores.

The porous implants provide a better fixation of implants to the bone host via the growth of new bone tissue into the pores.

Porosity resulting from powder metallurgy processing gives a decrease in the Young's implant module, and surrounding bone, thereby improving the fixation [16].

Sintering process is a key process in the P/M technology because furnace atmospheres affect the sintering development and the material being treated. The main mission of the process is to prevent the metal from coming into contact with the air. The properties of the porous or dense implants using P/M technique are dependent on processing parameters and the sintering atmosphere [16]. In addition, P/M could be advantageous for metallic biomaterials like Ti, Mg or Nitinol, which are difficult to machine by conventional methods [52, 65].

P/M of Porous 316L Stainless Steel. Montasser Dewidar [16] studied the effect of sintering parameters on densification behavior, micro-structure, properties (mechanical and tribological) of Porous SS 316L with possible utilization in artificial knee or hip joints.

In Figure 2, the processing steps of fabrication of porous 316L stainless steel is schematically presented.

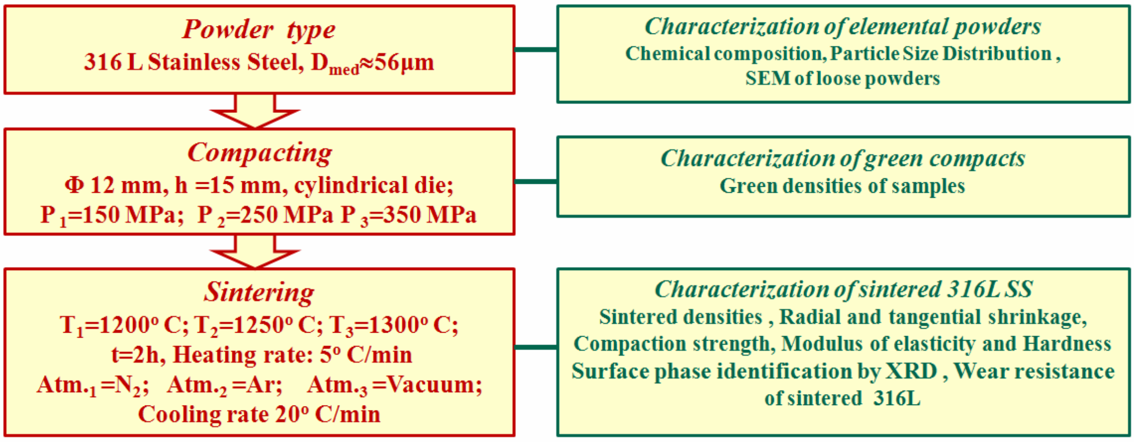

Figure 2. Process flow diagram for processing porous 316L stainless steel by P/M. Adapted after Reference [16]

In Figure 3, the compressibility curve of 316L stainless steel powder is presented, showing that low applied pressures (between 150 MPa and 350 MPa) have been used to obtain samples with high porosity [16]. The compacted powder (SS 316L powders without lubricant addition) , increases with increasing of applied pressure. Was obtain a minimum density (4.4 g/cm^3) for applied pressure of 150 MPa (corresponding to 55% of theoretical density) and the highest value of density from experimental study, at 350 MPa was 5.12 g/ cm^3 (corresponding to 64% of theoretical density) [16].

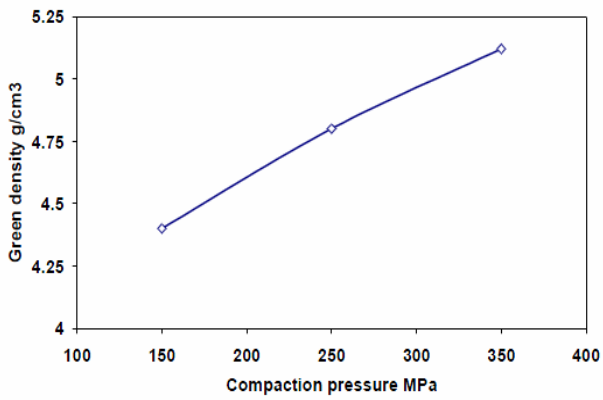

Figure 3. The compressibility curve of 316L stainless steel powder [16].

In Figure 4 the effect of sintering temperature and sintering atmosphere on the compressive yield strength (a), compressive modulus of elasticity (b), and hardness (c) of 316 L samples compacted at 350 MPa are presented. These results [16] led to the following conclusions:

(i) the sintered SS 316L at the all three sintering temperatures had porosity values ranging from 39.25 % to 11.87 %;

(ii) the mechanical tests showed that as the porosity increases, both the modulus of elasticity and the strength of the material decrease;

(iii) the most efficacy sintering atmosphere used in processing of porous 316 L stainless steel (with highest strength, wear resistance and hardness values results obtained) was nitrogen atmosphere and

(iv) the optimum sintering temperature in nitrogen atmosphere was 1300 °C.

These mentioned above processing parameters and optimum results (mechanical properties, density and wear resistance) make the obtained porous 316 L SS suitable for use as biomaterial in hard-tissue applications.

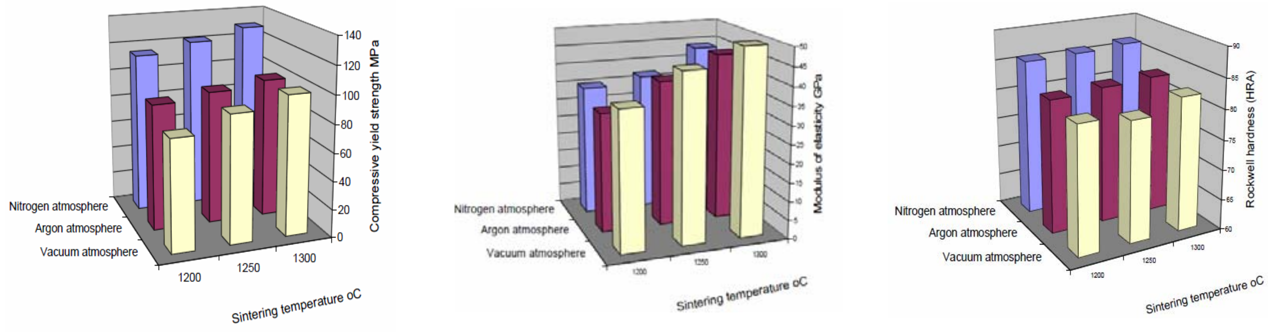

(a) (b) (c)

Figure 4. The effect of sintering temperature and sintering atmosphere on (a) Compressive yield strength; (b) Compressive modulus of elasticity; and (c) Hardness of 316 L samples compacted at 350 MPa [16].

P/M of Biodegradable Fe-Mn. Hermawan *et al.* [4, 29, 30] was the first researchers that studied biodegradable iron-manganese alloys with future applicability in the medical field, as implants in the cardiovascular system.

Hermawan [30] obtained the Fe-Mn alloys by P/M processing, and he pursued the fulfillment of the following targeted properties: (a) good mechanical properties (yield strength more than 190 MPa, maximum elongation higher than 20%); (b) physical properties (non-ferromagnetic and magnetic properties comparable with SS 316L), and (c) controlled degradation process and biological performance (non or less toxic elements, etc.). One of the reasons for choosing the manganese as alloying element was that it is an essential element of the proper functioning of living organisms, it is nontoxic, and as an alloy, Fe-Mn alloys are nonmagnetic. In Figure 5 the schematic P/M processing route of *Biodegradable Fe-Mn alloy* for biodegradable stents applications is presented [30].

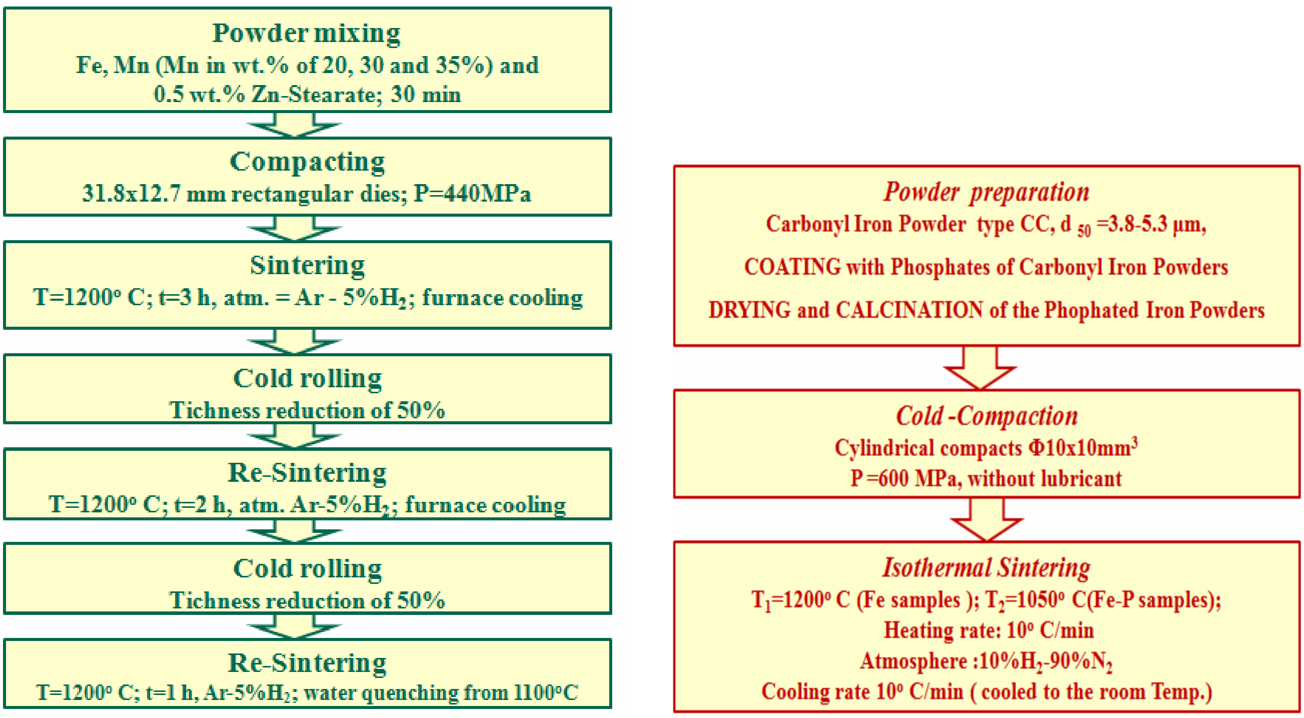

(a) (b)

Figure 5. The schematic P/M processing route of (a) Fe-Mn alloy for biodegradable stents applications. Adapted after [30]; (b) Fe-P alloy for biomedical applications. Adapted after [27]

It has been developed an experimental program to achieve the above mentioned objectives. Thus, were investigated four types of iron-manganese alloys (with 20, 25, 30 and 35 wt%) from microstructure, mechanical properties, magnetic properties and degradation point of view[30]. The results showed that their microstructure is mainly composed of γ phase with the appearance of ε phase in alloys having low Mn content. The yield strength was 234 MPa, and 421 MPa for the Fe–35%Mn alloy and Fe-20%Mn alloy, respectively, elongation for Fe–35%Mn alloy was 32% but for Fe-20%Mn was 7.5%. The magnetic susceptibility in the quenched condition for these type of alloys was similar and remains constant after plastic deformation, with exception of Fe–20%Mn alloy. In comparison with pure iron, the corrosion rate was slightly higher. The tests' results on the four alloys showed that the optimum alloy for biodegradable stent application is Fe–35%Mn alloy. In terms of mechanical properties Fe-30Mn and Fe-35Mn alloys (the alloys that contained single austenitic phase) are closest to 316 L stainless steels. In addition, the iron based alloys with 30 and 35 % Mn have the degradation rate two times higher in comparison with pure iron, and also they have low inhibition in the metabolic activity of fibroblast cells during the cell viability studies. All these results make these obtained Fe-Mn alloys [30] suitable for application as coronary biodegradable stent in *vitro* and *in vivo* conditions.

The Fe-P biomaterials prepared by *powder metallurgy process* (see Fig. 5b) starting with a new class of powders, i.e. carbonyl-iron particles coated with a layer of phosphates, were studied by Kupková *et al.* [27]. The aim of their work was to investigate how the phosphorus addition in an amount of 0.5 wt% and 1.0wt% to the iron powder as a coating layer affected the microstructure of sintered samples and their corrosion behavior in Hank's solution.

The obtained microstructure (Figure 6) can be described as a spatial network of globalized iron particles or iron oxides surrounded by a solidified liquid phase consisting of a variety of ferric phosphates [27].

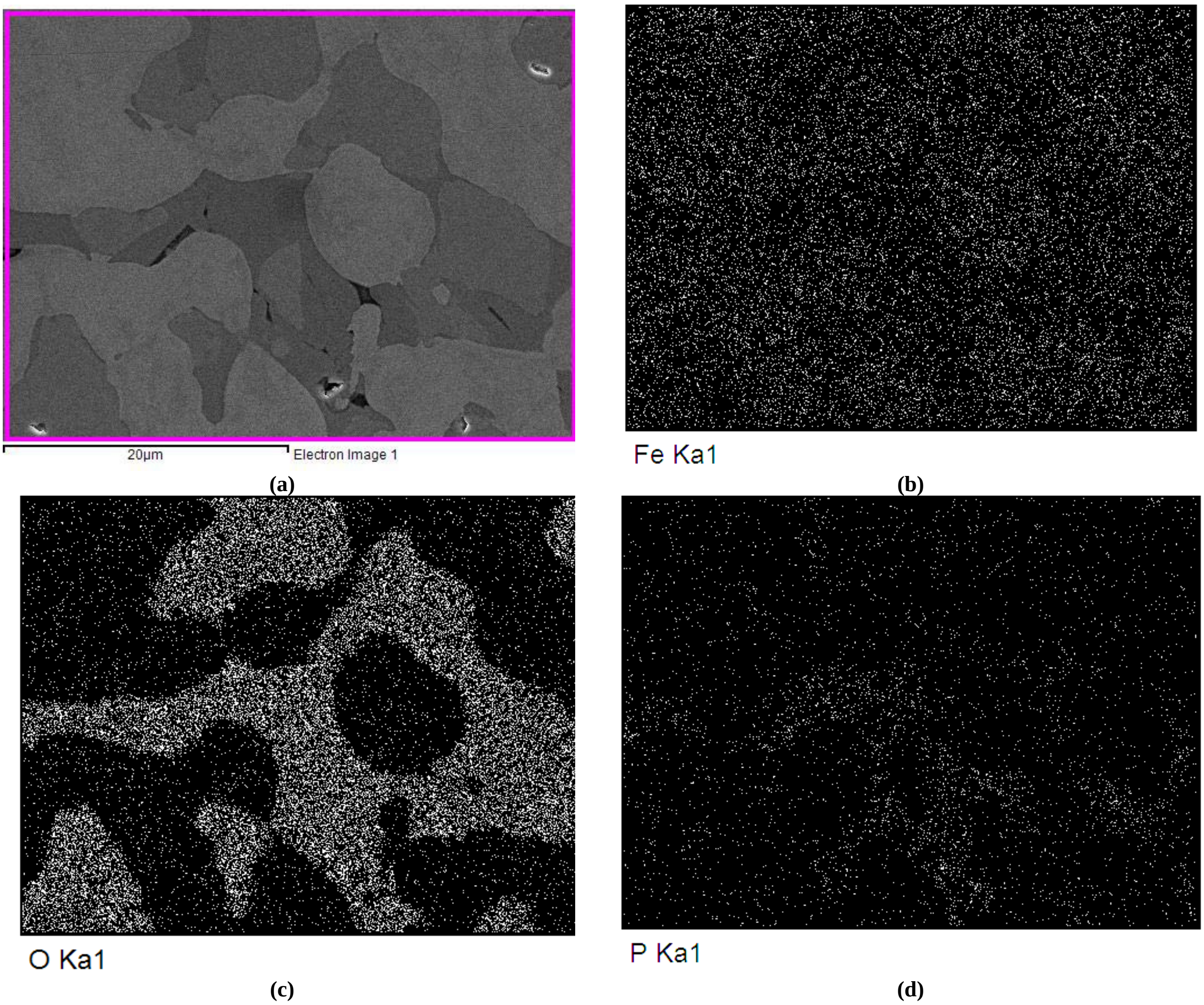

(a) (b) (c) (d)

Figure 6. SEM micrographs of a polished section of Fe-1.0P sintered compact (a) and the EDX mapping of the distribution of (b) iron, (c) oxygen and (d) phosphorus within this microstructure [27]

The results showed that the addition of 0.5 by weight of P give in a positive displacement of the corrosion potential at steady state and the addition of 1.0% by weight of P resulted in a slight negative displacement of the corrosion potential of the electrodes submerged in Hank's solution with respect to the corrosion potential of un-deped iron.

It was found from the electrochemical experimental results that the corrosion rate is higher for *Fe-1.0P* material in comparison with *Fe-0.5P alloy.*

A porous structure of the sintered iron sample allowed the rate of degradation to be increased relative to the "bulk" iron.

The Fe-0.5P sample showed the lowest corrosion tendency with a corrosion rate similar to that of the Fe-1.0P sample. Also they proposed future investigations to better understand the degradation of PM iron-phosphorus biomaterials in simulated body fluids, as well as to verify the practicality of the fractal geometry for the analysis of corrosion phenomena [27].

Commercially pure (CP) Ti and Ti based alloys can be obtained from powders through a variety of techniques, such as: press-and-sinter, press-sinter-and-hot-work, hot isostatic pressing, extrusion or direct roll compaction of loose powders, hot-press-and-machine and metal-injection-molding-and-sinter. *The press-and-sinter route* is the most attractive approach due to its simplicity and cost. The main difficulties of processing by casting when molten Ti reacts with most metallic and non-metallic materials used as crucibles for melting, and high purity argon atmosphere is required in the crucible and in the mold during melting and casting, make Ti P/M attractive. In addition, there are mechanical property advantages of finer grain size and greater chemical homogeneity for titanium parts made from powders [22, 23].

Compaction of titanium powder can be carried out at room temperature using standard presses in closed steel dies. For a better compaction, the irregular shape of sponge fines is recommended. The compaction behavior of sponge Ti powder shows a rapid increase in green density with compaction pressure up to 690 MPa, after that remaining constant. At 690 MPa the resulting green density is above 80% of the theoretical density. Similar compaction behavior and pressing characteristics have been observed for fine electrolytic titanium powder (250 µm), coarse electrolytic titanium powder (250–1000 µm), and fine titanium powder (< 30 µm) reduced by calcium hydride (CaH_2) except that the 80% theoretical density occurred at a lower compaction pressure, 500 MPa [24]. The pressing characteristics of a powder mixture, for the preparation of alloys via a blended elemental (BE) route, are, in general, determined by the base titanium powder, but may also be affected by the form of the alloying element powders. In the literature, there are numerous experimental data regarding the effect of particle size and size distribution on the green density [25]. The high green density obtained from titanium powder or BE powder mixtures at pressures < 700 MPa by cold pressing ensures good green strength, which is essential for the safe and rapid ejection of green shapes from various die cavities and their subsequent handling prior to sintering. Cold-pressed titanium green parts was sintered in the past in argon at 50 mm mercury pressure, but nowadays they are usually sintered in vacuum at pressures of the order of the 10^{-2} Pa because of the chemical affinity of titanium for oxygen, nitrogen, carbon and hydrogen [26].

Torres *et al.* [33] have researched on *Porous Titanium for Biomedical* applications *obtained by Conventional P/M process,* and studied the influence of pressing and sintering parameters on structure and mechanical characteristics of CP Ti grade 4 porous specimens. The microstructure was investigated from porosity point of view (the type , shape, size and quantity of pores).
The mechanical tests consisted in compressive yield strength, and conventional and dynamic Young's modulus investigations. The elastic modulus, both conventional and dynamic, and the yield strength showed the same behavior. In the middle part of the cylindrical samples (the sample results from pressing at 38.5 MPa and sintering at 1000 and 1100 ^{o}C) resulted a better stiffness. An assessment of porosity and elastic modulus on a three-part cylindrical sample showed that it is possible to obtain a titanium sample of graduated porosity that can be used in implant design. This approach opens up a new possibility to solve the bone resorption problems in association with the stress-shielding phenomenon. Bolzoni *et al.* [34] studied the processing of hydride-dehydride elemental titanium powder by conventional Press and sinter method and hot-pressing techniques. For the *conventional P/M route*, the green samples were subjected to uniaxial cold press at 700 MPa using a floating die and zinc stearate as a lubricant for the walls of the die. The sintering parameters used were: sintering temperatures ranging from 900 ºC and 1300 ºC, with a step of 200 ºC for 2 hours, in high vacuum tubular furnace (the minimum vacuum level was 10^{-5} mbar), using a heating and cooling rate of 5 °C/min.

They obtain dense titanium products with properties similar to those of the wrought materials which should reduce production costs and eventually extend the use of titanium in new industrial applications.

Vasconcellos et al. [17] et al. [17] assessed the *in vivo* response of rabbit tibia *to porous titanium scaffolds* and dense titanium samples *prepared by powder metallurgy*. Porous titanium scaffolds were prepared from a mixture of titanium / urea powder having a weight ratio of 80 to 20 percent. The blend was uniaxial pressed under 100 MPa in a stainless steel mold and then isostatically pressed below 200 MPa. The resulting samples were sintered at 1200 ° C / 1h under vacuum (10-7 torr) and then heat treated at 180 ° C / 2h in air to remove the spacer particles.

These parameters were used to prepare dense titanium samples also. The results demonstrated that both titanium devices presented osseointegration, with porous titanium scaffolds showing bone ingrowth in the pores, which augmented over time. These porous structures have promising potential as a biomaterial implant system, considering their interactions with bone cells [17]. Bone growth in porous metal depends on several factors, such as (i) surface porosity, (ii) stability of micromorphism (iii) degree of micromorphism between the implant and bone, whether the host bone is trabecular or cortical and (iv) the presence of gaps between the implant and the bone surface. In their study [17], the tight press fit of the implants into the osteotomic cavity was aimed at minimizing the gap and micro-motion of the implant. Oseointegration is strongly affected by (a) the morphology of the porous structure and (b) the degree of bone ingrowth seems to depend on the size of the pores.

Few research studies have been published on the effect of Mn on Ti-based alloys, especially on second generation alloys such as *Ti–13Nb– 13Zr, Ti–35Nb–7Zr–5Ta, Ti–Mo or Ti– 29–Nb–13Ta–4.6Zr* [63, 76]. One way to obtain *Ti alloys* with lower elastic modulus is to use metallic foams *by a powder metallurgy route*. The use of space holders as a means of tailoring the morphology and properties, particularly stiffness, of titanium foams *produced by the PM* route has attracted significant recent interest.

Development of titanium foams with low Young's modulus as a potential implant by P/M techniques was made by Guerra *et al.* [63]. In their work, the effect of manganese on the mechanical properties of compression of Ti-13Ta-30Nb-xMn foams (x2-6% by weight) has been studied. Titanium alloys obtained from mechanical alloying were processed to produce foams (see Figure 7) using ammonium hydrogen carbonate with a 35 mm average particle size (50% v / v) as a space-holder. Powders and space holder were mixed and uniaxial pressed to form compacts. The space support was removed by heating the green parts at 180° C for 1.5 hours before sintering at 1300° C for 4 hours in argon.

The modulus of elasticity of the foam was lower than that of pure Ti and the yield strength increased with the addition of Mn.

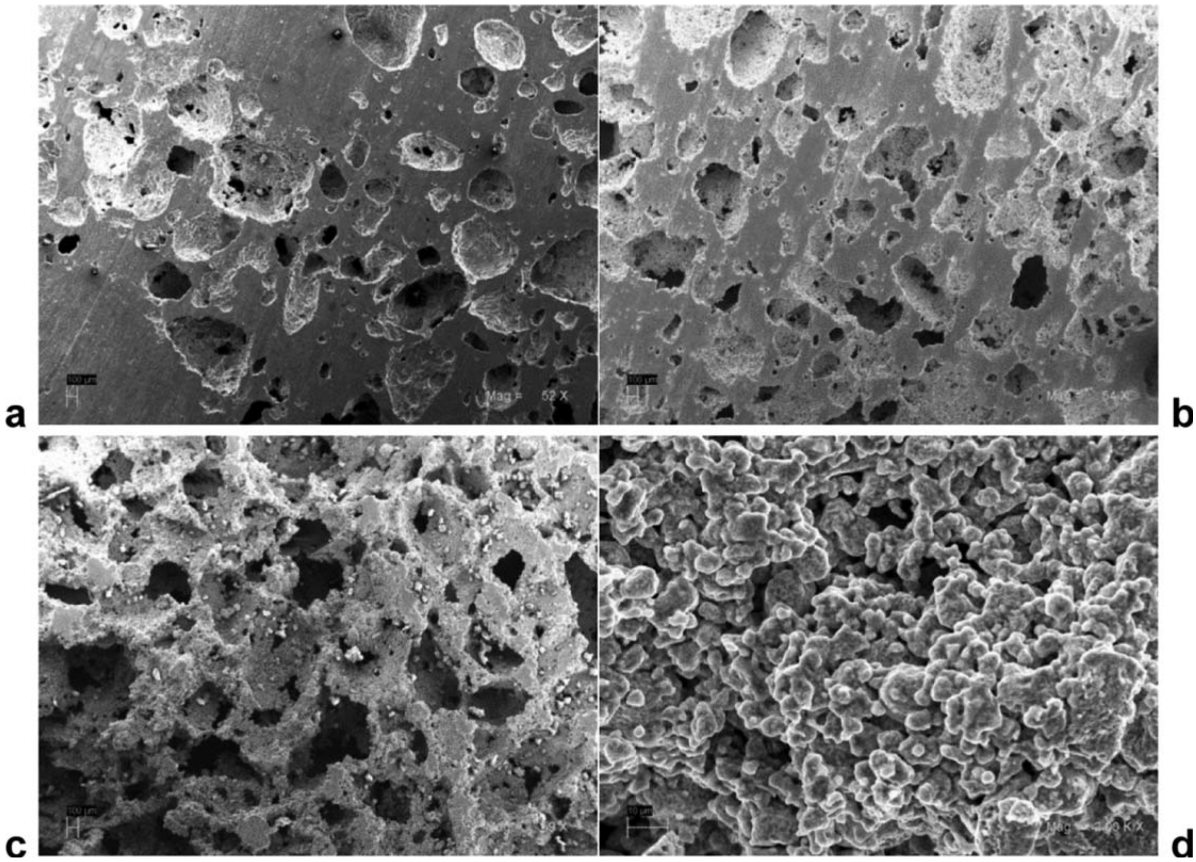

Figure 7. SEM images of foams: (a) Ti–30Nb–13Ta–2Mn; (b) Ti–30Nb–13Ta–4Mn; (c) Ti–30Nb–13Ta–6Mn; (d) small pores produced by sintering process [63]

The increasing number of patients with cardiovascular disease has determined, in the last years, development of extensive researches in developed of different types of biomaterial including shape memory alloys (SMA) used as stents.

Porous NiTi shape memory alloy fabricated by *element powder sintering* in argon atmosphere were investigated by Zhu *et al.* [21] using compression and flexural tests. The results showed that the maximum compressive strength and flexural strength of the porous NiTi alloy depend on the NiTi porous alloy densities and the sintering conditions. In compression experiments, the pre-strain could recover completely while it was less than 2%.

Recovery of the NiTi porous alloy was based on the unique NiTi phase and pore structure. The pores have adverse effects on the recovery of the NiTi alloy form under experimental conditions.

Powder Metallurgy fabrication of ***Co-Based Alloys*** for Biomedical Applications [65] brings several advantages such as reduced machining, possibility of alloying by high-melting elements, preparation of nanocrystalline materials with enhanced mechanical properties *or producing of porous alloys* with improved ability to integrate into issues. *Cobalt-based materials* with improved properties have been *fabricated by means of powder metallurgy.*

When compared with conventional alloys, the samples made by P/M process were found to result in good mechanical properties (high tensile and hardness, fatigue strength) and from structural point of view, fine grain size and more uniform structure that is less prone to segregation.

The P / M processed alloy also offers the same relative benefits even after exposure to high temperatures typically associated with the annealing or forging of hard-tissue implants [77].

In the work of Marek *et al.* [65] they focused on the basic preparation of *Co 28 Cr 6 Mo 0.25 C* by two methods of powder metallurgy. In the first method, pure metal powders were blended, pressed and sintered in a vacuum furnace. The second applied technology consisted of mechanical alloying using a planetary ball mill and compaction by sparking plasma sintering technique.

The preparation by conventional pressing and sintering technique consisted of a mixture of elemental powders of defined purity (Co from MERCK, 99.9%, 1 μm; Cr from Sigma Aldrich, 99.5%, 44 μm; Mo from Penta, 99.9%, 44 μm) and carbon (graphite, 10 μm) and then pressed at 630 MPa in 10 mm diameter green bodies, sintered in a vacuum induction furnace at 1250^{o}C and 1350^{o}C for 4, 8 and 12h. The dependence of the microstructure, phase composition and mechanical properties of samples prepared under the manufacturing conditions (milling parameters, sintering temperature, etc.) was studied.

The results were compared with the properties of the commercially available cobalt alloy used for medical applications. It has been found that simple cold compaction and subsequent sintering did not result in the desired phase composition and therefore the alloys exhibited a high porosity which was responsible for lowering the functional properties. Better results were obtained by using a combination of mechanical alloying and sparking plasma sintering. Thus, the Co28Cr6Mo0.25C alloy exhibited superior mechanical properties compared to the conventional molded counterpart.

Open-cell Porous Tantalum structure, with an appearance similar to cancellous bone (Zimmer Inc, Warsaw, IN) is made by pyrolysis of thermosetting polymer foam, which creates a low –density vitreous carbon skeleton with 98% porosity [68]. Trabecular metal is a portable structure of open porous tantalum, with repeated dodecahedrons, similar to the spongy bone. The pore size and mechanical properties of the Trabecular Metal can be adjusted by modifying the coating thickness of tantalum (40-60 mm). Current Trabecular Metal implants for hard-tissue applications have a porosity of 75-85% with a pore size between 400 and 600 mm. The open- cell porous Ta materials are best suited for use as coatings or non-load-bearing implants due to low mechanical properties. Porous tantalum structures can be prepared by applying the sponge impregnation technique and the powder metallurgy method [78].

Pore structure and morphology of the *porous scaffolds* evaluated by SEM showed that the porosity of the porous scaffolds was 66.7% and the pore size was 300-600μm, presenting a three-dimensional interconnected network (3D) to the cellular structure.

The compressive strength was 61.5±4.5MPa and the elastic modulus of the scaffolds was 2.21±0.16 GPa. The biocompatibility results show that porous Tantalum foam scaffolds can significantly promote the proliferation of rat osteoblasts and that the material was not toxic [78].

Porous Magnesium scaffold or foam for tissue engineering or drug deliver application can be obtained by various techniques such as *powder metallurgy*, laser perforation and unidirectional metal / gas eutectic solidification method (called GASAR process), and negative salt-pattern molding process [79]. The most common solid processing technique for the synthesis of magnesium materials is the powder metallurgy technique [2, 80]. ***The Mg-Zn alloy*** was prepared by *powder metallurgy* of Mg, Zn and Y powders [80]. The powders were mixed manually and compacted uniaxally at 530 MPa to form cylindrical green compacts and then sintered in a tubular furnace under an argon atmosphere.

The sintering temperature was chosen according to the phase diagrams of the individual alloys (MgZn5: 575 ° C, MgZn10: 405 ° C, MgY5: 600 ° C) and the sintering time was 2 hours. For *MgZn5* and *MgZn10* samples, sintering was prolonged up to 4 hours or 24 hours to observe the influence of sintering time on porosity and mechanical properties. The pore forming agent (NH4) 2CO3, which was used in some experiemnts, was removed prior to sintering by thermal decomposition [80]. Magnesium alloys prepared with P / M without a pore forming agent have an adequate elastic modulus and an ultimate compressive strength superior to the natural bones (Figure 8).

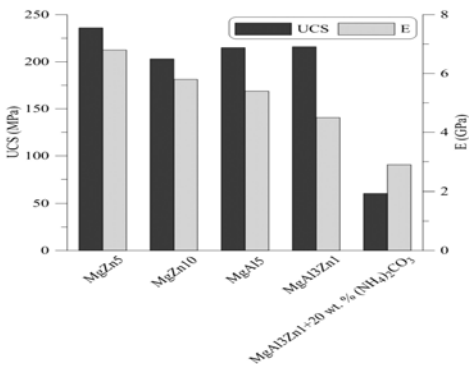

Figure 8. Compressive strength and modulus of elasticity of prepared Mg-Zn samples [79]

The porosity of the samples without the pore forming agent is up to 10% of the volume fractions. About 90% of pores have less than 100 μm diameter.

The number of pores with an equivalent diameter of 200 μm and a pore area fraction increases (18–48 % of the volume fractions) by addition of (NH4) 2CO3 pore forming agent to the MgZn5 and MgAl3Zn1 alloys. The ultimate compressive strength reached ranging 203 to 236 MPa. With the increase in porosity after addition of (NH4) 2CO3, the compressive strength decreased to 61 MPa [80].

4. CONCLUSIONS

The first section of the paper presents various types of metallic biomaterials (both in porous or dense state), used over time or in a laboratory testing stage, emphasizing their characteristics according to a definite medical field of use. The Conventional and Advanced Powder Metallurgy techniques used to make biocompatible and/or biodegradable materials and the advantages of using P/M techniques in comparison with other conventional techniques (i.e. casting methods) have been also concisely presented.

The advantages shown by PM techniques over the conventional methods deals with the control of porosity, pore size and pore distribution. The importance of porous structures of metallic materials is that they provide a better anchoring effect of the artificial implant in the bone by growing a new bone tissue into the pore spaces of the materials. The existence of porosity decreases the elasticity of the implant material closer to those of the human bone, thus preventing the stress-shielding effect and, consequently, improving the mechanical bio-compatibility (binding) of the two dissimilar materials.

Studies of the compaction-sintering behavior of porous metallic biomaterials for use as permanent or temporary implants in reconstructive surgery have also been reviewed, focusing on the effects of processing parameters on physical-mechanical characteristics, wear resistance, corrosion and biocompatibility behavior.

REFERENCES

Journals:

[1] M.Moravej, D.Mantovani, Review. Biodegradable Metals for Cardiovascular Stent Application: Interests and New Opportunities, Int. J. Mol. Sci. 12 (2011) 4250-4270.

[2] F.V.Anghelina, D.Ungureanu, V.Bratu , I.N.Popescu*, C.O.Rusanescu, Fine Structure Analysis of Biocompatible Ceramic Materials Based Hydroxyapatite and Metallic Biomaterials 316L, APPL SURF SCI, 285 A, (2013) 65-71.

[3] J.Čapek, D.Vojtěch, Powder metallurgical techniques for pre-paration of biomaterials, Manuf.Technol.,15(6)(2015),964-969.

[4] H.Hermawan, H.Alamdari, D.Mantovani, D.Dube, Iron-manganese: new class of metallic degradable biomaterials prepared by powder metallurgy, Powder Metall. 51(2008) 38–45.

[5] Ayşe Eda Onar and Koray Gençoğlan, Biomaterials (lecture), Muğla Sıtkı Koçman University.

[6] D.Vojtech, J.Kubasek, J.Serak, P.Novak, Mechanical and corrosion properties of newly developed biodegradable Zn-based alloys for bone fixation, Acta Biomaterialia,7(9)(2011)3515-3522.

[7] F.Y.Zhou, B.L.Wang, et.al., Microstructure, corrosion behavior and cytotoxicity of Zr–Nb alloys for biomedical application, Materials Science and Engineering C 32(4) May (2012) 851–857.

[8] C.M.Cotrut, M.Tarcolea, M.D.Vranceanu, A.I. Gherghilescu, N.Ghiban, F.Baciu, I.C.Ionescu, Stainless Steel Brackets: In Vitro Corrosion Behaviour And Mechanical Debonding Test, Solid State Phenomena, 216 (2014) 187-193.

[9] Robert B.Heinmann, Structure, properties, and biomedical performance of osteoconductive bioceramic coatings, Surface & Coatings Technology 233 (2013) 27–38.

[11] H.F.Li, F.Y.Zhou, L.Li, Y.F.Zheng, Design and development of novel MRI compatible zirconium ruthenium alloys with ultralow magnetic susceptibility, NATURE, Scientific Reports 6, Article number: 24414 (2016).

[12] K.Mediaswanti *et al.*, A Review on Bioactive Porous Metallic Biomaterials, J Biomim Biomater Tissue Eng 18(1) (2013) 2-8.

[15] G.Ryan, A.Pandit, D.Panagiotis-Apatsidis, Fabrication methods of porous metals for use in orthopaedic applications, Biomaterials 27 (2006) 2651–2670.

[16] Montasser Dewidar, Influence of processing parameters and sintering atmosphere on the mechanical properties and microstructure of porous 316L stainless steel for possible hard-tissue applications, Int. Journal of Mech. & Mechatronics Eng. IJMME-IJENS, 12 (1) (2012) 10-24.

[17] Luana Marotta Reis de Vasconcellos et. al., Porous Titanium Scaffolds Produced by Powder Metallurgy for Biomedical Applications, Materials Research, 11 (3), (2008) 275-280.

[18] Jiunn-Der Liao, Han Lee and Chih-Kai Yao, Powder Metallurgy Based Porous Metal Biomaterials, J Powder Metall Min (2013), 2-4.

[19] Gang Chen, Peng Cao, Neil Edmonds, Porous NiTi alloys produced by press-and-sinter from Ni/Ti and Ni/TiH2 mixtures, Materials Science & Engineering A 582 (2013) 117–125.

[20] A.H.Yusop, A.A.Bakir, N.A.Shaharom, M.R.Abdul Kadir, and H.Hermawan, Porous BiodegradableMetals for Hard Tissue Scaffolds: A Review, International Journal of Biomaterials, Article ID 641430 (2012), 1-10.

[21] Zhu, S.L., Yang, X.J., Fu, D.H., Zhang, L.Y., Li, C.Y., Cui, Z.D., Stress–strain behavior of porous NiTi alloys prepared by powders sintering, Materials Science and Engineering A, 408 (2005) 264–268.

[23] G .I. Friedman Titanium powder metallurgy, Inter. J. Powder Metall., 6 (2) (1970) 43–54.

[24] Ma Qian, Cold Compaction and Sintering of Titanium and Its Alloys for Near-Net-Shape or Preform Fabrication, Int. Journal of Powder Metallurgy, 46 (5)(2010)29-44.

[25] I.M.Robertson, G.B.Schaffer, Review of densification of titanium based powder systems in press and sinter processing. Powder Metallurgy, 53 (2)(2010) 146-162.

[27] Miriam Kupková *et al.,* Corrosion Behaviour of Powder Metallurgy Biomaterials from Phosphated Carbonyl-Iron Powders , Int. J. Electrochem. Sci., 10 (2015) 671-681.

[29] H. Hermawan, D. Dube, D. Mantovani, Development of degradable Fe-35Mn alloy for biomedical application, Adv. Mater. Res. 15 (2007) 107–112.
[30] H. Hermawan, Conception, Développement et Validation d'Alliages Métalliques Biodégradables pour Emploi dans le Domaine de la Chirurgie Endovasculaire. PhD Thesis, Université Laval, Quebec, Canada, May 2009.
[31] R. Waksman et. al. Short-term effects of biocorrodible iron stents in porcine coronary arteries, J. Interv. Cardiol. 21 (2008) 15–20.
[32] B.Wegener *et. al*, Microstructure, cytotoxicity and corrosion of powder-metallurgical iron alloys for biodegradable bone replacement materials. Mater. Sci. Eng. B 176 (2011) 1789.
[33] Y.Torres, J.J.Pavon, I.Nieto, J.A.Rodriguez, Conven-tional Powder Metallurgy Process and Characterization of Porous Titanium for Biomedical Applications, Metallurgical and Materials Transactions B-Process Metallurgy and Materials Processing Science 42 (2011) 891-900.
[34] L. Bolzoni, E.M. Ruiz-Navas and E. Gordo, Processing of Elemental Titanium by Powder Metallurgy Techniques Materials Science Forum, 765 (2013) 383-387.
[35] Amigó, A; Zambrano, J; Martinez, S; Amigó, V., Microstructural Characterization of Ti-Nb-(Fe-Cr) Alloys Obtained by Powder Metallurgy, European Congress and Exhibition on Powder Metallurgy. European PM Conference Proceedings; Shrewsbury EPMA (2014), 20-25.
[38]E. Schüller, O.A.Hamed, M.Bram, D.Sebold, H.P. Buchkremer, D.Stöver, Hot Isostatic Pressing (HIP) of Elemental Powder Mixtures and Prealloyed Powder for NiTi Shape Memory Parts, Adv. Eng. Mater.5 (12) (2003) 918–924.
[39] Aris Widyo Nugroho, PhD Thesis. Investigation of the production and mechanical properties of porous Beta Titanium alloy compacts prepared by powder metallurgy processes for biomedical applications, April 2013.
[40] Y.F.Zheng, X.N.Gu, F.Witte, Biodegradable metals, Materials Science and Engineering R 77 (2014) 1–34.
[41] Y. P. Zhang, B.Yuan, M. Q. Zeng, C. Y.,Chung, X. P. Zhang, High porosity and large pore size shape memory alloys fabricated by using pore-forming agent (NH4HCO3) and capsule-free hot isostatic pressing, Journal of Materials Processing Technology, 192–193 ((2007) 439-442.
[42] E. D. Spoerke *et al*. Titanium with aligned, elongated pores for orthopedic tissue engineering applications, In: Journal of Biomedical Materials Research Part A, 84A (2) (2008) 402-412.
[43] Y. Zhao, M.Taya,Y.Kang, A. Kawasaki, Compression behavior of porous NiTi shape memory alloy, Acta Mater. 53 (2005) 337–343.
[44] A. Dudek, M. Klimas, Composites based on titanium alloy Ti-6Al-4V with an addition of inert ceramics and bioactive ceramics for medical applications fabricated by spark plasma sintering (SPS method), In: Materialwissenschaft Und Werkstofftechnik, 46 (3) (2015) 237-247.
[45] W. M. R. M. Daoush, et. al., Microstructural and Mechanical Characterization of Ti-12Mo-6Zr Biomaterials Fabricated by Spark Plasma Sintering, In: Metallurgical and Materials Transactions a-Physical Metallurgy and Materials Science, 46A (3), (2015) 1385-1393.
[46] M.Fousova, J.Capek, D.Vojtech, Preparation of magnesium-zinc alloy by mechanical alloying, Manufacturing Technology, 14 (3) (2014) 304-309.
[47] C.Y.Tang, L.N.Zhang, C.T.Wong, K.C.Chan, T.M.Yue , Fabrication and characteristics of porous NiTi shape memory alloy synthesized by microwave sintering, Mater.Sci.Eng. A528 (2011) 6006–6011.
[48] J.L. Xu et. al. Effect of pore sizes on the microstructure and properties of the biomedical porous NiTi alloys prepared by microwave sintering, Journal of Alloys and Compounds 645 (2015) 137–142.
[49] P. Novák, *et al.* Formation of Ni–Ti intermetallics during reactive sintering at 500–650 °C, Materials Chemistry and Physics, 155 (2015) 113-121.
[50] M. Whitney, S. F. Corbin, R. B. Gorbet, Investigation of the mechanisms of reactive sintering and combustion synthesis of NiTi using differential scanning calorimetry and microstructural analysis, Acta Materialia, 56(3) (2008). 559-570.
[51] B.Y.Li, L.J.Rong, Y.Y.Li, V.E.Gjunter, Synthesis of porous Ni–Ti shape-memory alloys by self-propagating high-temperature synthesis: reaction mechanism and anisotropy in pore structure ActaMater. 48 (2000) 3895–3904.
[53] D.T.Pham, S.S.Dimov, Rapid prototyping and rapid tooling--the key enablers for rapid manufacturing, Proc. Instn Mech. Engrs , 217 C: J. Mechanical Engineering Science, (2003) 1-23.
[54] L.A. Dobrzański, The concept of biologically active microporous engineering materials and composite biological-engineering materials for regenerative medicine and dentistry, Archives of Materials Science and Engineering, 80 (2) (2016) 64-85.
[55] ***, Overview of additive manufacturing and powder metallurgy processes, Powder metallurgy and additive manufacturing, The Linde Group, www.boconline.co.uk.
[56] Helena N Chia and Benjamin M Wu, Recent advances in 3D printing of biomaterials, Journal of Biological Engineering 9(4) (2015) 1-14.
[57] G. Chen, G. A. Wen, P. Cao, N. Edmonds and Y. M. Li, Processing and characterisation of porous NiTi alloy produced by metal injection moulding, Powder Inject. Mould. Int., 2012, 6, (3), 81–86.
[58] G. Chen, P.Cao, G.Wen, N.Edmonds,Y.Li, Using an agar-based binder to produce porous NiTi alloys by metal injection moulding, Intermetallics 37 (2013) 92–99.
[61] Randall M. German, Progress in Titanium Metal Powder Injection Molding, Materials 6 (2013), 3641-3662.
[62] D. Cristea, I. Ghiu□ă, D. Munteanu, Tantalum Based Materials for Implants and Prostheses Applications, Bulletin of the Transilvania University of Braşov, 8 (57) No. 2 Series I: Engineering Sciences (2015), 151-158 .
[63] C.Guerra, C.Aguilar *et al.* Production and characteri-zation of mechanical properties of Ti–Nb–Ta–Mn alloys foams for biomedical applications, Powder Metallurgy 57 (5) (2014) 1-5.
[64] C.O.Rusănescu, M.Rusănescu, T.Iordănescu, F.V.Anghelina, Mathematical relationships between alloying elements and technological deformability indexes, JOAM, 15(7-8) (2013) 718-723.
[65] I.Marek, P.Novák, *et. al.* Powder Metallurgy Preparation of Co-Based Alloys for Biomedical Applications, ACTA PHYSICA POLONICA A. 128 (4)(2015) 597-601.
[66] Muziwenhlanhla Arnold Masikane, MscThesis, A Investigation into the microstructure and tensile properties of unalloyed titanium and Ti-6Al-4V alloy produced by powder metallurgy, casting and layered manufacturing, University of the Witwatersrand, Johannesburg 2015.
[67] L. Reclaru, R.E. Unger, C.J. Kirkpatrick, C. Susz, P.Y. Eschler, M.H. Zuercher, I Antoniac, H Lüthy, Ni–Cr based dental alloys; Ni release, corrosion and biological evaluation, Materials Science and Engineering: C 32 (6),(2012) 1452-1460.

[68] V.K. Balla, S. Bose, N.M. Davis, A. Bandyapadhyay, Tantalum—A bioactive metal for implants, J. Miner. Met. Mater. Soc. 62 (7) (2005) 61.
[69]. B.R. Levine, S.Sporer, et al., Experimental and clinical performanceof porous tantalum in orthopaedic surgery, Biomaterials 27 (2006) 4671-4681.
[70] Xue-Nan GU, Yu-Feng ZHENG, A review on magnesium alloys as biodegradable materials, Front. Mater. Sci. China 4(2)(2010) 111–115.
[71] Zibo Tang, Jialin Niu, Hua Huang, Hua Zhang, Jia Pei, Jingmin Ou, Guangyin Yuan. "Potential biodegradable Zn-Cu binary alloys developed for cardiovascular implant applications", Journal of the Mechanical Behaviour of Biomedical Materials, 72(2017) 182-191.
[72] P. Thomsen, C. Larsson, L. E. Ericson, Structure of The Interface Between Rabbit Cortical Bone And Implants of Gold, Zirconium And Titanium Journal Of Materials Science: Materials In Medicine 8 (1997) 653— 665.
[73] Hussein M.A., C. Suryanarayana, M.K. Arumugam and N. Al-Aqeeli. "Effect of sintering parameters on microstructure, mechanical properties and electrochemical behavior of Nb–Zr alloy for biomedical applications, Materials & Design 83 (2015) 344–351.
[74] Alison Cowley and Brian Woodward, A Healthy Future: Platinum in Medical Applications, Platinum Metals Rev., 55, (2) (2011) 98–107.
[75] W. F. Agnew, T. G. H. Yuen, D. B. McCreery and L. A. Bullara, Histopathologic evaluation of prolonged intracortical electrical stimulation Exp. Neurol., 92, (1) (1986) 162 .
[76] M. Geetha, A. K. Singh, R. Asokamani and A. K. Gogia, Ti based biomaterials, the ultimate choice for orthopaedic implants –a review, Prog. Mater. Sci., 2009, 54, 397–425.
[77] M. Walter, Benefits of PM Processed Cobalt-Based Alloy for Orthopaedic Medical Implants, Carpenter Technology Corp., Wyomissing, PA, USA 2006.
[78]. Yang, H., Li, J., et al.: Structural preparation and biocompatibility evaluation of highly porous Tantalum scaffolds. In: Materials Letters 100 (2013), p. 152-155.
[79].Nan Li, Yufeng Zheng, Novel Magnesium Alloys Developed for Biomedical Application: A Review, J. Mater. Sci. Technol., 2013, 29(6), 489-502.
[80]. Pavel Salvetr, Pavel Novák, Dalibor Vojtìch, Porous Magnesium Alloys Prepared By Powder Metallurgy, MTAEC9, 50(6) (2016) 917-922.

Books:

[10] Manoj Gupta, Ganesh Kumar Meenashisundaram, Synthesis of Magnesium-Based Biomaterials (Chapter 2), Springer Briefs in Materials Insight into Designing Biocompatible Magnesium Alloys and Composites, pp 17-34, 2015.
[13] R. Goodall , Porous metals: foams and sponges (Chapter 10), Advances in Powder Metallurgy, Properties, processing and applications, Edited by Isaac Chang and Yuyuan Zhao, Woodhead Publishing Limited, pp. 273-307, 2013.
[14] Goodall, R., Andreas Mortensen, Porous Metals (Chapter 24), Physical Metallurgy, Vol. III, Edited by David E. Laughlin and Kazuhiro Hono , ISBN: 978-0-444-53770-6, Elsevier Publisher, pp. 2399–2595, 2014.
[22] M. Qian, G.B. Schaffer, C.J. Bettles, Sintering of titanium and its alloys(Chapter 13), Sintering of Advanced Materials, Woodhead Publishing Series in Metals and Surface Engineering, pp. 324-355, 2010.
[26] M J Donachie Jr., Titanium-A Technical Guide, 2nd ed., Materials Park, Ohio, ISBN: 978-0-87170-686-7, ASM International Publisher, pp. 46–53, 2000.
[28] Erhard Klar, Prasan K. Sama, Powder Metallurgy Stainless Steels: Processing, Microstructures, and Properties (Chapter 5), ASM International Publisher, ISBN: 978-0-87170-848-9, 2007.
[36] F.H. (Sam) Froes, Powder metallurgy of titanium alloys (Chapter 8), Advances in Powder Metallurgy, Properites, processing and applications, Edited by Isaac Chang and Yuyuan Zhao, Woodhead Publishing Limited, (2013) p. 202-240.
[37] Biomaterials Science-An Introduction to Materials in Medicine, Academic Press, ISBN 0-12-582460-2, 1996.
[52] M.Bram, T.Ebe and M.Wolff, A.P.Cysne, Applications of powder metallurgy in biomaterials (Chapter 18), Advances In Powder Metallurgy: Properties, Processing And Applications, Woodhead LTD Publisher, 520-554, 2013.
[59] R.M. German, Powder Injection Molding, Metal Powder Industries Federation, Princeton Publisher, 1990, ISBN 0918404959.
[60] I. Todd and A. T. Sidambe, Developments in metal injection moulding (MIM) (Chapter 6), Advances in Powder Metallurgy, Properties , processing and applications, Edited by Isaac Chang and Yuyuan Zhao, Woodhead Publishing Limited, pp. 109-146, 2013.

The Scientific Bulletin of VALAHIA University
MATERIALS and MECHANICS –Vol. 15, No. 13

DOI 10.1515/bsmm-2017-0016

USING 3D SCANNING TECHNIQUES IN ORTHOPEDIC SYSTEMS MODELING

Mihai-Constantin BALAȘA[1], Ştefan CUCULICI[2], Cosmin PANȚU[2], Simona MIHAI[3], Alexis-Daniel NEGREA[3], Mihai-Octavian ZDRAFCU[3], Dorin-Dacian LEȚ[3], Viviana FILIP[3], Ştefan CRISTEA[2]

[1]Macartney Hydraulics A/S, Denmark
[2]"Carol Davila" University of Medicine and Pharmacy Bucharest, România
[3]Valahia University of Targoviste, Institute of Multidisciplinary Research for Science and Technology, 13004, Targoviste, Romania

E-mail: mihai.simona@yahoo.com

Abstract. *Designing orthopedic implants with a long lifespan is essential for improving patients' quality of life. It is necessary to develop new products with a high degree of personalization for the human body. Physicians and engineers analyzed the geometry and behavior of healthy joints' motion under specific load conditions as well as the behavior over time and lifetime of orthopedic implants fitted to patients to improve their quality. The paper presents the way in which three-dimensional modeling techniques using specialized software (Catia, SolidWorks) can be combined with reverse engineering techniques (3D scanning) to optimize the design of orthopedic implants. The design of an implant consists of its three-dimensional modeling, as well as simulation of its integration into the human body, in order to analyze its behavior during motion. Therefore, it is necessary not only to 3D model the parts that make up the implant itself, but also to 3D model the bone to which the implant will be fitted. The paper highlights the complementarity of the classic modeling techniques with the reverse engineering techniques, which is necessary because the design of the parts that make up the implant itself can be achieved by specialized software modeling techniques, while the bones, having complex geometries, are better suited to 3D Modeling by scanning.*

Keywords: *Reverse engineering, bone, implant, CAD techniques, 3D scanning, orthopedic, modeling*

1. INTRODUCTION

Medical statistics have shown that orthopedic implants have a relatively short life span, so many researchers and physicians have joined efforts to optimize the design, to optimize the choice of materials and the manufacturing technology, in order to prolong implant durability. Theoretical research methods specific to engineers become more efficient when applied in close collaboration with medical professionals on a "functional team". The medical area of orthopedics has strong interference with the technical field, the field of medical engineering research having an interdisciplinary character.

The locomotor apparatus is the musculoskeletal system that allows you to move in space and mobilize different body segments, some in relationship to others.

The parts of the implant must allow specific relative movements for the entire range of human activities over a long period of time. The study starts from the anatomy concept of the knee joint ("a hinge joint"), the largest and most complex of the human joints. The bones that make up the knee joint (Figure 1) are: femur 1, patella 2, and tibia 3. The fibula 4 does not directly participate in the articulation.

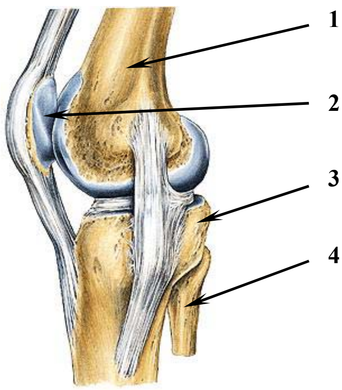

Figure 1. Knee Joint [1]
1-femur, 2-patella, 3-tibia, 4-fibula

The femur, the largest bone of the body, articulates with the tibia through its distal epiphysis formed by two protrusions (lateral and medial condyles) corresponding to the tibial plateau. The medial condyle is narrower but more prominent and is 3-4 mm longer than the lateral [1] to articulate with the medial tibial plateau.

The tibia on which the femur rests shows a top plateau with two condyles, separated from each other by a spine.

The medial and tibial plateaus are not in the same plane, the medial one being lower by 3-4 mm.

Anterior to the two main bones of the joint (femur and tibia), there is the extensor apparatus that includes a patella which via the patellar ligament is attached to the tibia.

For the assessment of human body bones and their pathology, their geometry must be related to the planes and axes of the human body, Figure 2 [1, 2, 3].

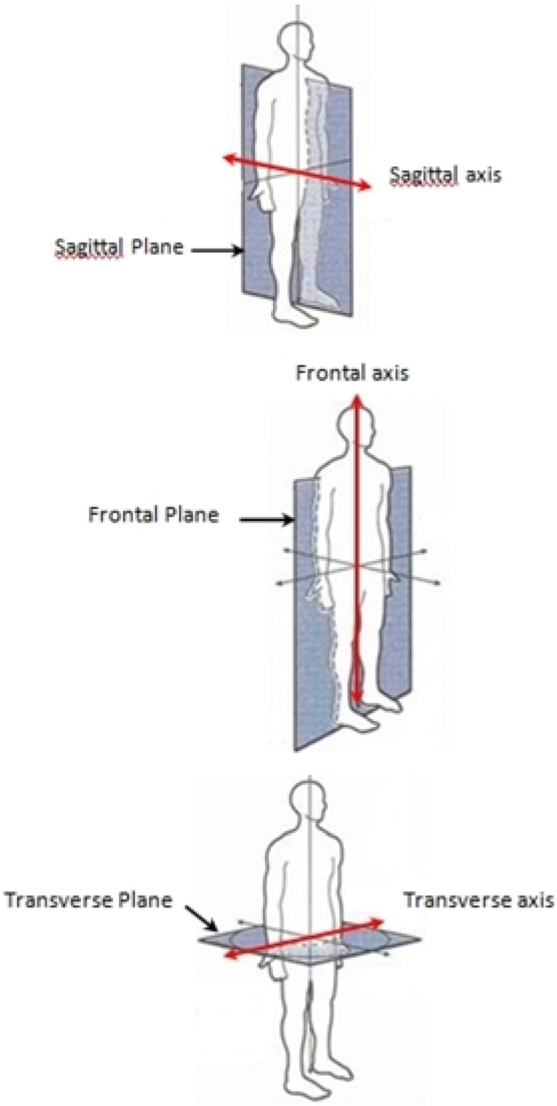

Figure 2. Axes and planes of the human body [1]

Being based on the principle of bilateral symmetry, the human body has three axes and three planes forming a triorthogonal triangle. The planes of the human body can be applied to the area of the body we are studying (for example, the knee joint) and named the same. A very important aspect is the mechanical and anatomical axes of the bones forming the lower limb (Figure 3).

Although apparently the human limbs seem to be straight, there is a 9-degree angle between the vertical axis and the anatomical axis of the femur and an approximate 175 degree angle between the anatomical axis of the femur and the one of the tibia [1].

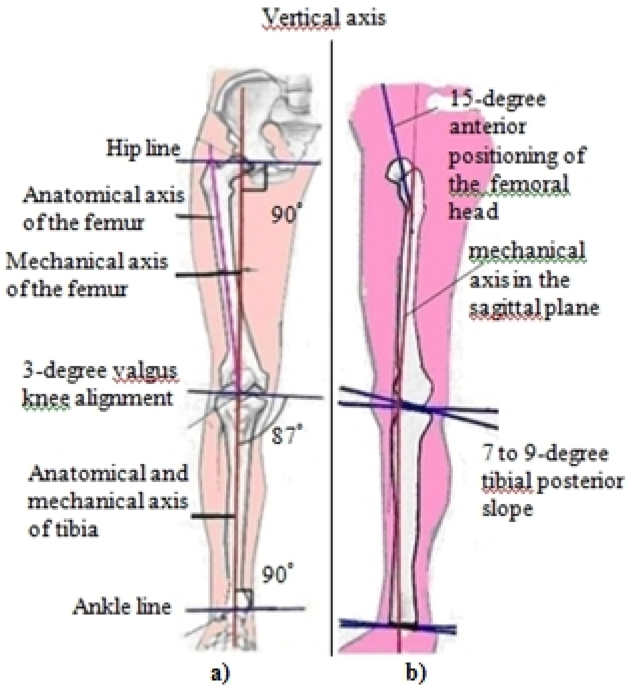

Figure 3. Lower limb axes [1]
a) in frontal plane, b) in sagital plane

The mechanical axis of the lower limb is defined as an axis going through the center of the hip, knee and ankle joints, which forms a 3-degree angle with the vertical axis, Figure 3. The anatomical axis of the tibia coincides with the mechanical axis, while the femur axis does not; it forms a physiological angle of 5-10° to the mechanical axis. You can also highlight the hip, knee and ankle guidance lines.

A joint means the connection between two bones, and their relative movement. The joint makes the mechanical link between the bone levers.

The shape and degrees of freedom of movement of the joints are important factors that determine the direction of the movements and limit their amplitude.

Understanding anatomy and knee biomechanics [4] is extremely useful both for the study of locomotion in general and for the diagnosis and treatment of pathological conditions.

Knee movements are allowed by the shape of the tibial and femoral joint surfaces and are limited by the 4 major ligaments (ACL - anterior cruciate ligament, PCL – posterior cruciate ligament, MCL - medial collateral ligament, LCL - lateral collateral ligament).

The knee joint is basically formed of two friction couplings (two femoral condyles in contact with two tibial plateau parts) acting unitarily due to the ligaments, especially the cruciates.

The knee joint has 6 degrees of freedom: 3 rotation (flexion / extension, internal / external, varus / valgus) and 3 translation (anterior / posterior, medial / lateral, superior / inferior), Figure 4.

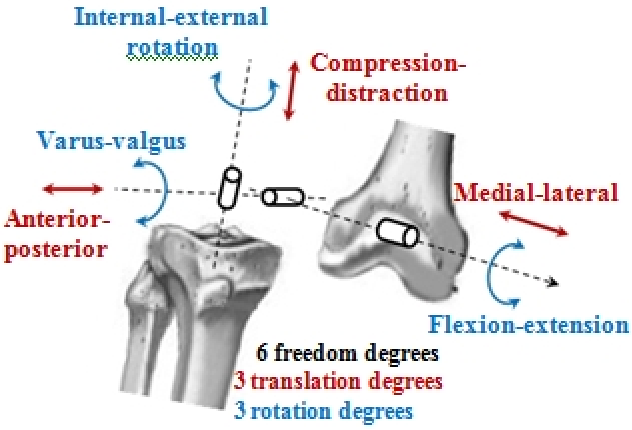

Figure 4. Knee cinematics [1]

The main movement is flexion / extension. It is accomplished by a rolling and sliding motion of the femoral condyles on the tibia, followed by a movement of the axial passage of the tibia, given the inequality between the two femoral condyles.

Knee arthroplasty is the surgical procedure in which the affected knee and cartilage are removed and replaced by an implant consisting of the following parts: femoral component 1, polyethylene 2 insert and tibial component 3, Figure 5.

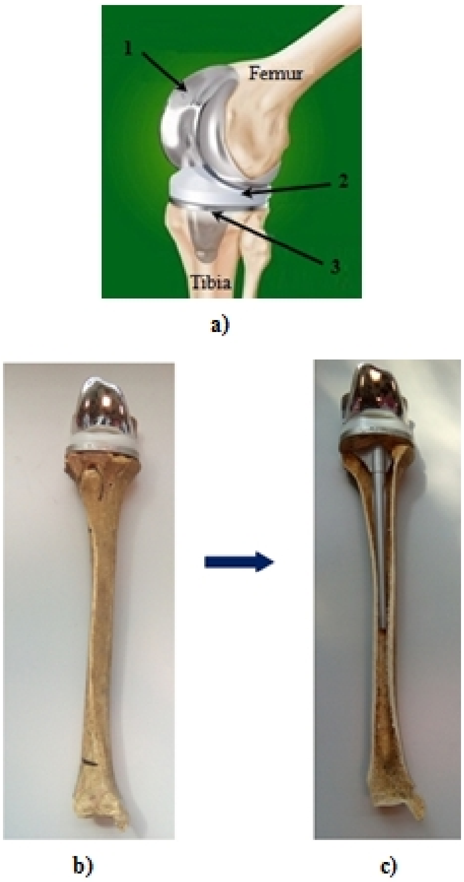

Figure 5. Knee prosthesis [5]
a) Virtual model, b) Tibia (real bone) with implant, c) Cross section through tibia, with implant

These pieces allow for natural knee movements.

From the mechanical point of view, the main causes of failure that arise from the knee joint replacement operation are [6]: the polyethylene wear from which the insert 2 is made, the failure of the femoral component cement 1 and the tibial component 3 or even the implant breakage [7, 8] . In order to minimize these issues, the virtual model of the parts that make up the implant and the virtual model of the bones in which it is mounted are made and the virtual bone-implant assembly is analyzed, both cinematically and in terms of mechanical resistance (Finite element analysis). By simulating the mechanical behavior of the implant in the human body, information is obtained from which the physician can make a correct choice of the type and size of the parts that make up the implant (eg the type and length of the tibial extension).

2. THREE-DIMENSIONAL MODELING OF HUMAN BONES THROUGH 3D SCANNING (REVERSE ENGINEERING)

Because human body bones are geometrically quite complex, we used Reverse Engineering techniques to get their virtual model.

Reverse engineering can be used in the design and redesign process and consists of taking geometric shapes of existing objects using special devices such as 3D scanners and converting them into digital formats [9]. In other words, reverse engineering consists of obtaining the virtual model of an existing object through 3D scanning techniques.

The paper presents the virtual model of the tibia starting from the real bone, Figure. 6. The bones were made available to us by the "Carol Davila" University of Medicine and Pharmacy in Bucharest - the Anatomy Laboratory.

Figure 6. Tibia, real bone different sizes

The scanner used to digitize the tibia is a portable scanner of the 3D Exascan type, Figure 7. It scans objects of different sizes, with simple or complex geometries, with a scanning resolution of 0.2mm, making 25.000,00 measurements / s.

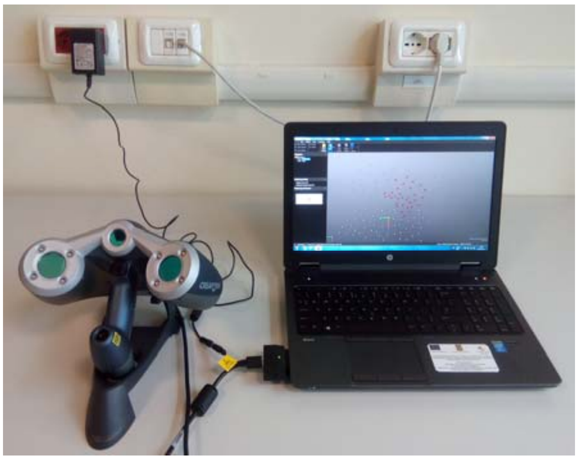

Figure 7. Portable 3D Exascan Scanner

The stages of the scanning process are:

- connecting the scanner and accessing the "VXelements"

- calibrating the scanner, if necessary

- preparation of the benchmark for scanning, i.e. setting reference targets; The scanner uses the reference targets to position itself in space and set the scan direction

- target scanning

- scanning the object

For a good scan of the object, the scanning distance must be respected.

Targeting can be done in two ways:

The first option - when the targets are positioned on the scanned object. In this case, the object can be moved in any position during scanning.

The second option - when the targets are not positioned on the scanned object, but are positioned on the work table, and the object is fixed between the targets. In this case, the object can only be moved after the scan is completed.

To scan the tibia, we tried several scanning variants to find the optimal version.

We tried scanning with targets placed on the tibia, but the shape of the bone did not allow the mounting of at least four targets on all the surfaces of the bone.

Scanning the tibia with the worktop mounted targets also did not allow full scanning because we chose to fix the scanned tibia in the vertical position (to get the mark from a single scan) and the optimal scanning distance relative to the targets did not allow to scan the entire part, Figure 8.

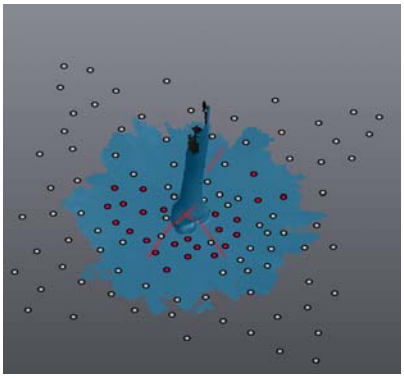

Figure 8. Scanning with targets mounted on the worktop

We tried to add targets to a vertical plane, namely to mount a target panel behind the bone, but this method was not satisfactory as the scan result had overlapping surfaces and voids Figure 9.

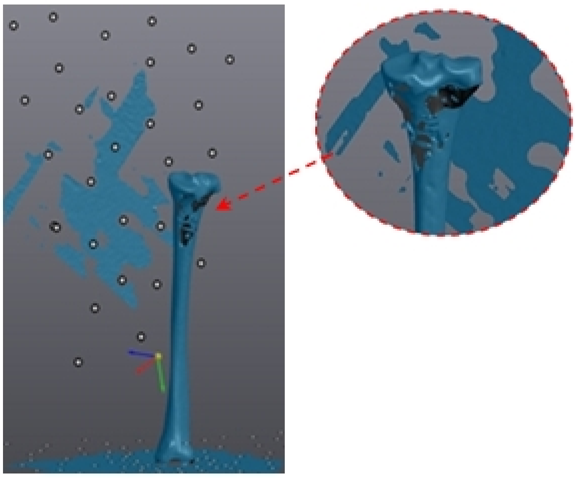

Figure 9. Scanning with targets mounted both on the worktop and in a vertical plane

We tried another option, namely setting the targets only on the worktop, fixing the tibia in a vertical position and mounting the targets on top of the tibia, Figure 10.

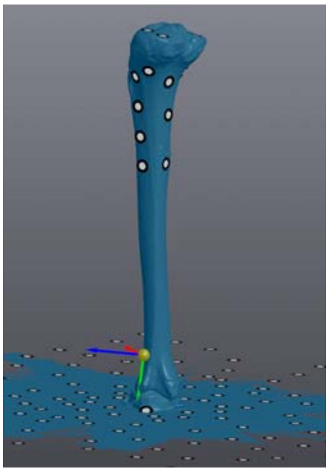

Figure 10. Scanning with targets mounted on the worktop and on the top of the tibia

Figure 11 shows the tibia in the optimal scanning model. During the scanning process, the surface is rendered in real-time and the user can view the result as the object is scanned.

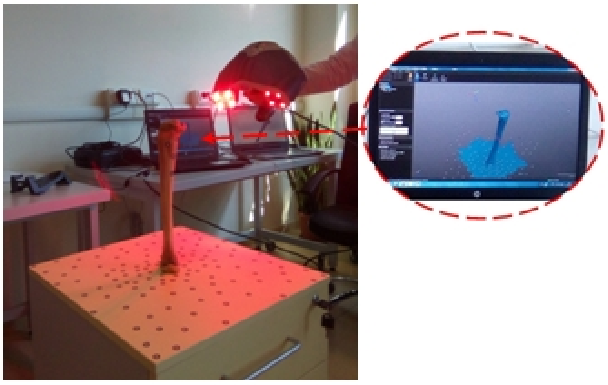

Figure 11. Optimal scanning model

By using this method, we have achieved a result with a very good fidelity. After 3D scanning, the virtual model obtained may have imperfections (holes, discontinuous surfaces). In this case, it is imported into a three-dimensional modeling software (Catia, SolidWorks) and retouched. A good scan of the object, with a high degree of fidelity, shortens the processing time.

The quality of the scan pattern is also influenced by the resolution we set in the scanner software before or after the scan. Thus, the scanner software can achieve a mesh from previously acquired, coarser or finer raw data, depending on the user-defined scanning resolution. Mesh is required for export to the software that will process the pattern obtained via scanning.

After scanning, we imported the saved Mesh model into Catia and processed it: we delimited the areas, checked and completed the surfaces, eliminating the discontinuities, Figure 12.

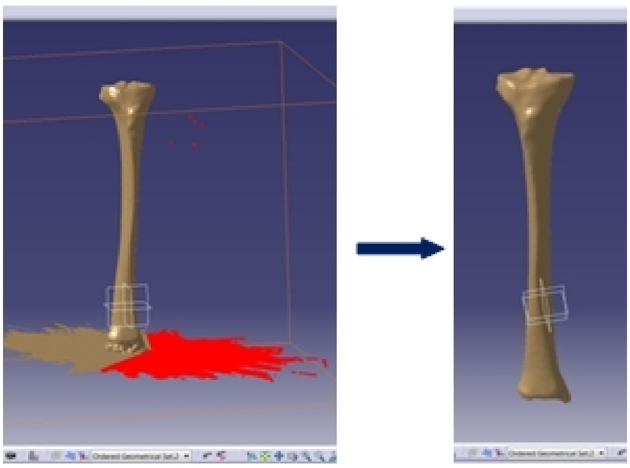

Figure 12. Scanned tibia, processed in CATIA

3. THREE-DIMENSIONAL MODELING OF KNEE IMPLANT PARTS BY CONVENTIONAL TECHNIQUES

Since the knee implant parts have relatively simple shapes, we can use conventional modeling techniques with specialized software such as Catia, SolidWorks to get their virtual model. Thus, we modeled the knee prosthesis parts using the SolidWorks software, Figure 13. These parts are: the femoral component 1, the polyethylene insert 2 and the tibial component 3. To give better stability to the bone-implant assembly, the tibial component 1 extended with a stem (tibial extension) 4.

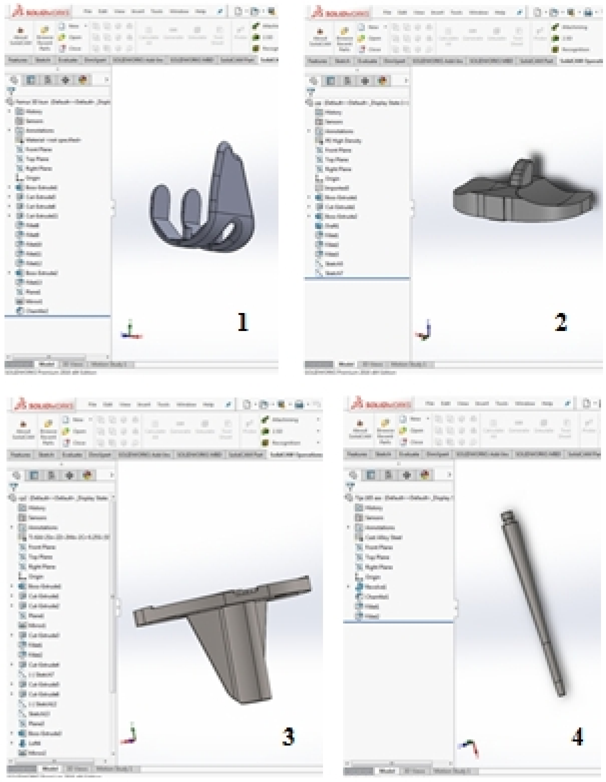

Figure 13. SolidWorks model of the knee prosthesis components: 1- femoral component, 2 - polythene insert, 3 - tibial component, 4 - stem (tibial extension)

After modeling these parts, we assembled them into SolidWorks, obtaining the virtual model of the bone plus prosthesis. We have thus tested the accuracy of the execution of the implant parts and verified that the prosthesis ensures the degrees of freedom specific to the knee joint (Figure 14). In this way, we tested the mobility of knee joint because it is an esential goal taken into consideration in a knee artroplasty [10]. We simulated the movement of the femoral component 1 with respect to the assembly consisting of the polyethylene insert 2, the tibial component 3 and the tibial extension 4. In order to achieve the bone implant assembly, we saved the tibia processed in Catia with the extension .igs, we imported it into SolidWorks and then added the implant components.

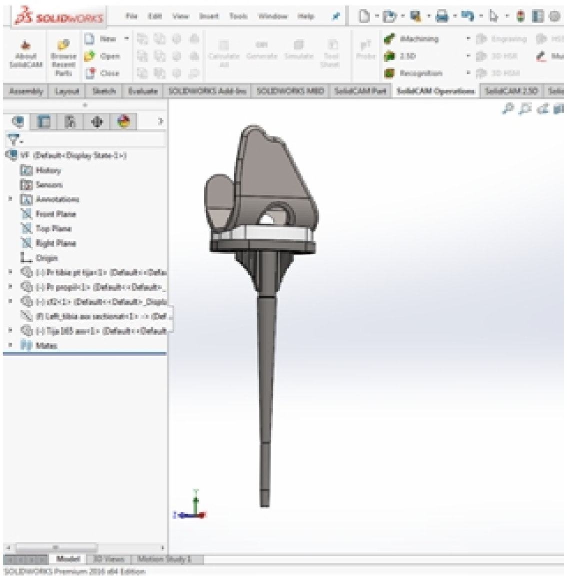

Figure 14. The knee implant assembly, modeled in SolidWorks

Next, we made a cross section of the tibia and removed the plateau.

Inside the tibia we made a longitudinal groove, representing the medullary canal into which the implant is inserted, Figure 15.

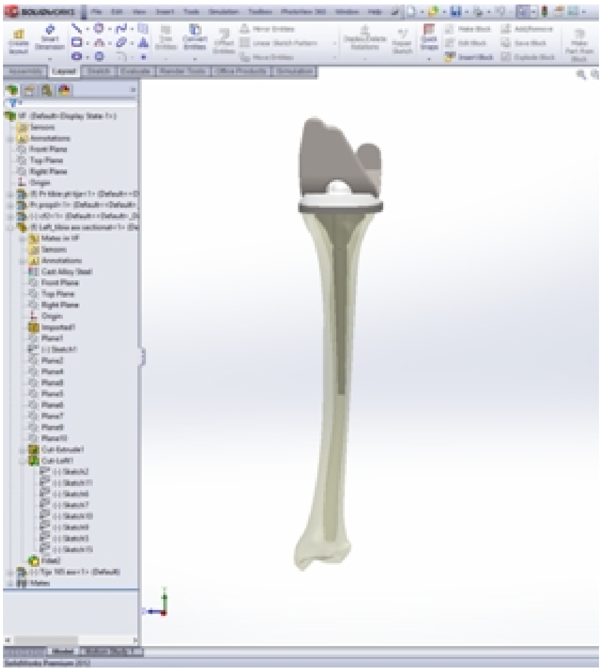

Figure 15. Bone – implant assembly

4. FUTURE RESEARCH GOALS

In order to simulate the implant behavior in the human body, the following steps will be taken in the future:

Assign material and set material properties for all components: tibia (bone), femoral component (CoCr alloy), polyethylene insert (polyethylene UHMWPE), tibial component (CoCr alloy), stem (CoCr alloy).

The weight of the human body is amplified with an error coefficient simulating the natural functioning of the knee. Finite element analysis is performed to measure the stresses and deformations occurring in the components of the assembly and to check the mechanical strength of the implant. Repeat the analysis for different tibia lengths for different varus-valgus tilt angles for different degrees of osteoporosis (bone densities). For each situation, determine the optimal type and size (length, diameter) of the tibial extension.

5. CONCLUSIONS

Creating virtual bone models through 3D scanning meets designer requirements, as the virtual model resulting from scanning reproduces with high fidelity the real bone.

The disadvantage of modeling by scanning the bones is that the method cannot be applied in vivo. But even if it is applied only in vitro, the results of the study conducted with these models can be applied to patients.

Another method of realizing the virtual model of human bones is reconstruction by transforming radiographic images (in vivo method). The difference between the two methods is that the latter does not require the existence of the real bone (from the corpses), but it is a more cumbersome method.

3D scanning techniques can be used in complementarity with conventional virtual modeling techniques with specialized software and can be successfully applied in biomechanics, where we frequently encounter objects with complex surfaces.

REFERENCES

[1] I. I. Cofaru, Summary of the PhD thesis, Researches regarding the biomechanics of the axial deviations of the human lower member and the development of the correspondent surgical devices http://doctorate.ulbsibiu.ro/obj/documents/rezumatenglcofaruioana.pdf

[2] S. Pickering, D. Armstrong, Alignment in total knee replacement (TKA), 2012, British Editorial Society of Bone and Joint Surgery, The Journal of Bone & Joint Surgery http://www.boneandjoint.org.uk/sites/default/files/Focus%20on%20Alignment%20in%20TKR.pdf

[3] R.W. Brouwer, T.S. Jakma, S.M. Bierma-Zeinstra, A.Z. Ginai, J.A. Verhaar, The whole leg radiograph: standing versus supine for determining axial alignment, Acta Orthopaedica Scandinavica 2003; 74 (5): 565–568, http://www.tandfonline.com/doi/pdf/10.1080/00016470310017965

[4] A.Williams, M. Logan, Understanding Tibio-Femoral motion, The Knee, Volume 11 (2004) pp. 81–88, http://www.sciencedirect.com/science/article/pii/S0968016004000043

[5] http://www.doctorortoped.ro/

[6] S. Mihai, V. Filip, New design concept for reducing torque wear on implant, Applied Mechanics and Materials, Vol. 658 (2014) pp. 453-458 https://www.scientific.net/AMM.658.453

[7] F. F. Cintra, A. K. Yepéz, M. G. S. Rasga, M. Abagge, P. G. C. Alencar, Tibial component in revision of total knee arthroplasty: Compararison between cement and hybrid fixation, Sociedade Brasileira de Ortopedia e Traumatologia, 2011, V46(5), pp. 585-590 http://ac.els-cdn.com/S225549711530416X/1-s2.0-S225549711530416X-main.pdf?_tid=cd61da7c-67bf-11e7-b298-00000aab0f6c&acdnat=1499946094_78f02ba083912d6adf3037f5389b2a77

[8] A. Mittal, P.B. Bhosale, A.V. Suryawanshi and S. Purohit, One – stage long-stem total knee arthroplasty for arthritic knees with stress fractures, Journal of Orthopaedic Surgery 2013; Vol. 21 No. 2, pp.199-203 https://pdfs.semanticscholar.org/30e2/6aa48d15366ee82f7bfcc9227a27f7cee9ff.pdf

[9] T. Tóth, J. Živčák, A Comparison of the Outputs of 3D Scanners, Procedia Engineering, Volume 69, 2014, pp. 393-401 http://ac.els-cdn.com/S1877705814002501/1-s2.0-S1877705814002501-main.pdf?_tid=17d22052-67c1-11e7-9f4e-00000aab0f01&acdnat=1499946648_3bce7ec962bf878f67fd664802849386

[10] Șt. Cristea, A. Prundeanu, Fl. Groseanu and D. Gârtone, The Role of Arthroscopy in Mini-Invasive Treatment of Tibial Plateau Fractures, Chapter from the book Modern Arthroscopy, pp. 225-236, http://www.intechopen.com/books/modern-arthroscopy

DE GRUYTER OPEN

The Scientific Bulletin of VALAHIA University
MATERIALS and MECHANICS –Vol. 15, No. 13

DOI 10.1515/bsmm-2017-0017

METHODS OF DETERMINING SOCK VALUES AND THE DISTANCE BETWEEN AXES OF THE GEARBOXTEETHING USING A FITTED TOOTH ENGAGEMENT

Dănuț STANCIU, Gheorghe Ion GHEORGHE

National Institute for Research Development in Mechatronics and Measurement Technique, Bucharest
6-8 Pantelimon Road, District 2, Bucharest, Romania

E-mail: danutstanciu@yahoo.com

Abstract: *There are several constructive variants of devices built for complex control of engagement on both sides aimed at controlling both internal and external shocks, all of which featuring a standard wheel compound. By the method of forced tooth engagement fitted between the standard wheel and the measuring wheel and using the spectral analysis, constructive errors of the gear wheels can be quickly determined, especially those consisting in shocks and the variation of the distance between the axes, errors that severely impact on operation. At the National Institute of Research and Development in Mechatronics and Measurement Technique was developed a device used to control shock values and the distance between the axis of the gearboxes (for four of the gearbox speeds) by means of forced engagement and complex harmonic analysis.*

Keywords: *engagement, engagement shock, distance between the axels, harmonic analysis.*

1. INTRODUCTION

A classic method for gear control is based on measuring the variation of the distance between axes based on the method of margin less engagement on both sides between the gear wheel and the standard wheel [1-3]. In order to obtain a modern and accurate means of measuring we must resort to electronic computer processing, using complex mathematical processing algorithms [4], a method which also has the advantage of using a much-simplified mechanics [5].

2. COMPLEX CONTROL ON BOTH SIDES

Control based on a standard wheel which is engaged on both sides is considered a complex control because it allows to determine a composite error as a result of the individual wheel errors in the gearing. The principle of measurement and the schematic diagram of the device are depicted in Figure 1 below [5].

Devices built for complex engagement control on both sides are made in several constructive variants, controlling both inner and outer dents, all of which including the standard wheel as an essential feature.

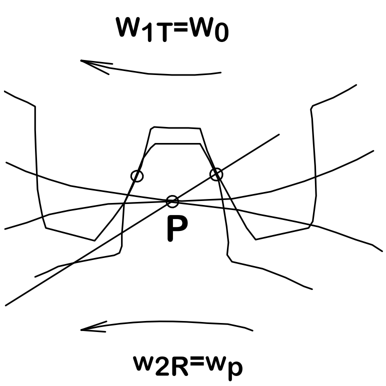

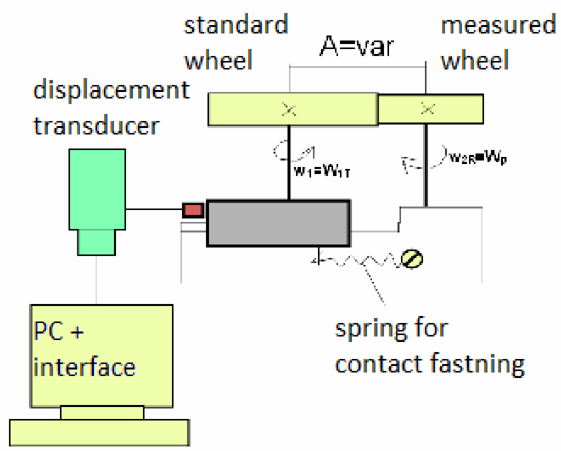

a) b)

Figure 1. a –Engagement diagram, b – Schematic diagram of the control device

By controlling the toothed wheel by means of a standard wheel, the composed error is determined as the result of individual errors. This composed error (according to STAS 6273-81) represents the variation of the measured distance between the axle F''_{ir} that is defined as the difference between the maximum and the minimum value of the distance that needs to be measured between the axis of the standard wheel and the axis of the working wheel that needs to be checked in a margin less engagement at a complete rotation of the test wheel. If the working wheel rotates with one tooth, this difference is called "the variation of the distance measured between the axes when rotating with one tooth: F''_{ir}

Determining the contribution of each individual error or individual deviation of the working wheel in the diagram of the variance of the measured distance between the F''_{ir} axes is difficult to make and it is interpretable, which leads to the elaboration of a series of hardly verifiable, sometimes contradictory theories. The most important contribution is that of radial shock b_r.

We must note that a conjugated gear wheel can also be used in the absence of the standard gear wheel, should the margin less engagement not make the contact between the tooth of the gear and the end of the other gear. The method is used as a gear sorting method, mating together two conjugated wheels, for which the variation of the distance between the axes has the smallest of values. When performing the control process, by means of several consecutive teeth positions of the two wheels we can also determine the pair of conjugated teeth for which the minimum error is obtained.

The radial shock, the most important feature, can also be established on the diagram recorded when engaging the gear wheel with a standard wheel. Such a diagram will be similar with the on in the following figure [10]:

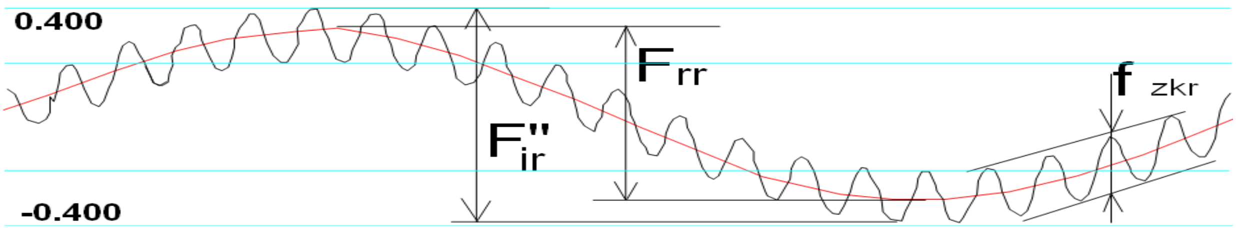

Figure 2. Total error diagram [10]

The elements below appear on the diagram:

- $F''_{ir.}$ - variation of the measuring distance between the axes (radial composite error)
- F_{zkr}- cyclic error;
- F_{rr}. - radial shock (see Figure 1).

It is found that the radial shock has a sinusoidal variation over which the cyclic error of each tooth overlaps.

Since the largest component of the radial shock is the eccentricity "e" it can be noted that:

$$2e \approx F''_{ir} - f_{zkr} \qquad (1)$$

The problem that arises is the determination of the error values due to the shock to the teeth of the tested wheel. In Figure 2, a tooth displays such an error - shown more clearly in Figure 3.

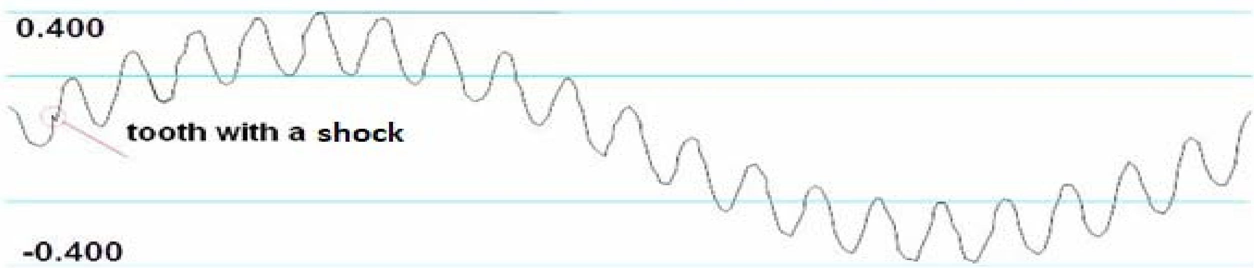

Figure 3. Positioning of the defect within the total diagram

A shock is defined as a sudden variation in the distance between the axis of the gears in dynamic drive (rotated at a certain speed). By denoting with A the distance between the axis of the engaged gears, then a shock is given by the velocity of the variation of the distance, respectively the first derived in relation to time as in the formula below:

$$V_{shock} = \frac{dA}{dt} \qquad (2)$$

where:

V_{shock} – measured/calculated value of shock
A – value of the distance between the axes
t – time in which displacement A takes place

These characteristics of the shock that needs to be determined lead us to the following methods of obtaining the measured value:

1. Determining the rate of variation of the distance between the axes
2. Using the analysis be decomposing the recorded chart in Fourier series.

3. METHODS OF DETERMINING THE VALUES OF SHOCK

3.1. Determining the Rate of Variation

Collected data is acquired at equal time intervals and stored in a datasheet. In order to obtain the rate of variation, the numerical derivative is applied to this datasheet, and the value obtained is compared with a baseline value. Thus, the formula for calculating the rate of variation of the distance between axes is given by the formula below:

$$V_i = \frac{\Delta a}{\Delta t} = \frac{a_i - a_{i-1}}{\Delta t} \quad (3)$$

where:
V_i – speed calculated in location *i*
a_i, a_{i-1} – value of displacement in location *i*,and in *i-1*
This method is mainly used for manually operated shock control devices (working under human supervision) where the value of the distance between axes is monitored by the operator by means of a comparator.
In the case of data acquired by an automated system, the acquisition speed is much higher, which requires that the shock be sampled at several points, so that the rate of variation is not given by the start and end limits of the shock but by the intermediate values, as in the figure 4.
In the figure above, we can see that the shock (for curve a) is acquired with points 1-5, and the speed for each point is: *V1-V2*, *V2-V3* etc.; by applying the same method for curve *b*, we will have the same rate of variation, which will point to a shock, which is inaccurate.

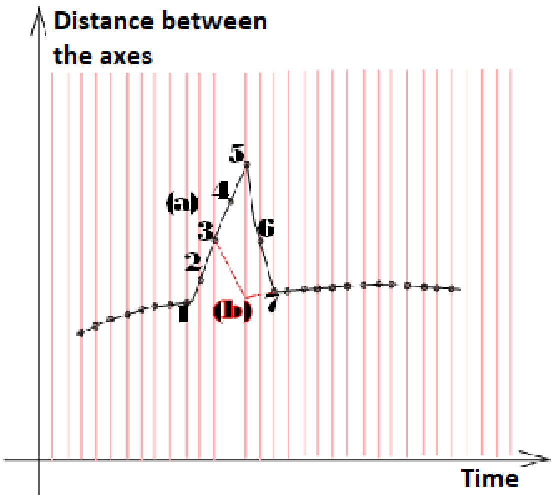

Figure 4. Diagram of anthrax for a shock to a tooth

3.2. Using Analysis Based on Fourier Series Decomposing

Fourier series decomposing transforms a periodic function into a sum of sinusoidal functions; a periodic function is a function of the following type:

f (t) = f (t+T), where *T* is the period of repetition of the function [11-14].
A Fourier series is a sum of an infinite number of sinusoidal (sinus and cosine) functions - each with a frequency equal to a multiple of an integer of 1 / T, as in the following formula [13, 14]:

$$g(t) = a_0 + \sum_{m=1}^{\infty} a_m \cos\left(\frac{2\pi mt}{T}\right) + \sum_{n=1}^{\infty} b_n \sin\left(\frac{2\pi mt}{T}\right) \quad (4)$$

where constants $\boldsymbol{a_m}$, $\boldsymbol{b_n}$ correspond to the coefficients of the Fourier series determining the weight of each sinusoid.
Prior to the emergence of modern computational methods, the determination of Fourier series coefficients was complicated, so this method had little use, but with the advent of electronic computers, methods of calculating these coefficients have been developed that

allow them to be determined quickly or even in time real. Therefore, a decomposing processing based on Fourier Series will respect the sequence presented in the diagram presented on the following page:

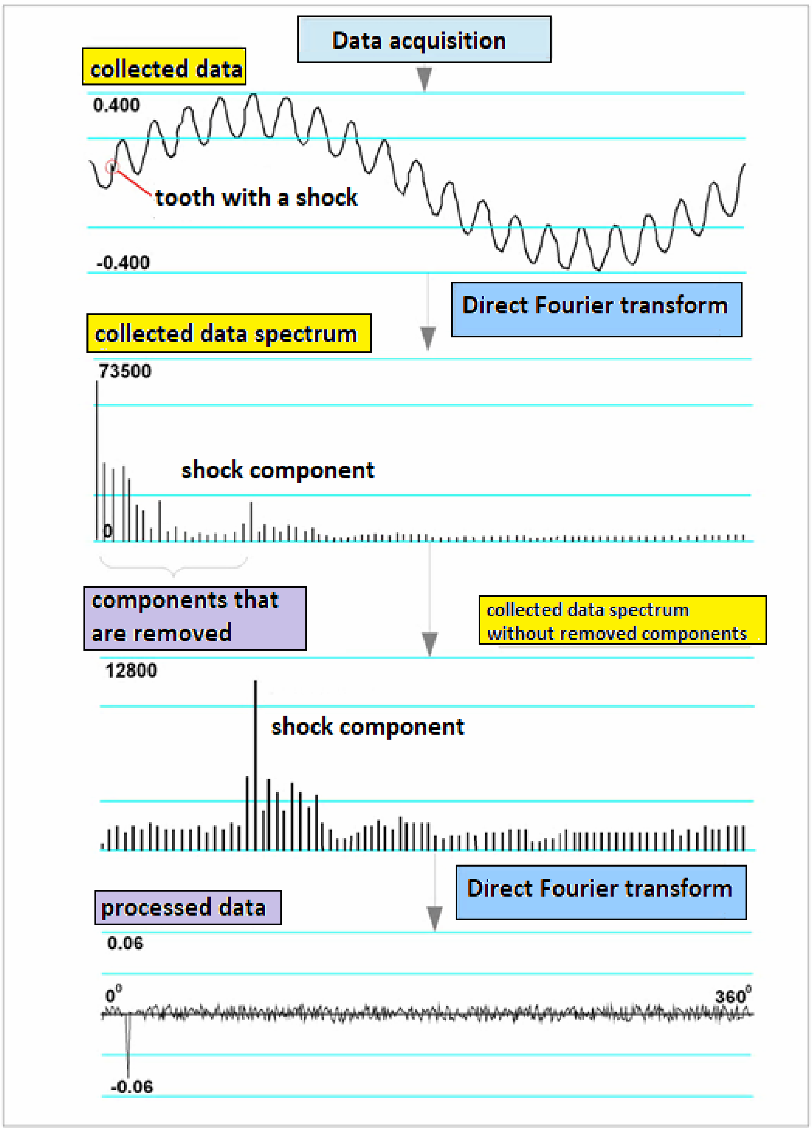

Figure 5. Processing diagram

Furthermore, the determination of the most significant shock with is obtained by selecting the maximum value in terms of an absolute value out of the processed value (i.e. 0.050, in the presented case study).

4. DESCRIPTION OF THE EQUIPMENT DEVELOPED FOR "DACIA RENAULT PITEŞTI"

The installation consists of a control table on which a support for securing the primary shaft is located between a rotating tip with rollers and a precision bush provided with grooves and 4 sledges sliding on roller guides with pneumatic buffers on which the gears that need to be tested are mounted for detecting shocks (tooth defects caused mainly by faulty handling of work pieces between workstations), and anthrax. The toothed shaft and the gears that need to be tested engaged with it are rotated by an alternative current motor reducer with a reducer and a speed variator with a speed of approximately 30-40 rpm, while the "shocks", as well as the teeth defects and the anthrax variation are highlighted by the sliding of the sledges with guides and read with incremental linear motion transducers with a race of at least 6 mm (plus the radius variance measured by the pneumatic buffers), on the display panel of the SIEMENS industrial computer.

The measurement of anthrax during the engagement on two sides also allows, in addition to checking the operation of the gear within normal parameters, to detect the occurrence of the manning operation on the sides. Thus, if a normal addition of 0.05-0.06 mm of manning is considered, from simple trigonometric calculations results, in the case of unmanned wheels, a shift in the sinusoid of the variation of anthrax of 0.15-0.2 mm that

is easily sensed by measuring instruments.
Each measuring section also contains a pair of inductive transducers that allow for the elimination of the radial shock of the spindles relative to the axis of rotation of the primary shaft that is hinged between the tips.
Periodically, the device is calibrated with cylindrical standard discs to determine the correct running anthrax. The device is protected by LED safety barriers.

Figure 6. Shock measuring device

5. CONCLUSIONS

The concept and making of the "Intelligent mechatronic equipment for shock and anthrax control of free gears 1,2,3,4 and primary shaft" belong to the National Institute of Research and Development in Mechatronics and Measurement Technique, Bucharest-Romania.

The implementation of the mechatronic equipment at S.C. Automobile DACIA Groupe Renault S.A. Pitești - Renault Mecanique Roumanie has led to the following results:
- Increasing the degree of automation and computerization of the process of controlling the toothed wheels of automotive gearboxes in the production line;
- Increasing labour productivity in control operations that are run in the manufacturing flow;
- Ensuring work safety in the process of production and control in compliance with the European norms in the field;
- Ensuring a high level of quality in the manufacturing of toothed parts in automotive gearboxes.

REFERENCES

[1] Alexandru P. et al., Proiectarea funcțională a mecanismelor, Editura Lux Libris, Braşov, 2000.

[2] Botez E., Minciu C., Mecanismul fictiv şi precizia dinamică a lanțului cinematic de rulare, Ed.Tehnica, Bucharest,1984.

[3] Draghici I. et.al, Îndrumar de proiectare in constructia de masini, Vol II, Editura Tehnica. Bucharest, 1982.

[4] Bracewell R. N., The Fourier Transform and Its Applications (2nd Edition, Revised), MacGraw-Hill, 1986.

[5] Minciu Constantin, Precizia și controlul angrenajelor, Editura Tehnică, Bucharest, 1984.

[6] Duca Z., Teoria sculelor aşchietoare, Editura Tehnică, Bucharest, 1982

[7] Lighthill, M. J. – An Introduction to Fourier Analysis and Generalized Functions, Cambridge University Press, 1978.

[8] Mott R., Machine Elements in Mechanical Design, 4th Edition, Prentice Hall, 2004.

[9] Pavelescu D. et al., Organe de masini. Editura Didactica si Pedagogica, Bucharest, 1985.

[10] Sauer et al., Angrenaje, Volumes 1 & 2, EdituraTehnică, Bucharest, 1970.

[11] Catangiu A., Ungureanu D. N., Despa V., Data Scattering in Strength Measurement of Steels and Glass/Epoxy Composite, The Scientific Bulletin of Valahia University-Materials and Mechanics, Vol.15, No.1/2017.

[12] Introduction to the Fourier transform - web page - http://www.thefouriertransform.com/#introduction

[13] Fourier Transforms - web page - http://www.cv.nrao.edu/course/astr534/FourierTransforms.html

[14] Fourier Transform - web page - https://en.wikipedia.org/wiki/Fourier_transform

DE GRUYTER OPEN

The Scientific Bulletin of VALAHIA University
MATERIALS and MECHANICS –Vol. 15, No. 13

DOI 10.1515/bsmm-2017-0018

NEW MEASUREMENTS RESULTS ACHIEVE FOR PROACTIVE MAINTENACE WITH VIBRO-EXPERT DIAGNOSIS SYSTEM

Ionel RUSA[1] , Cornel MARIN[1]. Marius BAIDOC[2]

[1]VALAHIA University of Târgovişte, FIMM, Str. ALEEA SINAIA Nr.13 Targoviste [2]S.C. VIBRO SYSTEM S.R.L.

Email: [1]ionelrusa@gmail.com, [1]marin_cor@yahoo.com, [2]info@vibrosystem.ro

Abstract. *One important objectives of proactive maintenance are the knowledge of the technical state of machinery, the intelligent planning of interventions according to the diagnosis technique, identification and correction of assembling errors. The aim of this paper is to present a new case on the vibrations diagnosis of hydro-aggregate CAMPELA - CHE Dubasari (MOLDOVA). The VIBRO EXPERT diagnostic system used on the CAPMELA hydro-aggregate is designed to measure, monitor, diagnose, and analyze the technical and functional parameters in order to safe use of the hydro-aggregate turbine, using the vibrations data measurement. The proactive maintenance concept is being used more and more thanks to the development of these intelligent monitoring and control systems, in order to prevent interruptions due to major failures.*

Keywords: *proactive maintenance, vibration measurement data, diagnosis system Vibro Expert,*

1. INTRODUCTION

In the current context of the development of modern manufacturing, assembling, testing and exploitation technologies, proactive maintenance plays an important role in reducing operating costs and increasing the competitiveness of technical systems for the production of energy using hydro-aggregates. The most important advantages of new hydroelectric power plant technologies are continuous monitoring of normal operating parameters for both stable and transient operating modes (when starting or stopping the plant). The framing of the measured vibration parameters within normal limits means safe operation, exceeding normal limits means a malfunction that can lead to a major fault and the decommissioning of the power plant, high power-interruption costs and high costs repair and restoration.

2. DATA ACQUISITION SYSTEM

The professional **VIBRO EXPERT** system is a professional diagnosis system used to implementing a *proactive maintenance program*. The **VIBRO EXPERT** diagnosis system contain two acquisition modules with eight channel, six measurement sensors for relative proximity vibration and accelerometer transducers **VibraSens**. (***Figure 1***). The integrated system of diagnosis monitors the *absolute vibrations* in the bearing area and also the *relative vibrations* of the proximity transducers.

The **VIBRO EXPERT** diagnosis system use also laser sensors where ale performed for several measurement and registration of main turbine shafts of hydro-aggregates **CAPMELLA** [1] and industrial equipments from **LUKOIL** company [2].

The relative vibrations were measured in first case [1] with eight proximity sensors without contact. Measurement of the relative vibrations of the shaft was carried out in two directions perpendicular to the four bearing area indicated by(***Figure 3***):

LGS - Radial Axial Generator Superior Bearing,
LGI - Lower Generator Bearing,
LI - Intermediate Bearing,
LT - Turbine Bearing.

The accelerometer used is a piezo-ceramic element subjected to shear with 100/500 mV / g ± 5% sensitivity produced by **Sendig Technology** type **VibraSens 101.51-9** (***Figure 1***). The synchronization, speed and phase transducer is a non-contact laser sensor produced by **Monarch Instruments** type **ROLS-W *(Figure 2).***

The measurements are synchronized by the phase sensor mounted on the four bearing area. (***Figure 4*).**

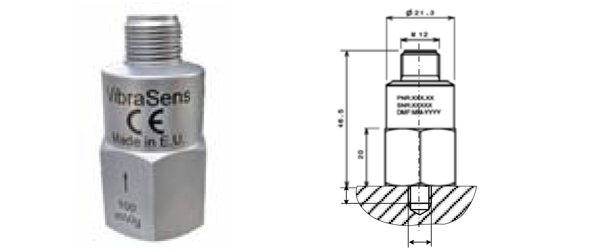

Figure 1.

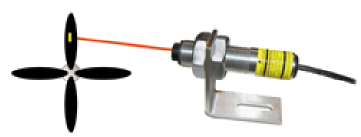

Figure 2.

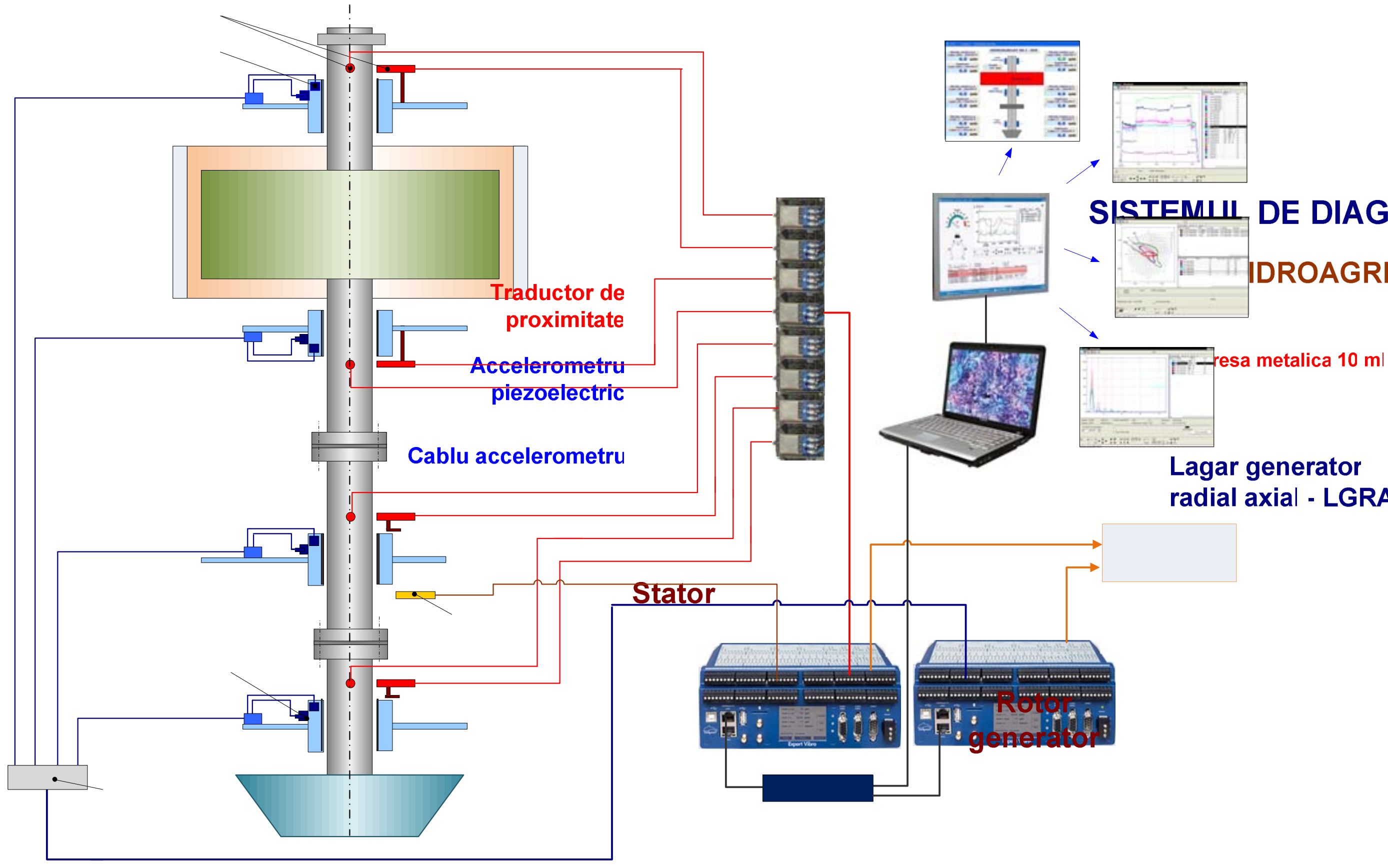

Figure 3. The integrated acquisition and EXPERT VIBRO diagnosis system

Lagar generator radial inferior - LGI

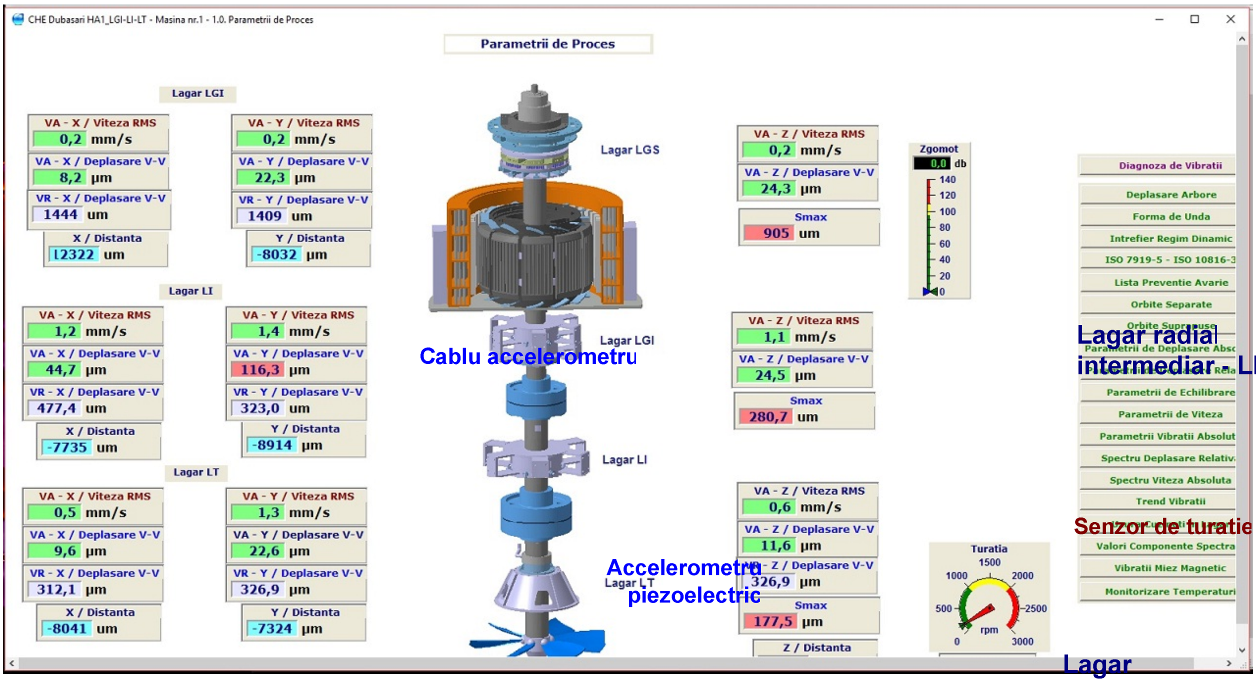

Lagar turbina LT

Figure 4. The process monitoring parameters of LGS , LGI , LI and LT bearings along X, Y, Z directions

Cutie conexciuni accelerometre

Rotor turbină

The analysis module of vibration has the following characteristics:
- the general analysis and tracking analysis (vs. time / vs speed / vs harmonics),
- the spectral analysis (FFT, auto spectrum, phase spectrum)
- the tire analysis - alarm and signaling functions; orbits; time capture; phase analysis facilitates the storage of large data volumes in real time; Statistical analysis module (mean, median, variant, coherence, kurtosis analysis etc); flexible graphical user interface (automatic axis adjustment, etc.). The system interface displays all measured data and the charts resulting from data processing.

The **VIBRO EXPERT diagnosis system** can store important measurement data in a database that can be transferred to an external server. The **VIBRO EXPERT diagnosis system** is equipped with the professional software for data acquisition, processing , presentation, diagnosis, archiving named **PROFISIGNAL**. The **PROFISIGNAL** software is compatible with the hardware part of the computer system that can measure, monitor, and analyze vibration amplitudes. Vibration measurements can be purchased and viewed online and also off-line. The software allows you to display in 2D or 3D several types of measurements such as [3], [5], [6]:
- Global vibration,
- Spectrum frequencies
-Waveform (amplitude based on time),
- The shaft orbit in the bearing (the relative vibration),
- Bearing state measurements (bearing envelope),
- Phase-speed measurements, etc.

In order to obtain correctly diagnoses in the operating status of the equipment, the module **PROFISIGNAL** software allows [7], [8]::
-simultaneous display of measured data across multiple channels. The data will be saved and written in real time directly on the hard disk ;
- fittings of the order of 2 ... 10 selectable, low pass filter, high pass and band, mediation and signal integration will be available.

Operating System Computer hardware: Windows 7, Windows 2000 / XP.

The **PROFISIGNAL** software allows to create virtual computing channels directly in order to obtain any vibration or technical parameter by mathematical relationships. The vibration parameters that can be calculated using **PROFISIGNAL** software are [4], [5]:
- Peak-peak, mean, effective RMS, 0-peak, 0-lower,
-Amplitude and main frequency,
-Speed and phase at main amplitude,
-Amplitude and fundamental phase 1 x,
-Amplitude and component phase 2 x, 3 x, 4 x etc.
-The maximum value of the vector sum for 2 signals
-The average product for 2 signals,
-Frequency of main amplitude for 3 frequency bands,
-Main amplitude for 3 frequency bands,
-Efficient RMS value for 3 frequency bands, etc.

Figure 5.

3. TECHNICAL CONDITIONS OF MEASUREMENT

Vibration measurements of parameters were performed with proximity sensors for **relative vibration measurement** in accordance with ISO 7919-5 [15] and with accelerometers for **absolute vibration measurement** in accordance with ISO 10816-5 [18]. Vibration measurements were performed on three X, Y, Z directions.

Figure 5 show the CAMPELA hydro-aggregate and X, Y, Z directions of measurements on the bearing.

The measurements are synchronized by a phase sensor mounted in the machine axis area. The relative vibration of the shaft was measured in radials direction X-Y for the following bearings of hydro-aggregate [1]
- **LGS** -Superior Generator Bearing, which is also an Radial Axial Bearing
- **LGI** -Lower Bearing Generator
- **LI** -Intermediate Bearing
- **LT** -Turbine Bearing

The notations were used to determine the direction of measurement (***Figure 5***):
- X direction is similar to the upstream direction,
- Y direction - perpendicular to the upstream line,
- Z direction - parallel to the axis of rotation of the machine spindle.

The absolute vibrations were measured with acceleration transducers / accelerometers mounted as follows:
- two radial two directional sensors along X-Y axis
- one axial sensor along Z-axis

The standard ISO 10816-1/5 [17], [18] does not specify the admissible vibration value in axial direction Z .

With the diagnostics **VIBRO EXPERT** system, the technical parameters of global Vibration were measured an monitored:
- Relative vibration of the hydro-aggregate shaft according to ISO 7919-5 [14], [15]
- S_{max} value of vibration according to ISO 7919-5 [15],
- Absolute vibration according to ISO 10816-5[18],,
- Absolute speed vibration, and vibration of movement
- Shaft speed and vibration phase.
- The amplitude of the fundamental vibration
- the *1*x component and the phase for the determination of the imbalance vector

The S_{max} vibration parameter [μm] is defined [15] as the highest vibration value recorded on the bearing orbit relative to point :

$$S_{max} = \left[\sqrt{[S_{X1}(t)]^2 + [S_{Y1}(t)]^2}\right]_{max}$$

ISO 7919-5/ 2005 [15] and ISO 10816-5/ 2000 [18] provide the performance ratings of hydro-aggregate when it is energy-stable (***Table 1, Table 2***)

These operating ratings are classified as follows:
¬ **Qualification A** - Good / Vibration of newly installed machines falls within this area.
¬ **Qualification B** - Usable / Machine vibrations within this area are considered in normally, acceptable for unrestricted operation on long term.
¬ **Qualification C** - Admitted under supervision / Machines where the vibrations within this area are normally considered unsatisfactory for continuous, long-term operation. Generally, the machine can be operated for a limited time in this state until a suitable opportunity for remedial action appears. In this case, the machine can operate for a limited time, requiring repair programming
¬ **Qualification D** - Not allowed / Machines where vibrations within this area are considered as severe enough to cause damage to the machine.

ISO Standard 7919-5/2005 [15] recommends that vibration measurements relative to proximity systems are performed and the performance ratings are specified in the table below (150 rpm). (***Table 1***)

ISO 10816-5/2000 [18] indicates the performance ratings of hydro-aggregates for absolute vibration measurement with equipment that performs as a speed and displacement parameter in the 2 ÷ 1000 Hz frequency range. (***Table 2***).

Table 1. Performance ratings in according to ISO 7919-5/2005[15]

Machine		Hidroaggregate 150 rpm, P > 12 [MW]	
Measurement parameter		Displacement Pick- pick [μm]	Displacement S_{max} [μm]
Performance ratings	Good – A	under 155	under 85
	Usable – B	155 - 260	85 - 140
	Admitted under supervision – C	260 - 525	140 - 290
	Not allowed – D	over 525	over 290

Table 2. Performance ratings in according to ISO 10816-5: 2000[18]

Machine		Hidroaggregate 150 rpm, P = 12 [MW]	
Measurement parameter		Velocity [mm/s] rms	Displacement [μm] pick-pick
Performance ratings	Good – A	under 1,6	under 30
	Usable – B	1,6 – 2,5	30 – 50

	Admitted under supervision – C	2,5 – 4	50 – 80
	Not allowed – D	over 4	over 80

5. EXPERIMENTAL DATA

The diagnosis of hydro-aggregate operation was performed in all machine operating regimes described above by analyzing the **relative vibration** (displacement and S_{max}.) and the **absolute vibration** (speed and vibration movement).

Analyzing the vibration measurements, the highest amplitudes of relative vibrations were obtained on the **LGI** generator bearing, and then on the superior generator bearing **LGS.**

These high amplitudes have been recorded in all working regimes, resulting the Performance rating **D Not Allowed** - *See Global Relative Vibration Level Bulletin No. 1* [9] .

The spindle in the superior generator bearing **LGS** has a oscillation of level that has affected the correct measurement of relative vibrations by proximity sensors. To eliminate this large amplitude generated by spindle oscillation, the correct measurement were made from the wave / orbit waveform vibration. *In this respect it is recommended to process roughness R_a at the max. 6.3 μm (generator, intermediate and turbine) over an area of min. 40 mm in the proximity transducer probe read area, corresponding to each bearing, for future accurate vibration measurements (after machine repair).*

This spindle defect is highlighted by the orbit measurement of **LGS** bearing

Absolute vibration diagnosis, vibration velocity amplitudes, fit the machine to the Performance rating **B Usable** for 9.6 MW, and the Performance rating **A Good** for 4,8-7,2-12 MW - *See Global Speed Absolute Absolute Rate Bulletin no. 2* [10] .

From Vibration Movement measurements, the Performance rating **D Not Allowed** for all Load operating modes and the Performance rating **C Admitted under Supervision** for *Blank idle*. See *Global Absolute Movement Level* ***Bulletin No. 3*** [11]

The vibration measurements performed on the hydro-aggregate bearings were analyzed for the following **three regimes:**

5.1. Regime A: Without load/ not excited work regime At rotation speed : 120, 140, 150 and 165 rpm *(ANNEX 1)*

At the 120 rpm speed of the hydro-aggregate there was occurred an intermittent friction between the rotor and the generator, the orbit shown highlights this phenomenon. See *Annex 1:* ***Fig. 6 (A1)*** , ***Fig.7 (A6)***.

In this respect, it is recommended to check the rotor and the generator, especially in the LGS bearing area. For all rotation speeds at 120 140, 150 and 165 rpm, the relative and absolute vibrations were lower in this regimes than in the load regimes.

5.2. Regime B: Increase and decrease speed for Without load/ not excited work regime *(ANNEX 2)*

Upon increasing and decreasing speed to **150 rpm**, the vibration amplitudes relative to the generator bearings are significantly increased:

LGS - *610 μm* V-V (Peak-Peak) / X direction,

LGI - *889 μm* V-V (Peak-Peak) / X direction,

This values exceeding the allowable limit of standard ISO 7919-5 [15] admissible limit is *525 μm V-V (Peak-Peak).* Hence, the machine operates with high vibrations since the Without load/ Idle regime. *Annex 2 –* ***Fig.8 (A.25), Fig.9 (A26)*** [12]

Absolute vibration analysis for the same work regime **increase and decrease speed** was performed in two ways, namely: *vibration velocity* and by point of view of *absolute displacement.*

In the case of the *vibration velocity analysis*, it can be seen that the highest value was recorded on the **LI / Y direction** – RMS *1.37 mm/s* , and this value is **Good rating A.** ***Annex 2: Fig.10 (A.46), Fig.11(A.47)*** [12]

In the case of the vibration displacement, the highest value was also recorded on the intermediate bearing **LI / Y direction,** *67 μm V-V* (*Peak-Peak*) but this value making the machine qualify as **Admitted under supervision** rating. *Annex 2* ***Fig.12 (A.57), Fig.13 (A.58)*** [12]

5.3. Regime C: The comparative analysis between Without load/not excited work regime and the Load/ excited work regime

5.3.1. The comparative analysis C1. Analysis of relative vibration *(ANNEX 3)*

The amplitudes of relative vibrations recorded on the lower bearing **LGI** and the intermediate bearing **LI** increased significantly with the **Load/ excited work regime** for rotation speed at 150 rpm, practically doubled compared to **Without load/not excited work regime.** *Annex 3 –* ***Fig.14 (A.28), Fig.15(A.29)***. [12]

The magnitude of the amplitudes relative vibration measured to the lower bearing **LGI** are *1462 μm V-V (Peak-Peak) (7.2 MW)* exceeded three times the admissible value *525 μm V-V (Peak-Peak).*

By analyzing the FFT frequency spectra, this large increase of amplitudes may be due to several causes, namely *non-uniform air gap*, which leads to an *electrical imbalance* corroborated with *bearing faults* and *shaft misalignment*. *Annex 3, Figure A.38* [12]

From the LGI bearing orbit analysis, it can be observed that when the machine is at load (4.8 MW ... 12 MW), it *flattens slightly,* leading to additional loading of the bearing and occurrence in the frequency spectrum of the upper *2×* *3×* and *4×* components. *Annex 3 - Figure A.39.* [12]

For this type of defect, it is recommended, in the first phase, to check the weaknesses of the **LGI bearing** (bearing wear, cracks, etc.), then the air gap and the de-stressing of the shafts. The orbit recorded at this LGI bearing highlights this phenomenon. *Annex 3 – **Fig.17 (A.16), Fig.18 (A.17)***. [12]

After these checks, it is advisable to perform a new set of measurements in which to analyze the mechanical imbalance vector. If it exceeds the allowable value specified in ISO 1940, it is recommended to perform the dynamic balancing of the generator rotor.

The same conclusions can be made to the S_{max} parameter analysis. *See Global Relative Vibration Level Bulletin No. 1* [12]

In most cases, the phenomenon is inversely, i.e. when it's empty, the vibration level is higher than the load regime, and this happens when the air gap bearings are admissible, the alignment of the shafts is correct and the residual mechanical imbalance is admissible.

This phenomenon is explained as follows: when the electromagnetic field occurs (Load regime) takes place concentricity in the electro-magnetic field of the rotor with the increase of the forces in the generator bearings. If the bearing has excessive weaknesses or wear, vibration amplitudes increase significantly, which leads to the loading of the bearing.

Another phenomenon can be observed on the relative vibration measurements is namely: the displacement above X-direction shows significant increases by short-term impulses over *1000 μm V-V(Peak-Peak)* when the aggregate passing from 7.2 MW to 9, 6 MW. *See Annex 3- **Fig.19 (A.31)***. [12]

These impulses can be generated by machine instability on the X direction (upstream - downstream direction) in additional with hydraulic forces and cavitations phenomenon. This phenomenon is also emphasized by the *analysis of the orbits and frequency spectra* recorded on the turbine bearing. *Annex 3 – **Fig.20 (A.32), Fig.21 (A.34)***[12]

5.3.2. The comparative analysis C2.
Analysis of absolute vibration *(ANNEX 4)*

When analyzing the absolute vibrations, the same phenomenon can be emphasized: significant increase of the vibrations with the **Load/ excited work regime** for rotation speed at 150 rpm, practically doubled compared to **Without load/not excited work regime**. *Annex 4 – **Fig.22 (A.42)**, **Fig.23 (A.48)***. [12]

The absolute vibration frequencies spectra performed on the hydro-aggregate bearings and on the excitation body highlight the following aspects:

- The highest absolute vibration found in the spectrum recorded on the excitation body is due to the component *7× = 17.5 Hz (7× 2.5 Hz = 17.5 Hz,* where 2.5 Hz is the rotation speed of the machine *150 rpm / 60 = 2.5 Hz).*
- This vibration is due to a weakening in the area of the generator or its foundation. In this respect, it is advisable to check the generator bearings, their stiffening elements, the upper and lower star and including the generator base.
- The value of the 7x component changes depending on the machine rotation speed: at 150 rpm, the amplitude of the velocity was *RMS 3.84 mm / s* and at 165 rpm the value dropped to *RMS 2.17 mm / s. Annex 4 – **Fig.24 (A51)***. [12]

Highest velocity values were recorded at without load on speed of 140 rpm - above *RMS 25 mm / s. Annex 4 – **Fig.25 (A.42)*** [12] .

Practically at the 135-140 rpm speed of the hydro-generator, the weakening is excited to the maximum - possibly the resonance input of a component of the generator or foundation. In Load regime, the vibration value varies depending on the size of the load at 12 MW, the speed value measured is *RMS 7.08 mm / s. Annex 4 – **Fig.26 (A.52)***. [12]

- Analysis of FFT spectra on the LGI camp results in higher order spectral components with admissible level in which the 7x component is also found. The overall RMS vibration speed is relatively small, meaning that the bearing is rigid given that the relative displacements have the highest values on the machine. These large displacements of the spindle are damped by the oil film and possibly by excessive wear of the bearing or the weakening of the bearing components to the carcass, where the absolute vibration level is permissible.
- The highest vibration speed values are found on the intermediate bearing **LI,** and the FFT spectrum recorded on this bearing indicates excessive gap air, over order components, including 7x that lead to *RMS 1.1 mm / s. See Annex 4 – **Fig.27 (A.54)**.* [12]
- Speed values recorded on the turbine bearing give the **Good rating A** and the frequency spectrum indicates admissible air gap bearings due to the hydraulic forces. *See Annex 4- **Fig.28(A.55)***. [12]
- Absolute displacement frequency spectra indicate the same types of defects, with the exception that they highlight the low frequency spectral components and the global values given by this parameter place the machine at a **Non-allowed D rating**. *See Annex 4- **Fig.29 (A.61)***[12]
- The absolute displacement orbit is shown in *Figure A.64* [12], where the motion of the bearings in space on the X-Y directions can be observed. From here it can be concluded that the hydro-aggregate bearings have a more pronounced displacement in the X direction.

6. CONCLUSIONS

For the quality of the hydro-aggregate repair, and proactive maintenance the following recommendation are made:

- Verification of air gape / tolerances in the hydro-aggregate bearings, especially in the **LGI** and **LGS** bearings and if they correspond to the machine repair card;
- Verification of weaknesses in **LGI** inferior generator bearing - cracks or exfoliations in the cuff, loosening of pills or bolts, etc.;

- Practically checking the rigidity of the bearing. It is recommended that the same checks be applied to the axial radial bearing **LGS - LI – LT;**
- Checking the air gap, due to the significant increase in relative vibration amplitudes and absolute displacement on the **LGI** and **LI** bearing when the hydro-aggregate is in charge;
- Achievement of shaft alignment / generator shaft - intermediate shaft - turbine shaft / according to the hydro-aggregate mounting documentation. For this operation high precision digital device meters, proximity sensors or comparator watches can be used;
- Making new vibration measurements in order to calculation of the permissible deck of the generator rotor. If this does not correspond, the dynamic rotor balancing is recommended.

When manufacturer's tolerances are not available the tolerances are shown below in *Table 3*, this is based on the recommendations of Bill Duncan work: *"Bureau of Reclamation Plumb and Alignment Standards for Vertical Shaft Hydro-units"*. [13] .

Table 3.

Type of measurement Tolerance	Recommendation:
Stator switch	± 5% of rated design air gap
Stator concentricity (depending on turbine bearing)	± 5% of rated design air gap
Concentricity of the upper generator LGS (depending on the LGI lower bearing and the LT turbine bearing)	20% of the bearing diameter of the bearing
Concentricity of the lower LGI generator (depending on the LGS upper bearing and the LT turbine bearing)	20% of the bearing diameter
Concentricity of sealing ring	10% of diameter seal of sealing ring
Stator circularity	± 5% of nominal design air gap
Rotor circularity	± 5% of rated design air gap
Rotor Vertical	± 5% of rated design air gap
Shaft Linearness	<0.076 mm - No reading point shall have a deviation greater than 0,076 mm from a vertical straight line linking the reading point higher than the lower one
Static shaft deviation	<0.05 mm multiplied by the shaft length in the axial bearing to the deviation measurement point divided by the rotor diameter in the axial bearing section
Deviation of the center of the shaft	<0.00000025 x measured shaft length from the upper reading position to the lower reading position

REFERENCES

[1] Case study regarding measurements implemented with the repair entry a hydrogregate CAMPELA with vibro expert diagnosis system – Ionel Rusa, Cornel Marin, Marius Baidoc - International Conference ICOMECYME 2017, Bucharest, Romania

[2] Some results of vibroacustical diagnosis for industrial equipment in LUKOIL REFINERY– Ionel Rusa, Cornel Marin - 8th International Conference MECAHITECH'16, Bucharest, Romania

[3] Introducere în vibrații - Ref.Doc.MI 119 – Notă tehnică / Mobil Industrial – Pitești (2013)

[4] Mentenanța utilajelor dinamice vol . 1 – Mobil Industrial AG – Pitești (2011)

[5] Vibration Calibration Technique and basics of Vibration Measurement - Torben R. Licht – Singapore 2011

[6] An Introduction to Vibration Analysis Theory and Practice

[7] Automated machinery maintenance – Bill Powel , Tony Burnet

[8] Bearing vibration analysis – Connected Technology Center - Training modules

[9] *S.C. VIBRO SYSTEM S.R.L. www.vibrosystem.ro - Global Relative Vibration Level Bulletin No. 1.*

[10] *S.C. VIBRO SYSTEM S.R.L. www.vibrosystem.ro - Global Speed Absolute Abs. Rate Bulletin no. 2.*

[11] *S.C. VIBRO SYSTEM S.R.L. www.vibrosystem.ro - Global Absolute Movement Level Bulletin No. 3*

[12] *S.C. VIBRO SYSTEM S.R.L. www.vibrosystem.ro – MEASUREMENT TECHNIC REPORT sept 2016- ANNEXE 1*

[13] Bill Duncan - "Bureau of Reclamation Plumb and Alignment Standards for Vertical Shaft Hydro-units".

[14] ISO 7919-1 : 1996 Vibrații mecanice ale mașinilor. Măsurarea arborilor rotativi și criteriile de evaluare.Partea 1: Prescripții generale.

[15] ISO 7919-5 : 2005 Vibrații mecanice. Evaluarea vibrațiilor mașinilor prin măsurători ale arborelui rotativ. Partea 5: Hidroagregate și pompe.

[16] ISO 10817-1 : 1998 Sisteme de măsurare a vibrațiilor relative a arborilor rotativi. Partea 1: Detectarea vibrațiilor absolute și relative radiale.

[17] ISO 10816-1 : 1995 Vibrații mecanice. Evaluarea vibrațiilor mașinilor prin măsurători pe părțile non-rotative. Partea 1: Prescripții generale.

[18] ISO 10816-5 - 2000 Vibrații mecanice. Evaluarea vibrațiilor mașinilor prin măsurători pe părțile non-rotative. Partea 5: Hidroagregate și pompe.

ANNEXE 1

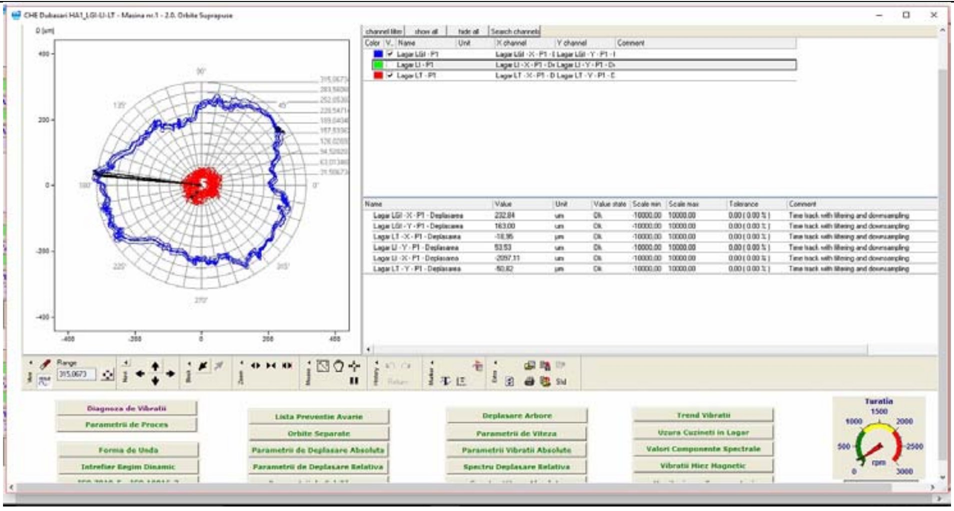

Fig.6 (A.1)

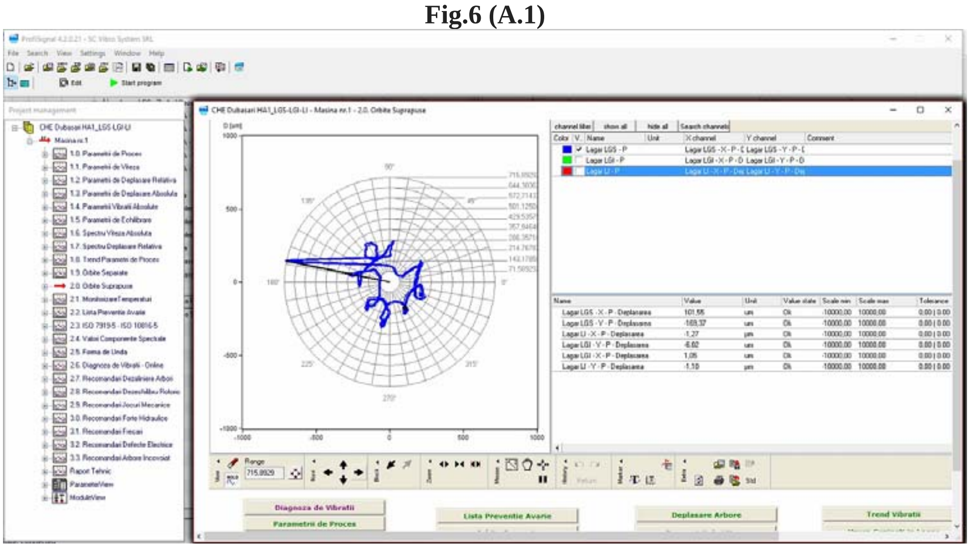

Fig.7 (A.6)

ANNEXE 2

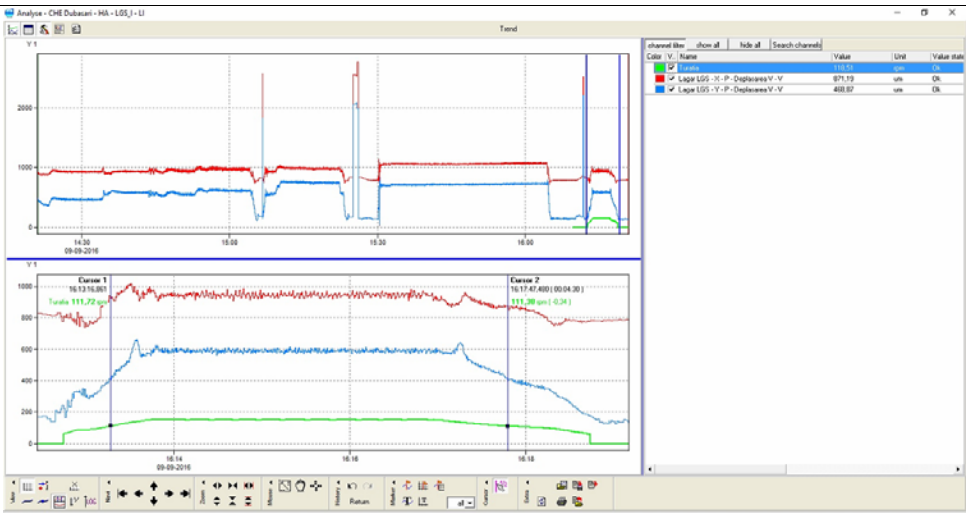

Fig.8 (A.25)

Fig.9 (A.26)

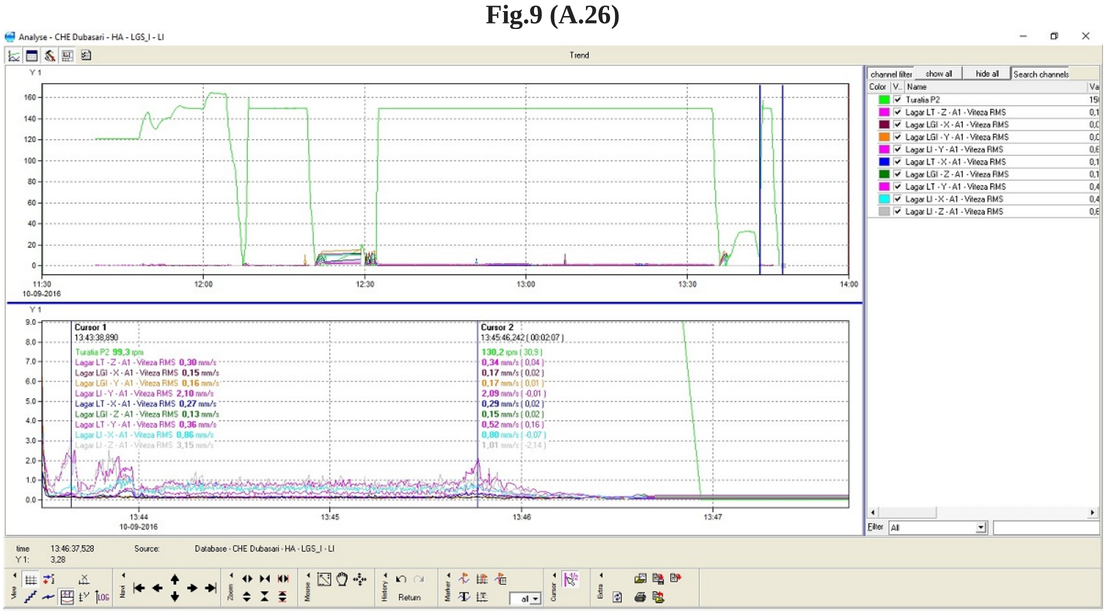

Fig.10 (A.46)

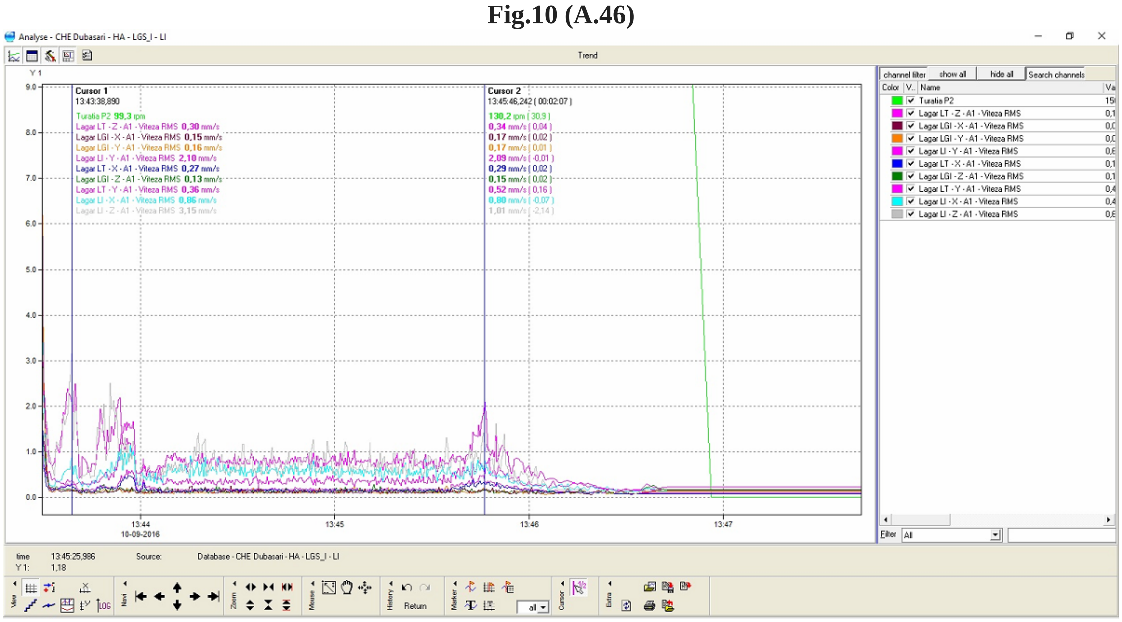

Fig.11 (A.47)

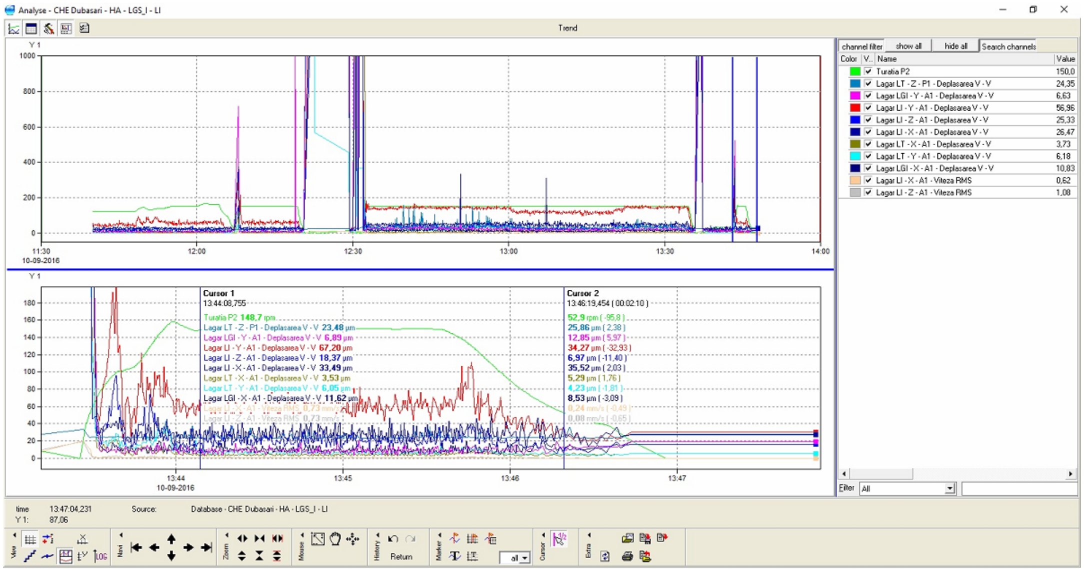

Fig.12 (A.57)

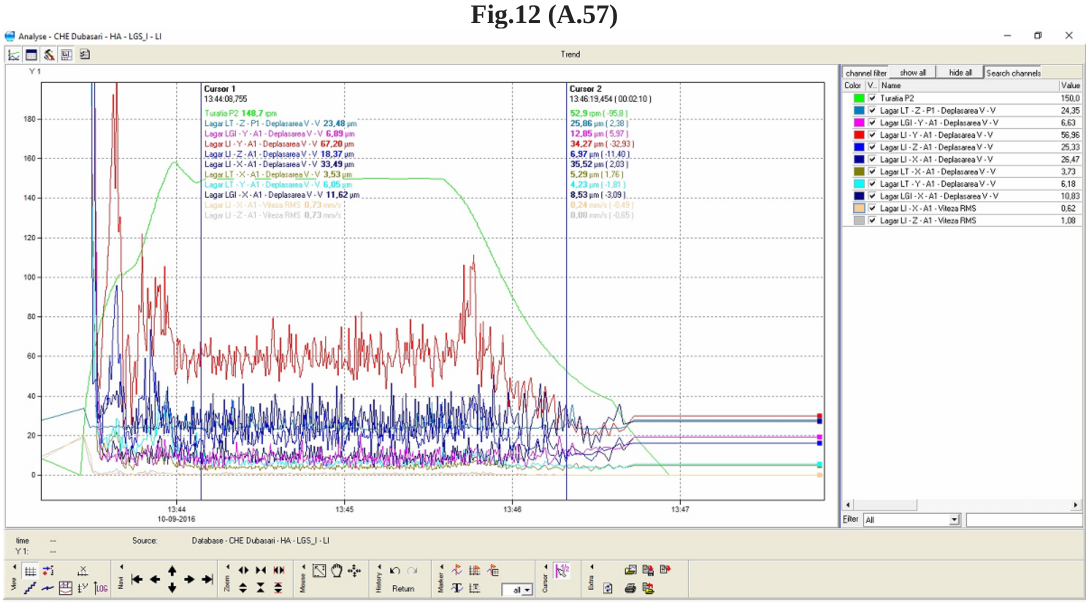

Fig.13 (A.58)

ANNEXE 3

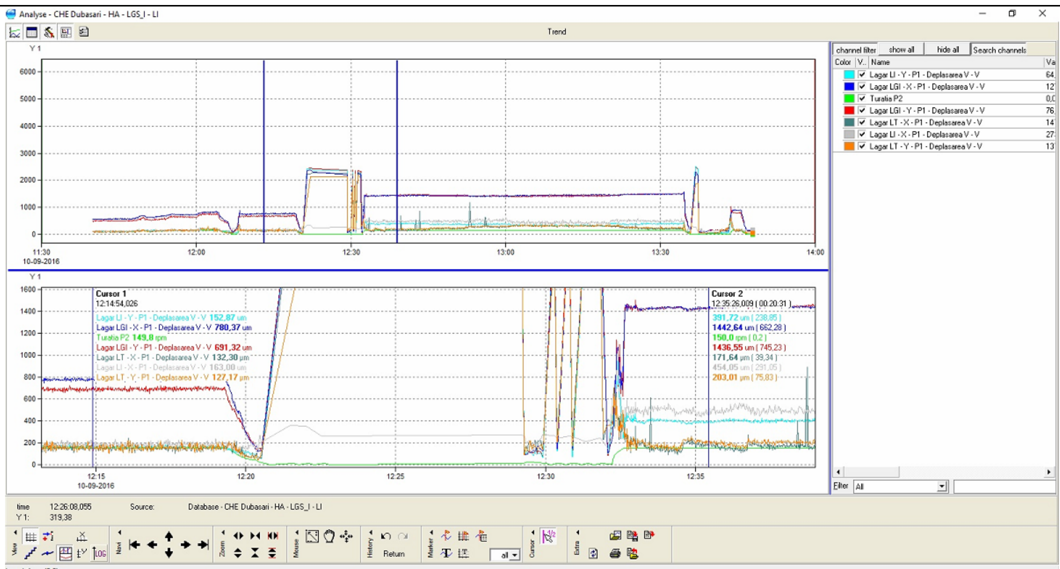

Fig.14 (A.28)

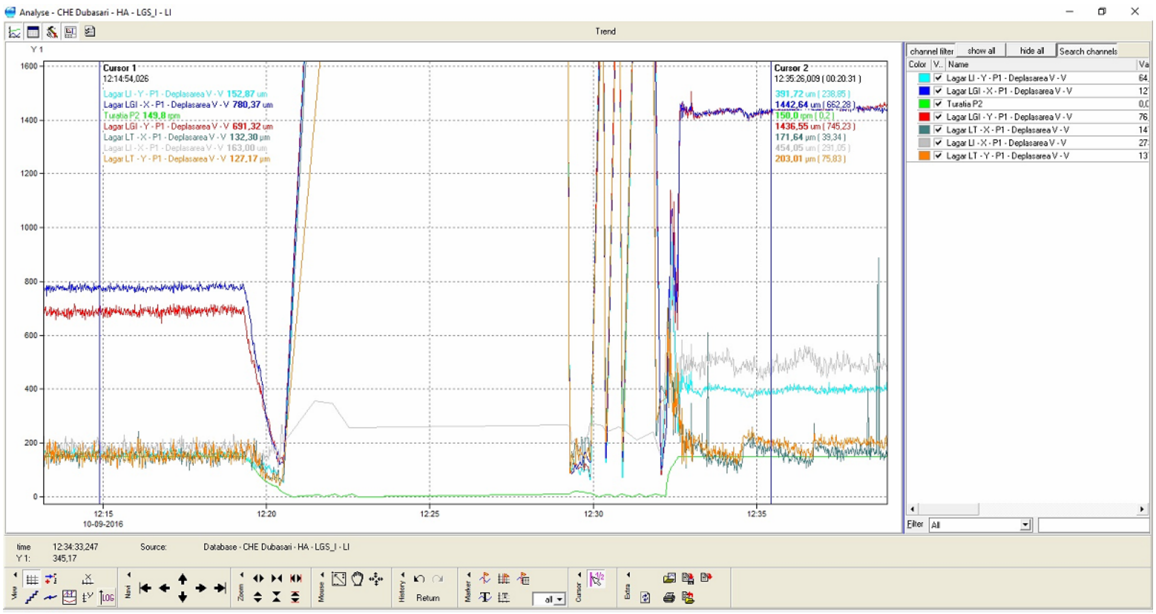

Fig.15 (A.29)

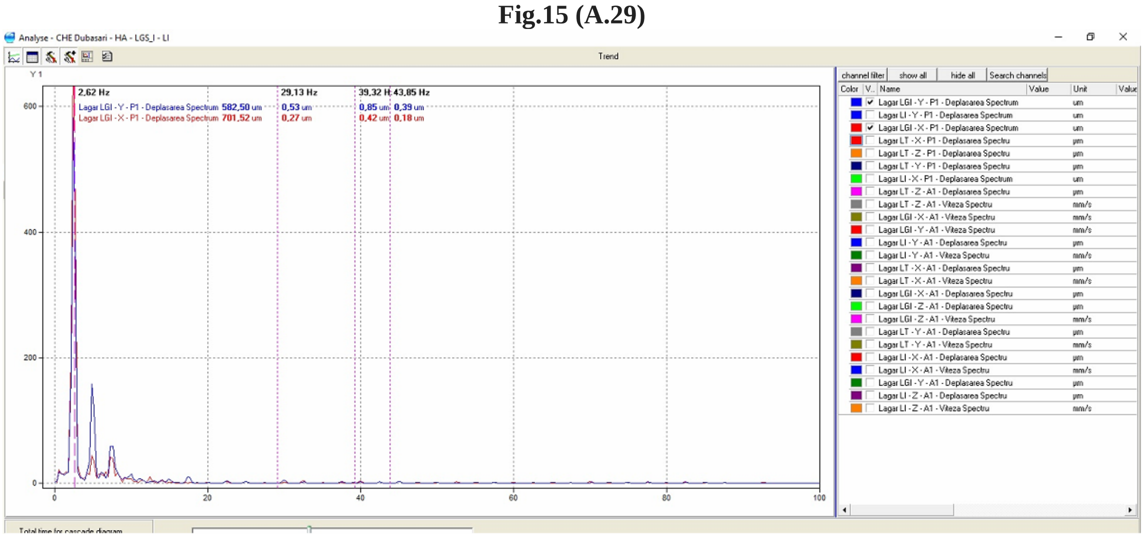

Fig.16 (A.38)

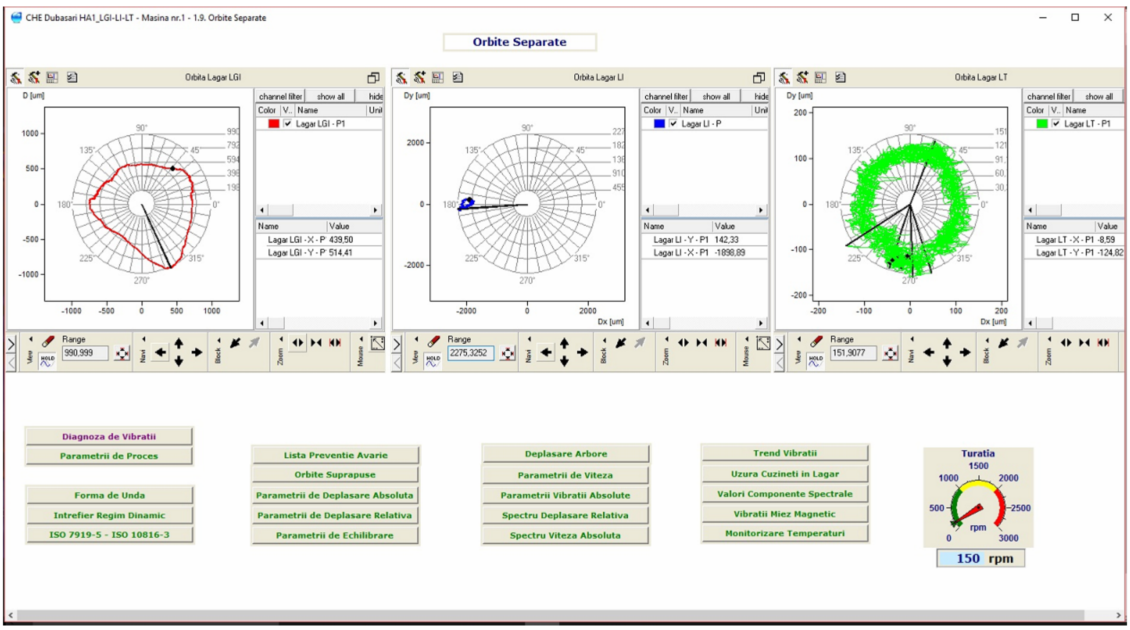

Fig.17 (A.16)

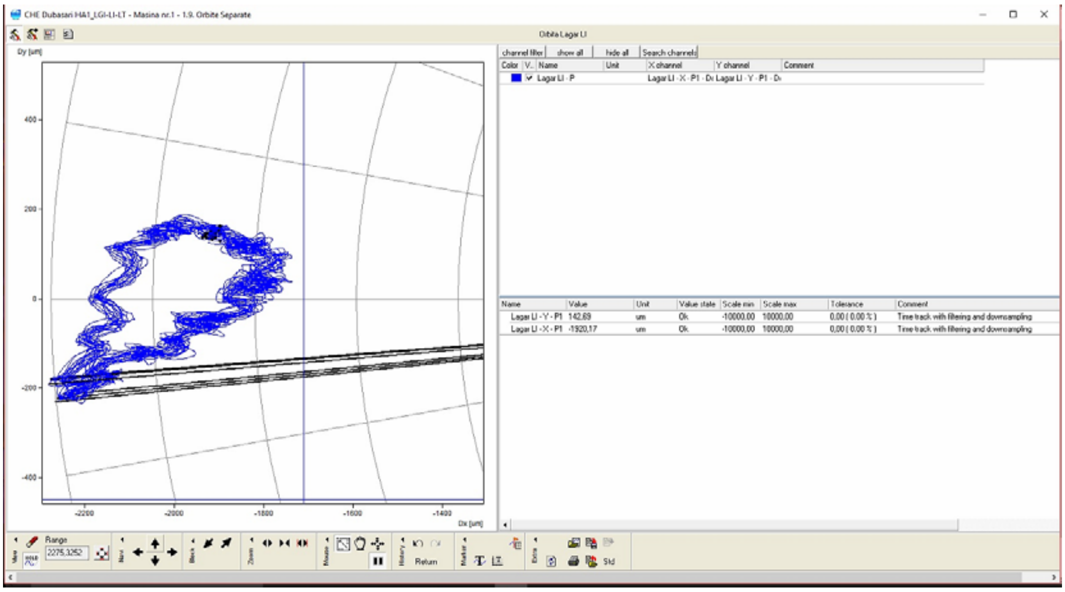

Fig.18 (A.17)

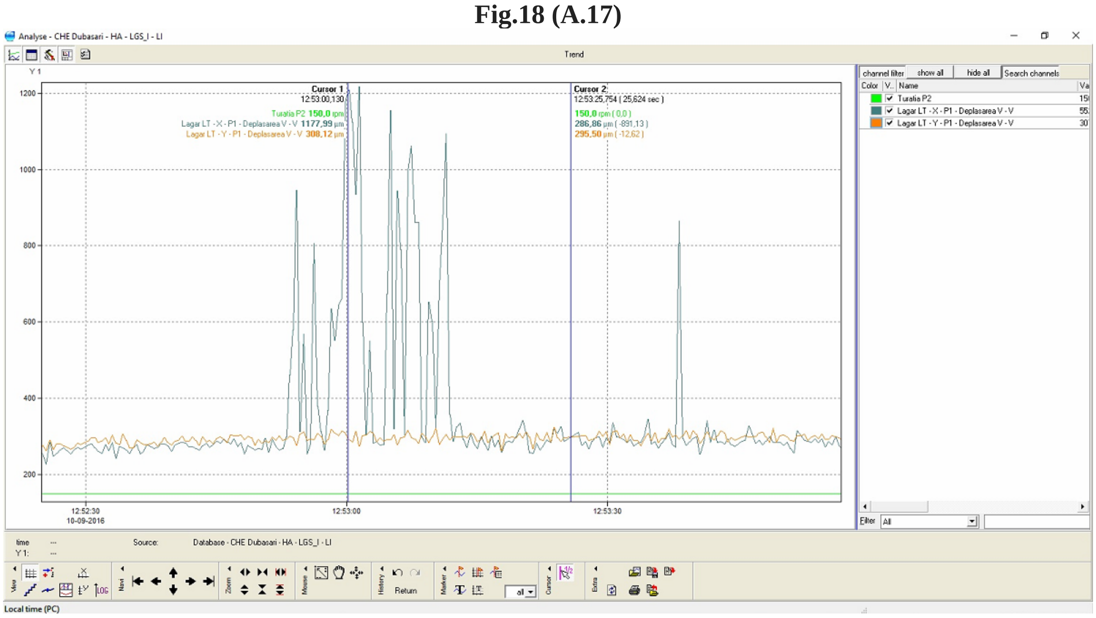

Fig.19 (A.31)

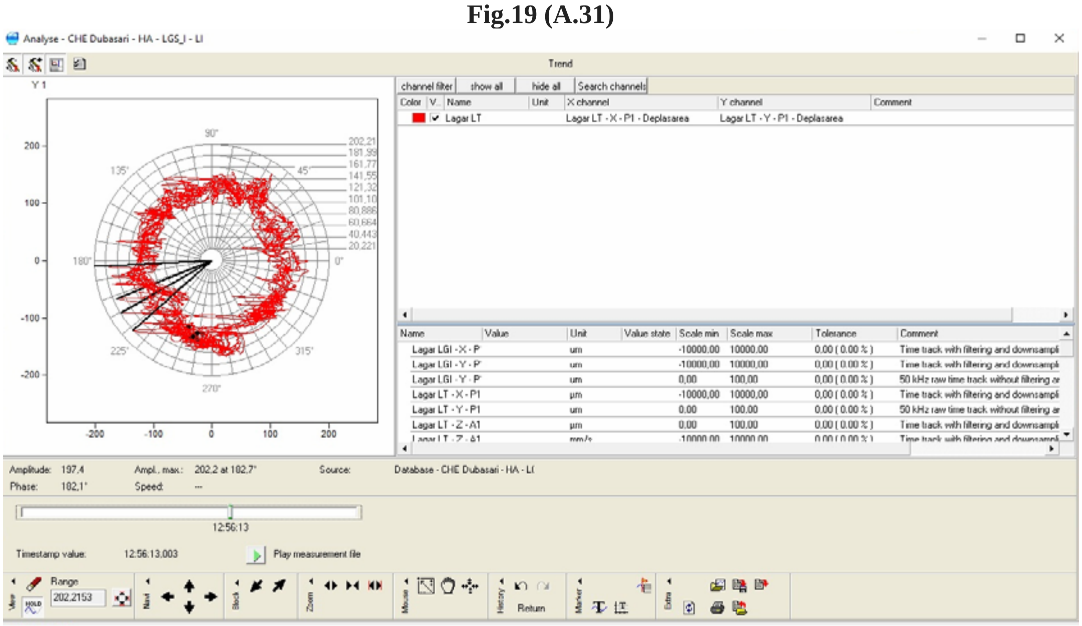

Fig.20 (A.32)

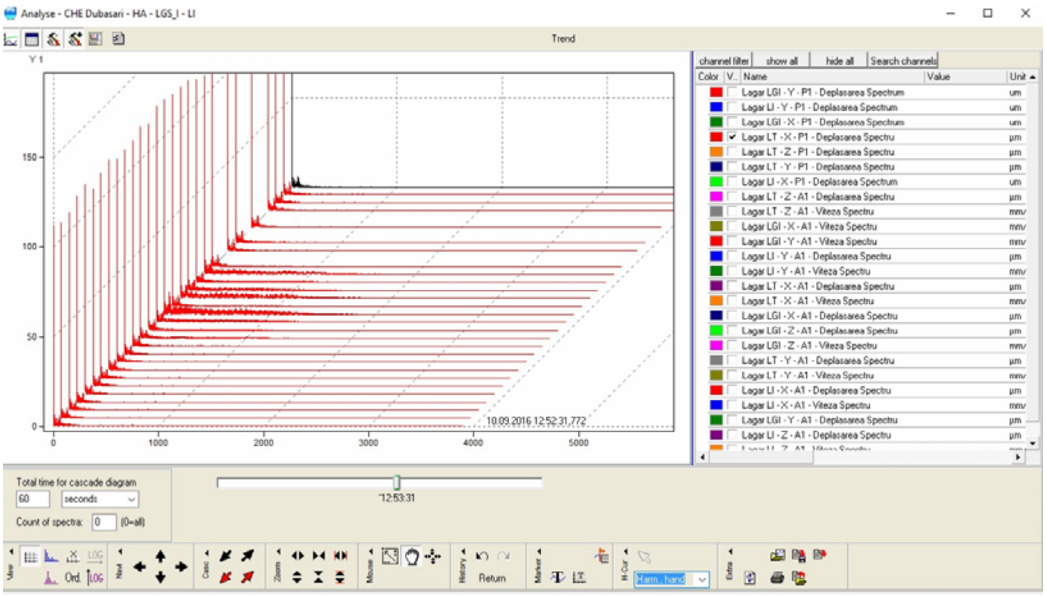

Fig.21 (A.34)

ANNEXE 4

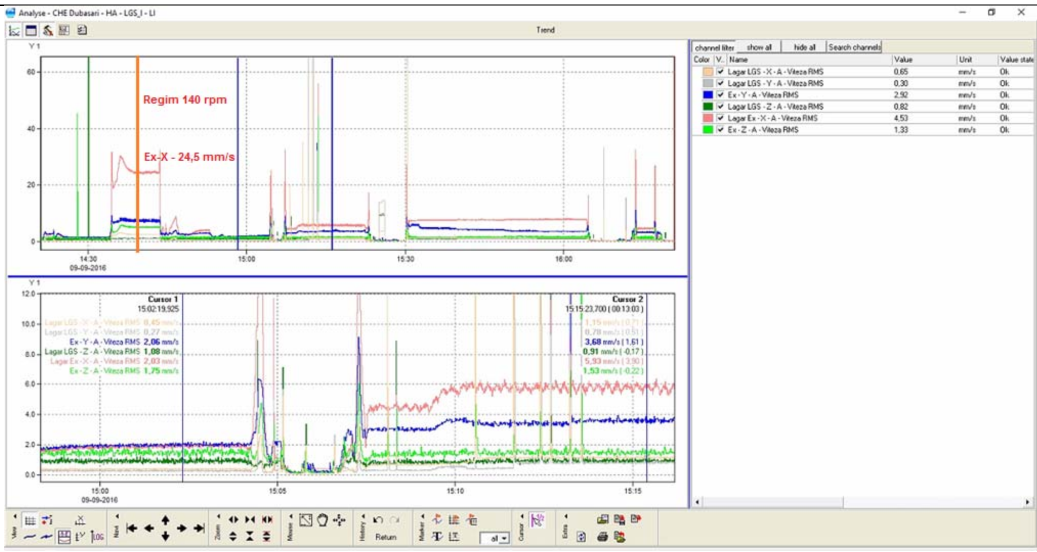

Fig.22 (A.42)

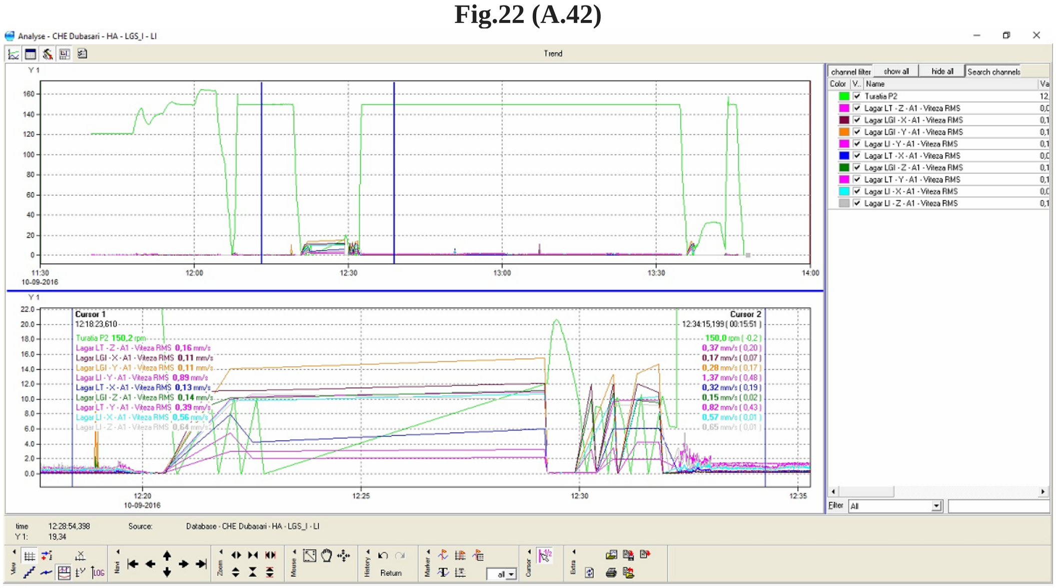

Fig.23 (A.48)

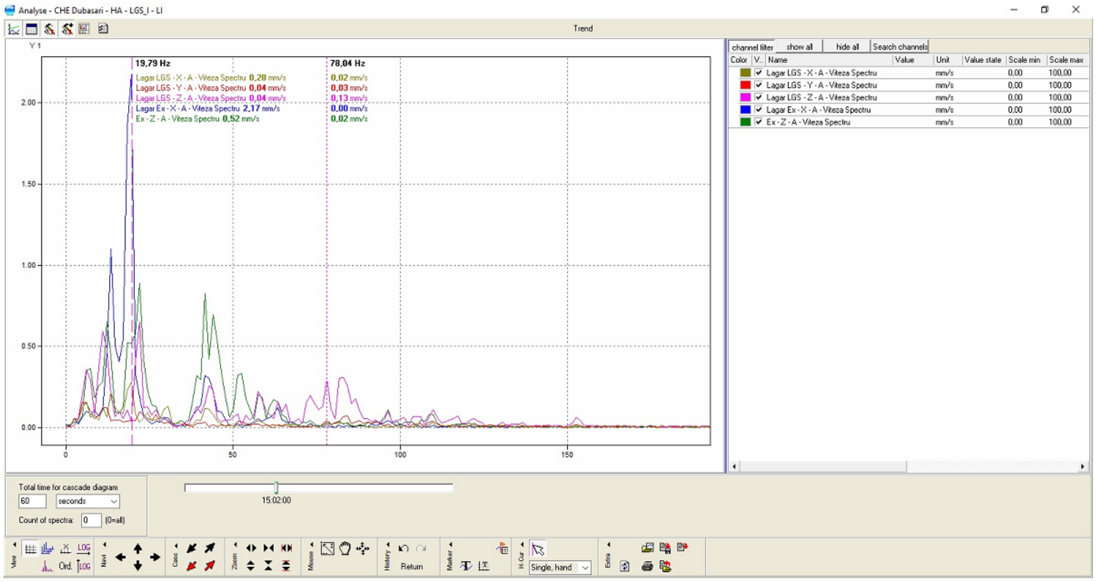

Fig.24 (A.51)

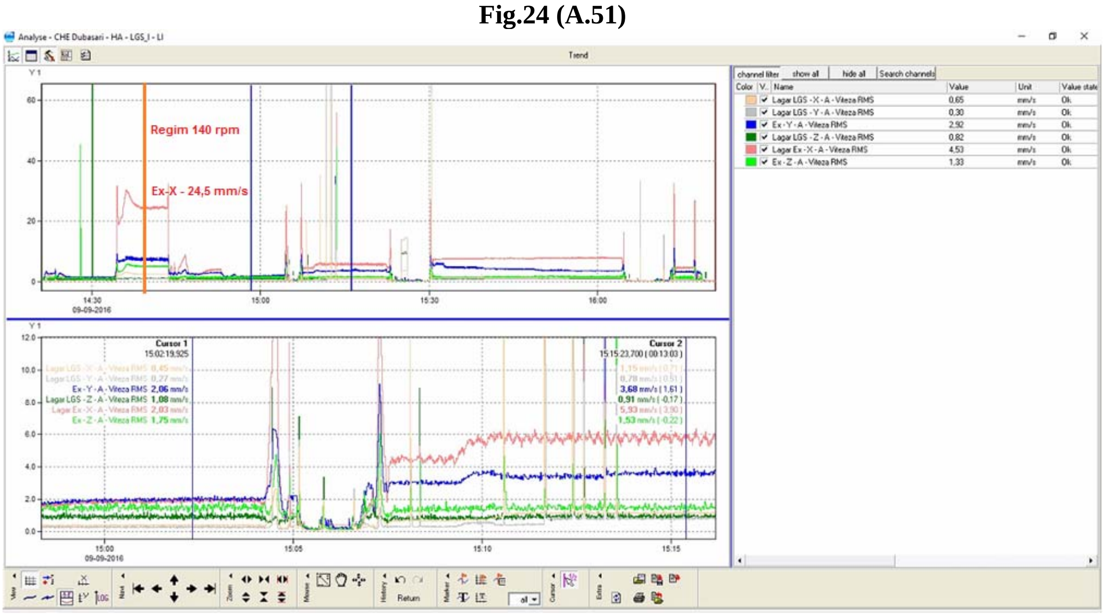

Fig.25 (A.42)

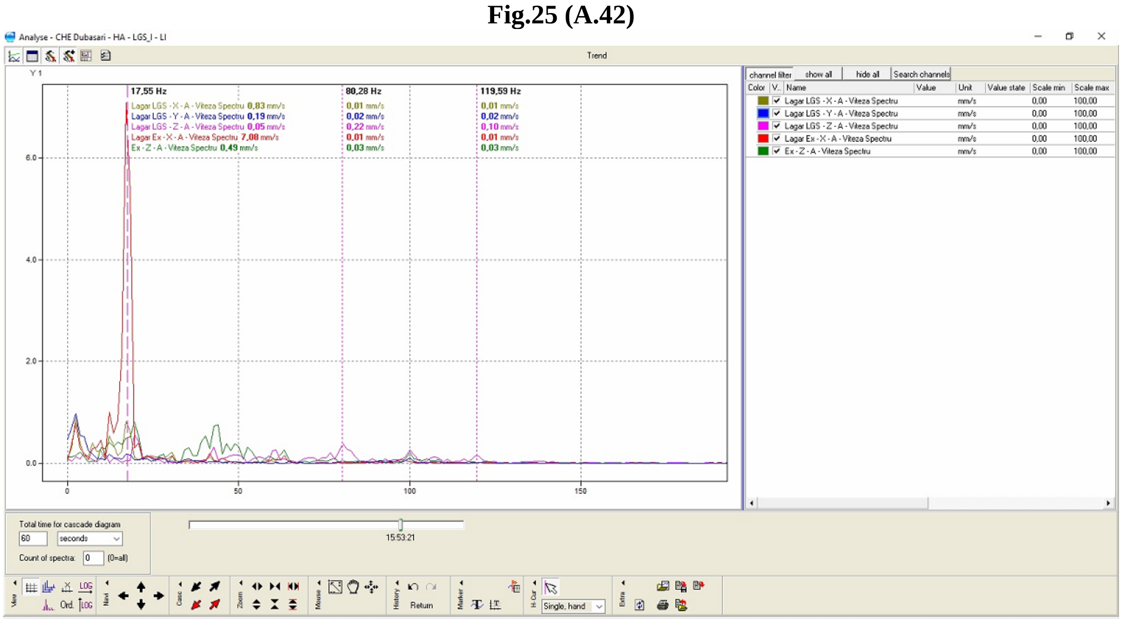

Fig.26 (A.52)

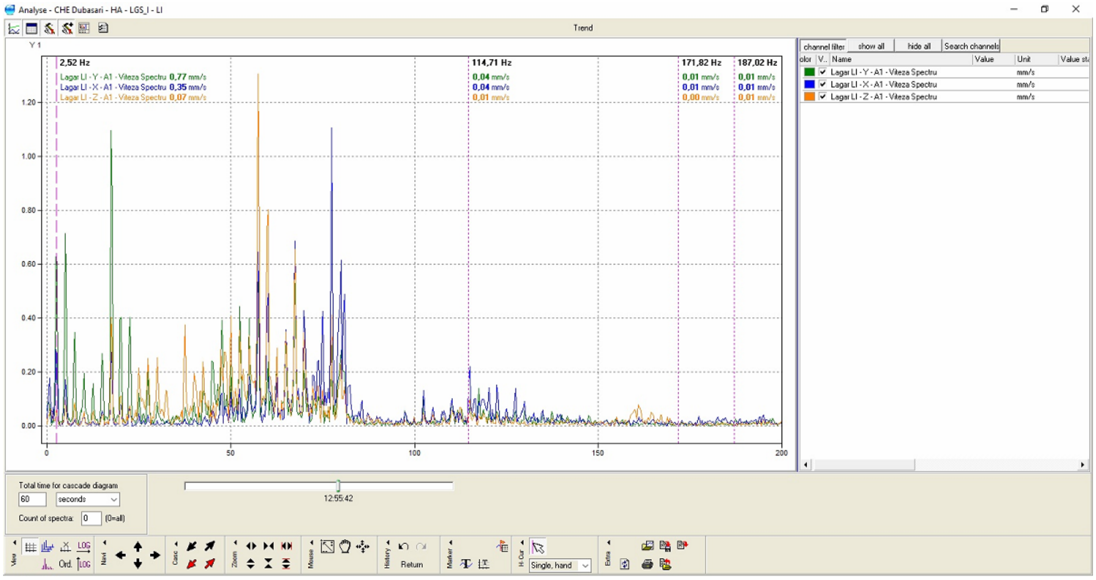

Fig.27 (A.54)

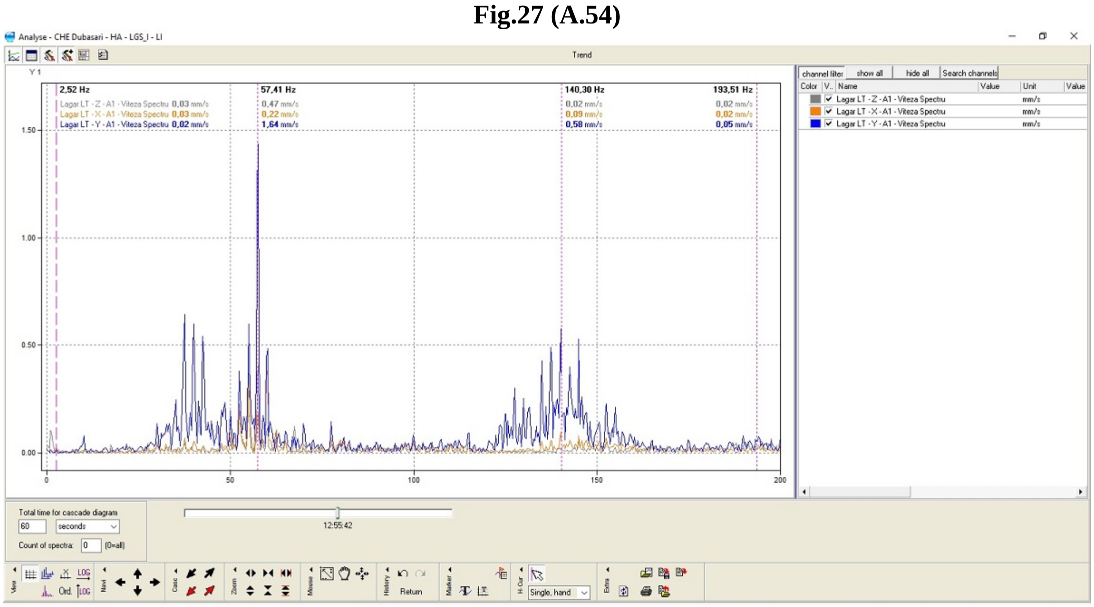

Fig.28 (A.55)

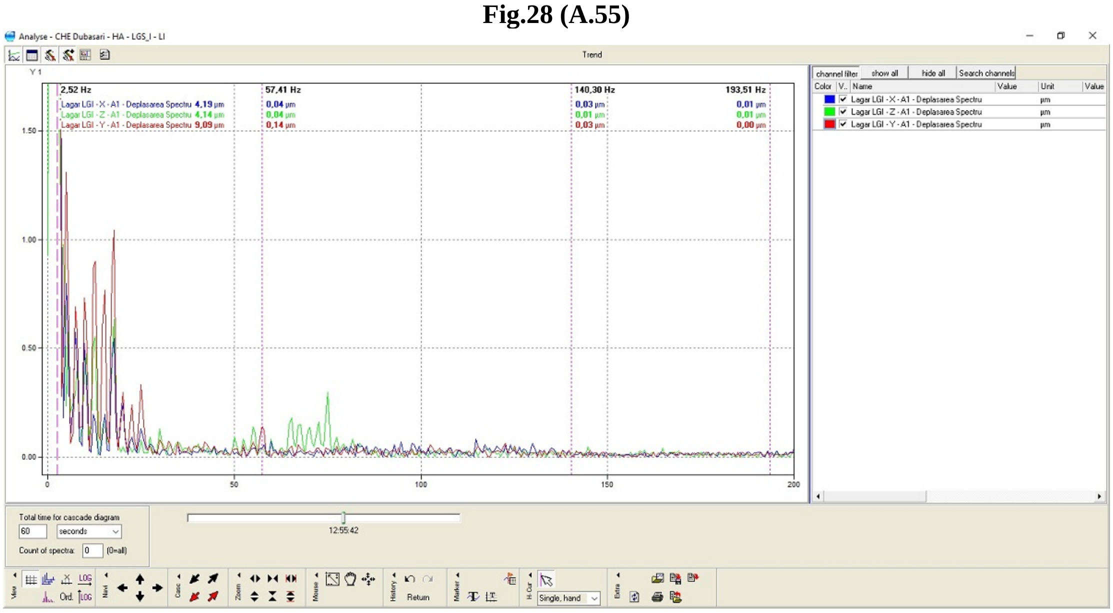

Fig.29 (A.61)

The Scientific Bulletin of VALAHIA University
MATERIALS and MECHANICS –Vol. 15, No. 13

DOI 10.1515/bsmm-2017-0019

NEW CONCEPTS ON MAKING OF MECHATRONIC AND CYBER-MIX-MECHATRONIC SYSTEMS

Gheorghe Ion GHEORGHE[1], Vasile BRATU[2], Adriana CÎRSTOIU[2], Veronica DESPA[2]

[1]National Institute for Research Development in Mechatronics and Measurement Technique, Bucharest
6-8 Pantelimon Road, District 2, Bucharest, Romania
[2]Valahia University, Bd. Carol I, Nr. 2, 130024, Târgoviste, România

E-mail: incdmtm@incdmtm.ro, vbratu@yahoo.co.uk, adriana_cirstoiu@yahoo.com, dumiver@yahoo.com

Abstract: *The scientific paper presents in summary the new concepts regarding the realization of cyber-mix-mechatronic systems with different industrial and societal applications.*

Keywords: concept, complex multiaplicative cyber-mix-mechatronic system, applicative cyber-mix-mechatronic system.

1. INTRODUCTION

This paper responds to the "challenge in the paradigm of European strategy" to create and develop new scientific concepts and new intelligent multiaplicative systems into new industrial value chains by combining and merging various skills and innovative solutions, but especially new mechatronic technologies, cyber-mechatronics and multidisciplinary cyber-mix-mechatronic solutions and their integration into advanced high-tech solutions and skills with IT & C for more advanced and smart products, systems, and systems of systems.

2. THE NEW CYBER-MIX-MECHATRONIC CONCEPT INTEGRATED IN THE ARCHITECTURE AND CONSTRUCTION OF MULTIAPLICABLE CYBERNETIC SMART SYSTEMS

The integration of the new complex concept includes the flexible fusion of the smart-mechatronic, cyber-mechatronic and cyber-mix-mechatronic systems architecture, expressed through complex sensor and actuator structures, located on the static and / or mobile physical work systems and equipment that transmit information to smart 4G devices that process, store and transmit to monitoring / remote monitoring entities / centres for command and / or databases [1].

By using smart 4G devices allows remote, real-time monitoring and diagnostics for all static and mobile smart mechatronic systems and equipment.

Multiaplicative adaptive mechatronic, cyber-mechatronic and cyber-mix-mechatronic systems for use and development will be in the form of "black box" entities that will innovate the hardware and software circuits for capturing, modelling and communicating data to / from the "control centre".

The architecture of multiaplicative adaptive mechatronic, cyber-mechatronic and / or cyber-mix-mechanic devices will be modular, with the possibility of integrating other add-on devices / sub-devices dedicated to special or specific activities [2].

The types of data captured by these smart devices / sub-devices will be processed, normalized and standardized by the multiaplicative and adaptive mecatronic, cyber-mecatronic and / or cyber-mix-mechatronic system / mother device in formats to ensure interoperability with the real-time monitoring platform [3], [4].

3. THE CONCEPT OF A 3D SMART MECHATRONIC SYSTEM WITH TWO GRIPPERS AND TWO FEELERS FOR MEASUREMENT, INTEGRATED CONTROL AND SMART INDUSTRIAL SERVICES

The conception of the smart 3D mecatronic system with two grippers and two feelers (Fig.1) comprises a multi-complex structure consisting of:
(1) support subsystem for the mechatronic system;
(2) smart mecatronic 3D system;
(3) PC central unit with subsequent monitor;
(4) 3D smart mecatronic control unit;
(5) the barrier system with sensors for protecting the working space of the 3D mecatronic system;
(6) digital display unit of measured data;
(7) 3D feelers for contacting the measuring points of the measuring pieces;
(8) two parts that need to be measured.

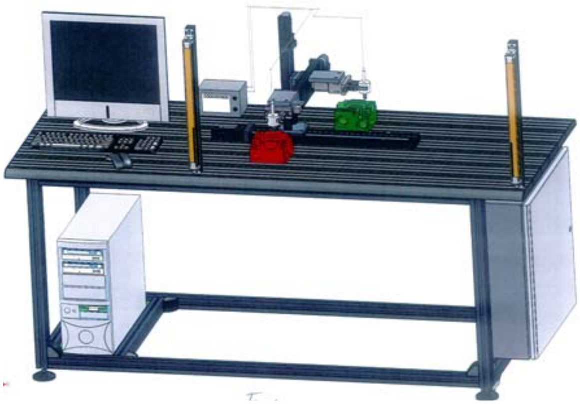

Figure 1. The smart 3D mecatronic system with two grippers and two feelers

● **The support sub-system** is architecturally made from standard aluminium (aluminium collage), which forms a rigid surface for the smart 3D mechatronic system, positioned to create an optimal workspace, a work-desk stiffening scheme, and a planar matrix adjustment of the four support legs.

The support table has a T-channel architecture with multiple possibilities for fastening the smart 3D mechatronic system and the other sub-systems of the mechatronic measuring system itself, including fixing and placing of the parts to be measured.

● **The smart 3D Mechatronic Equipment / System** (Fig. 2) is a complex assembly of three linear electronic axes that matrixes the Cartesian X-Y-Z measuring system and the two grippers of the two 3D feelers.

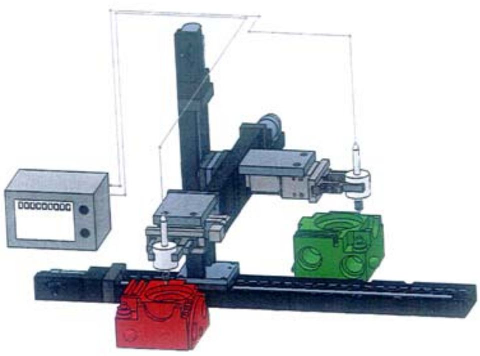

Figure 2. The smart 3D mecatronic system

Each linear electric axis is structured from basic mechanical and guiding elements, actuators, and sensors and transducers. The latter provide smooth movements, high precision for positioning and measurement.

In Figure 3, the mechatronic X-Z sub-system with grippers and 3D feelers is displayed in detail.

● **The two grippers** assembled on the Y-axis have broad possibilities to fix 3D touch pads or parts to be handled in the related process.

Each gripper is in a miniaturized construction that allows precisely driving the "gripping fingers", for the 3D feelers or the parts to be manipulated.

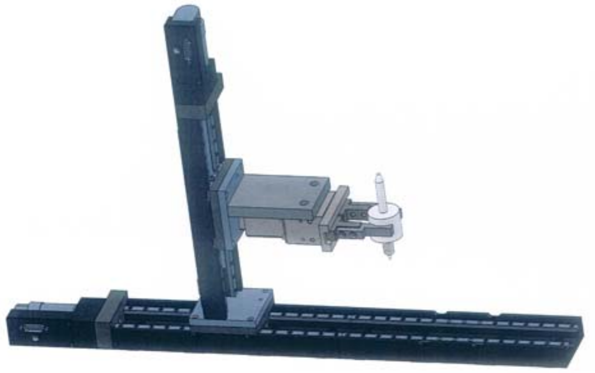

Figure 3. The mechatronic X-Z sub-system with grippers and 3D feelers

● **The two 3D feelers** have a 3-coordinate construction which allows the measuring probe itself to be able to tap three X-Y-X rectangular pieces.

● **The PC Central Unit** (Fig. 4) is in a state-of-the-art architecture with state-of-the-art hardware and specialized software, and developed in the latest generation with a new generation solution monitor. The PC is in permanent dialogue with the command and control unit of the entire smart mecatronic 3D system and synthesizes, processing data from smart measurement processes and all the results of the measurement process.

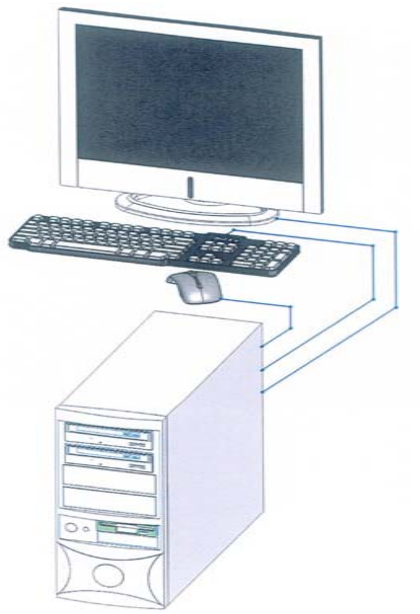

Figure 4. The PC Central Unit

The PC's construction allows integration of the 3D mechatronic system into a remote control and remote maintenance process by integrating it into the cyber space through a remote control and remote monitoring centre.

● **The mechatronic system control unit** continuously ensures the process of control and coordination of the integrated measuring and control process, being in permanent dialogue with the PC central unit. The work area of the integrated measurement and control process is ensured by the sensor barriers of the system (Fig. 5).

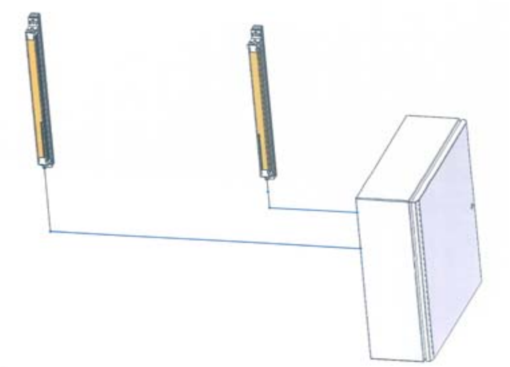

Figure 5. The sensor barrier system

● **The sensor barrier system** (Figure 5) ensures workspace security with the possibility of fully shutting down the 3D mechatronic system when the workspace is disturbed while ensuring the security of the entire 3D mecatronic system without any malfunction occurring.

● **The electronic display unit** ensures the acquisition of the electrical signals of the two 3D sensors from the actual measurement process and the display of the measurement results.

At the same time, the display unit transmits the information to the PC Central Unit for storage and compilation in Smart Measurement Process Databases.

The Smart 3D Mechatronic System, in order to integrate it into a smart cybernetic system, can be integrated with a TV camera subsystem (Fig. 6).

Figure 6. The TV camera subsystem

● The **remote control and remote maintenance centre** ensures the integration of remote control and / or remote monitoring process by associating with cyberspace (WAN Internet and industrial Ethernet) together with passive and active components necessary for this process, through a router.

The concept of this smart 3D Mecatronic Smart Metering System, integrated control and smart industrial technology services enables it to be developed to create other smart 3D mechatronic systems that embrace a simultaneous development with the one presented, forming a "smart multi-complex dual mechatronic 2D system for measurement, integrated control and smart industrial services" (Figure 7);

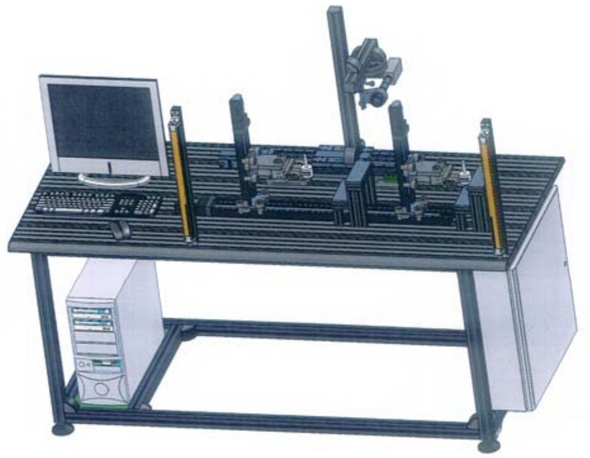

Figure 7. The smart multi-complex dual mechatronic 2D system

This smart multi-complex dual mechatronic 2D system has a matrix architecture consisting of:

● support table subsystem for the "dual mechatronic 2D system";

● two smart 2D mechatronic subsystems, each with a gripper and a 3D feeler, with positioning capabilities in the workspace, depending on the size of the piece being measured;

●TV camera subsystem for "viewing the measurement process" by assisting with continuous process images and transferring them to the remote-control centre through the cyber space;

● the actual workspace barrier subsystem;

● the PC Central Unit subsystem;

● the command and control unit subsystem;

● the gripping subsystems;

● 3D feeler subsystems;

●the specialized software package for measurement, control and service processes.

The structural-functional concept of a smart 3D mechatronic system can expand and develop into complex and multi-complex structures adaptable to industrial processes and industrial environments, until their full coverage is reached and depending on the requirements of quality standards of manufactured products.

Thus, "complex mechatronic and cyber-mechatronic 3D systems" can be designed and realized, with a repetition in the overall construction of their Cartesian axes, in a "tree-like" structure, comprising all the industrial or societal production areas and sections.

Such "multi-complex systems" with 1X, 2X, 3X, 4X, and so on, 2D or 3D axes can be built to cover all smart manufacturing technology spaces, ensuring their quality.

4. THE CONCEPT OF A ROBOT CYBER-MIX-MECHATRONIC SYSTEM WITH REMOTE MONITORING AND REMOTE-CONTROL SYSTEMS

The conception of a robot cyber-mix-mechatronic system (Fig. 8), comprises a complex multi-structure made of the following items: (1) smart industrial robot; (2) cyber-space; (3) remote control & remote monitoring centre.

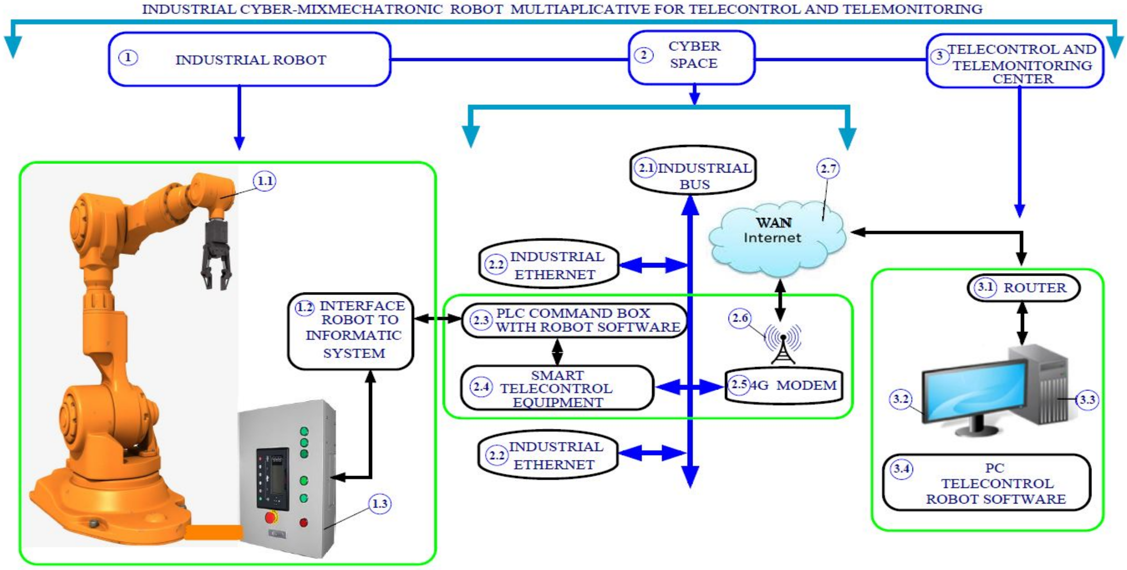

Legend:	1. Industrial robot 1.1 Universal robotic arm (with gripper / 3D feeler) 1.2 Interface between the robot and the informatic environment 1.3 Command tools	2. Cyber space 2.1 Industrial communication bus 2.2 Industrial ETHERNET network 2.3 Programmable PLC with ROBOT software 2.4 Smart devices for remote control and remote communication 2.5 4D GPRS modem 2.6 Internet WAN	3. Center of remote control and remote monitoring 3.1 Router linking to WAN Internet 3.2 PC monitor 3.3 Central unit 3.4 UPC with ROBOT remote control software

Figure 8. The concept of a robot cyber-mix-mechatronic system

- **The smart industrial robot** (Fig. 9) has a complex structure consisting of:
  - the actual robot with a smart arm with a gripper and a 3D feeler;
  - interface between the robot and the informatic environment;
  - command unit with PC.

The robot, through the interface, makes the connection with the PLC and the systems of remote communication.

- **The cyber-space** has a complex structure made of:
  - industrial com bus;
  - industrial Ethernet network;
  - PLC programmed by the software of the robot;
  - smart remote control and remote communication equipment;
  - GPRS 4G MODEM;
  - Antenna
  - WAN Internet.

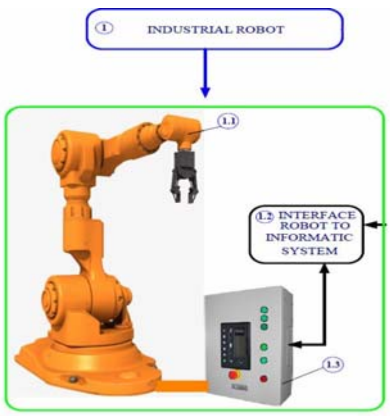

Figure 9. The smart industrial robot

The cyber-space (Fig. 10) makes the connection with the robot via the robot interface and with the centre of remote control via the router of the centre.

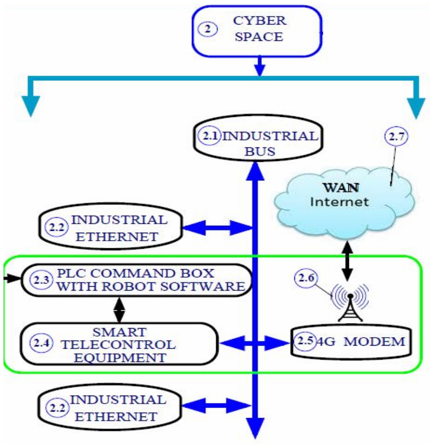

Figure 10. The cyber-space

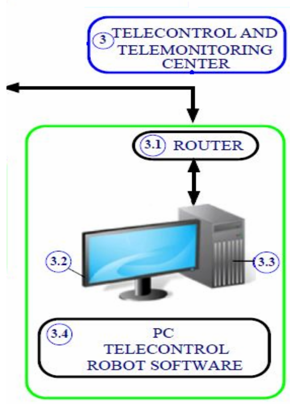

Figure 11. The remote control & remote monitoring centre

● **The remote control & remote monitoring centre** (Fig. 11), has a structure made of:

- router for connecting to WAN Internet;
- PC central unit;
- UPC with remote control robot software;
- the connection of the centre with the cyber-space is made via the router.

As an architectural ensemble, the informational flow of the "cyber-mix-mecatronic robot system with remote monitoring and remote control" goes from "non-electrical" inputs that are transformed into electrical, then amplified, divided and displayed, resulting in "outputs" as a product, service and technology, "a result that can be taken into account as such or can be controlled, monitored or configured remotely through the interconnections of the cyber-space and the remote centre and remote monitoring control.

The cyber-mix-mechatronic robot system with remote control and remote maintenance is used in any industrial or societal process, depending on its constructive and functional integration, in intelligent manufacturing processes, either as such or as remote control and maintenance manufacturing, assembly lines or quality assurance lines.

The robot itself is structurally structured and functional according to the requirements of the process where it is integrated, and in particular in the gripper architecture, so that the robot becomes an "intelligent control equipment" or a "technological and / or service equipment industrial".

In this regard, the gripper can be interchangeable so that it will be the integrator of the "3D feeler" to contact the measuring / control surface of the measuring / controlling piece or the gripper integrator with "fastening, application, manipulation" in application-related technology processes.

5. THE CONCEPT OF A SMART CYBER-MIX-MECHATRONIC DAMPING SYSTEM WITH REMOTE MONITORING AND REMOTE CONTROL

The conception of a smart cyber-mix-mechatronic damping system with remote monitoring and remote control (Fig. 12), comprises a multi-complex structure made of the following items:

(1) smart mechatronic automotive damping system;
(2) cyber-space;
(3) remote control & remote monitoring system.

● **The remote control & remote monitoring system** (Fig. 13) has a complex structure made of:

-electromagnet with coil;
-rheological fluid;
-acceleration sensor;
- acceleration sensor interface;
- high voltage power supply;
- smart remote-control system;
- GPRS 4G modem;
- Antenna.

The mechatronic auto damping system itself connects to cyber space (to the Internet WAN), through the antenna, and via the MODEM to the sensory interface.

● **The cyber-space** (Fig. 14) is represented by the Internet and industrial Ethernet and connects to the remote-control centre via the router and to the mecatronic damping system via the 4G MODEM.

● **The remote control & remote monitoring centre** (Fig. 15) is represented by the PC unit and its monitor, the WAN Internet and PC WAN router with remote monitoring software and remote control for the smart dampener. The remote-control centre connects to the Internet WAN via the router.

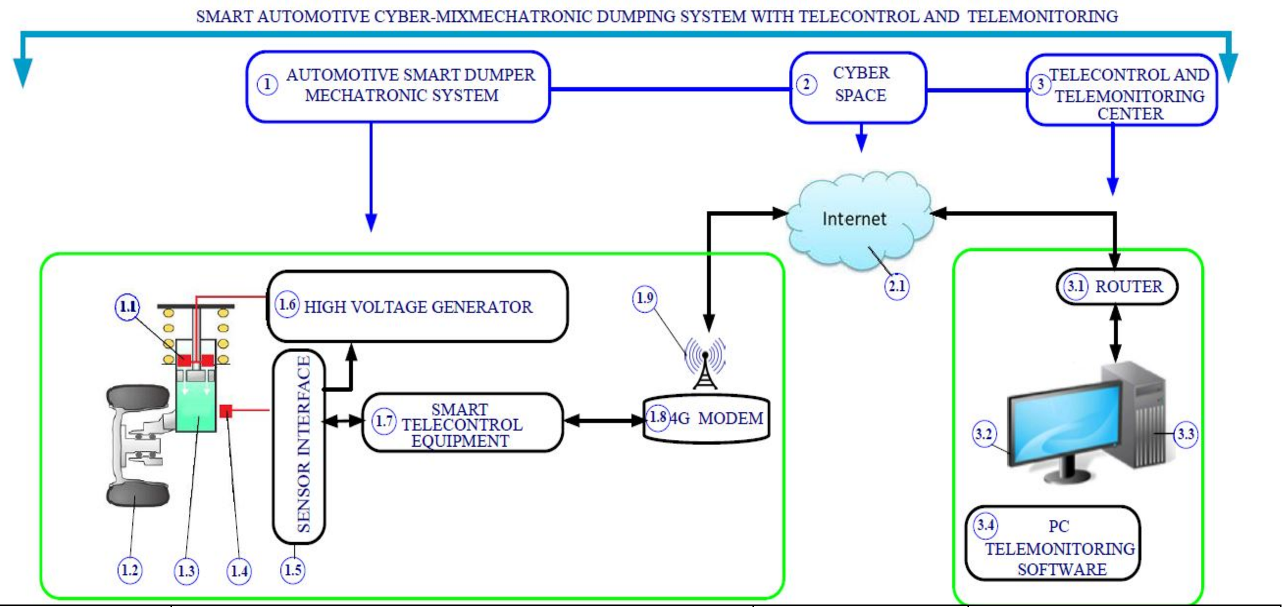

Legend:	1. Smart cyber mix-mechatronic system for dampening 1.1 Electromagnet or coil 1.2 Section of a tire 1.3 Rheological fluid 1.4 Acceleration sensor 1.5 Interface between sensor and acceleration 1.6 High tension source 1.7 Smart remote control device 1.8 4D GPRS modem Antenna	2. Cyber space 2.1 Internet WAN	3. Centre of remote control and remote monitoring 3.1 Router linking with WAN Internet 3.2 PC monitor 3.3 Central PC unit 3.4 PC with software for remote monitoring and remote control smart DAMPER

Figure 12. The cyber-mix-mechatronic damping system with remote monitoring and remote control

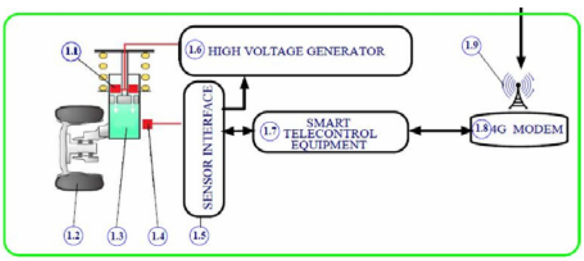

Figure 13. The remote control & remote monitoring system

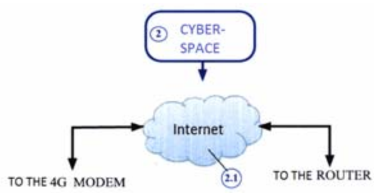

Figure 14. The cyber-space

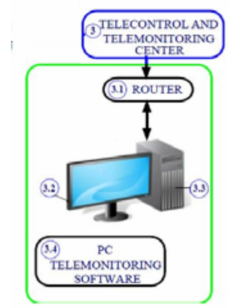

Figure 15. The remote control & remote monitoring centre

In the "intelligent cyber-mix-mechatronic damping system with remote monitoring and remote control" assembly, the **information transfer takes place from system inputs**, of non-electric nature, and transformed into electrical sizes subjected to amplification, division and display processes, to **outputs** of the system, as their final result, as a "product, technology and service" and which can be reported as such or can be controlled, configured and monitored remotely.

5. THE CONCEPT OF A CYBER-MECHATRONIC TECHNOLOGICAL TOOL WITH REMOTE MONITORING AND REMOTE-CONTROL SYSTEMS

The conception of a cyber-mechatronic technological tool with remote monitoring and remote-control system (Fig. 16) encompasses a multi-complex structure made of: (1) robotized fabrication industrial line; (2) human operator with smart integrated tool; (3) cyber-space; (4) remote control and remote monitoring centre [5], [6].

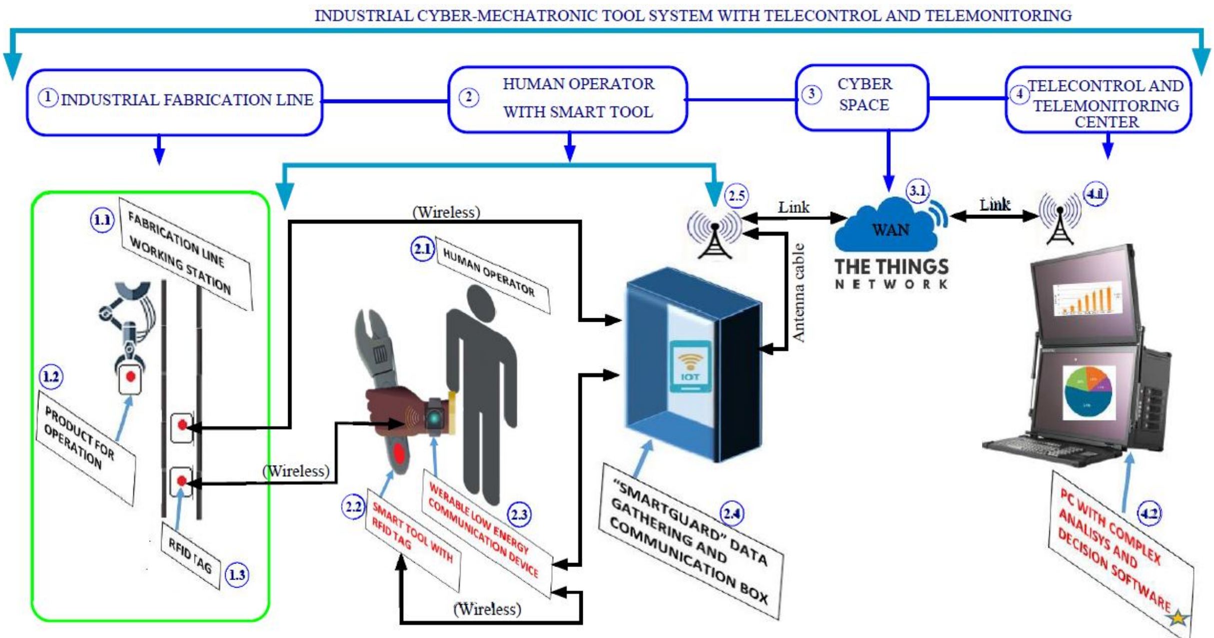

Legend:	1. Industrial manufacturing line 1.1 Workstation on the fabrication line 1.2 Product for technological applications 1.3 Unique identification system with RFID	2. Human operator with smart instruments 2.1 Human operator 2.2 Unique identification system with RFID 2.3 Smart communication and warning bracelet 2.4 Unit with system for data acquisition and communication 2.5 Antenna	3. Cyber space 3.1 Internet WAN	4. Remote control and remote monitoring centre 4.1 Antenna 4.2 PC with software for complex analysis and decision

Figure 16. The cyber-mechatronic technological tool with remote monitoring and remote-control system

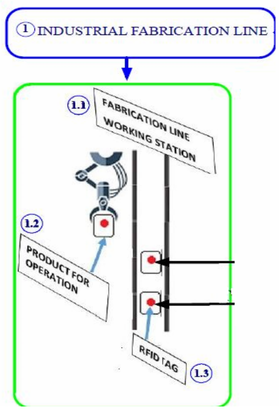

Figure 17. The robotized fabrication industrial line

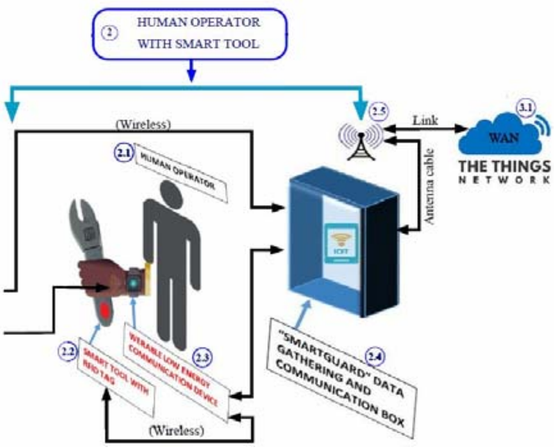

Figure 18. The human operator

• **The robotized fabrication industrial line** (Fig. 17) has a structure specific to the technology subjected to cybernetization, consisting of:

- Technological workstation embedded in the fabrication line;
- Product for technological and specific operations;
- Unique identification system with RFID.

The Robotics Manufacturing Industry Link with Smart Tool is Wireless, Data Collection and Communication.

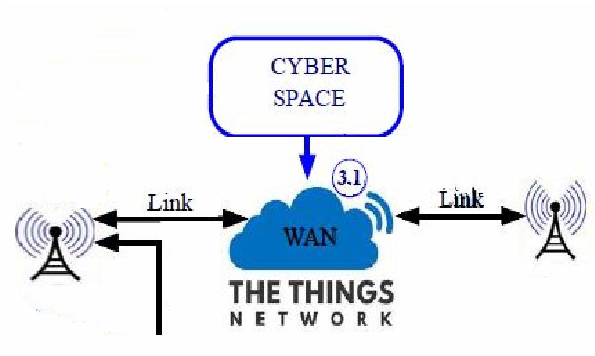

Figure 19. The cyber space

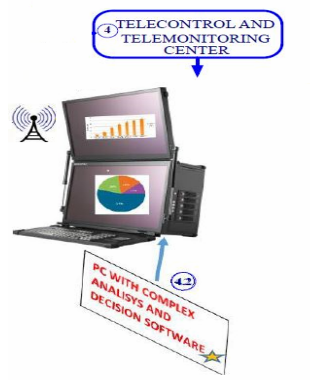

Figure 20. The remote control & remote monitoring centre

● **The human operator** equipped with the integrated intelligent technology instrument (Fig. 18) has on his or her side: a tool with a unique RFID identification system, an intelligent communication and warning barrier, a data collection and communication system and an antenna unit. The connection of the human operator equipped with a technologically integrated instrumental instrument to the manufacturing line is done wirelessly, and with the cyber space is made via an antenna and a link to the Internet WAN.

● **The cyber space** is characterized by WAN Internet (Fig. 19), it is linked to the human operator equipped with the intelligent integrated instrument through the link to the communication equipment (with the human operator) and is connected to the remote control and remote command centre with a link to communication equipment of the centre.

• **The remote control & remote monitoring centre** (Fig. 20) has the following structure: antenna, PC with complex analysis and decision software. As a whole, the "cyber-mecatronic technology remote control and remote control system" **provides the operational deployment** of phases and technological activities based on intelligent process or manufacturing technology through the **integration and connection** of the "smart operator" Which **assists and intervenes** in the process of technical and technological assembly, through its interconnection and decision, depending on the actual development of the process and **which interacts** with the other virtual communication systems **in order to optimize** the automated processes and **ensure their quality** [7].

The communication and transfer of information necessary for the automated or cybernetized process is done through wireless components, facilitating an optimal integration of the human operator with automated and cybernetized systems and subsystems.

In fact, the human operator with the intelligent communication and warning bracelet can be replaced right now or in the near future with a "humanoid robot" that can integrate into the cybernetic process of the industrial process.

6. CYBER-MECHATRONIC LASER BEAM DETECTION SYSTEM FOR A MICRO-SATELLITE NETWORK

Figure 21 presents conceptually an integrated cyber-mecatronic system of measurement by remote laser-distance detection the distance on the orbit between microsatellites placed in a network at distances up to 1 Km and radio communication with the earth station permitting the exploration of scientific applications based on the data transmitted by microsatellites. The action spectrum for electro-optical surveillance and radio covers the areas between the orbits.

The main features of the satellites are:

➢ They move quickly in the sky (typically, they cross the sky above the observation point in a few minutes);

➢ It can detect very small satellites (micro or nanosatellites) that are only visible with very large remote cameras (and therefore very expensive and with a very small field of view).

➢ The radio frequencies that these satellites emit are lower than those emitted by geostationary satellites. For example, typical frequency bands used by LEO satellites are: UHF / VHF (in particular remote meter data), L / S (e.g. meteorological or radio amateur satellites), X (especially Earth observation satellites or military communications).

The radio tracking station is complementary to the optical tracking system. Its advantages over the optical one is:

➢ It can work during times when there is a cloudy sky

➢ It requires the knowledge of the orbit of the satellite with a precision of 10-20 degrees (in the UHF / VHF band) or 1-2 degrees (in the S band), so it can be used in search of satellites with unknown orbit, while a remote end typically, the field has a visibility of about 0.25 degrees.

The disadvantage of the radio station comprises the following aspects:

➢ It cannot detect satellites except in the frequency band for which it was designed

➢ The use of very large antennas and amplifiers leads to low gain and lower signal / noise ratio making it difficult to detect satellites that emit very poorly or are very distant

➢ The radio receiver used must recognize the type of modulation used by the broadcasting satellite

➢ T cannot detect a satellite whose beacon does not cover the antenna or has the beacon closed.

The station has a modular architecture that allows various configurations depending on the intended application and / or the frequency band in which it should work. In the current configuration, the station operates in the UHF band, which allows it to test its performance by detecting and tracking radio transmissions by radio amateur satellites or by scientific nanosatellites.

The following are the mechatronic components of the cyber-mechatronic laser beam detection system for a micro-satellite network (Figs. 22, 23 and 24), [8].

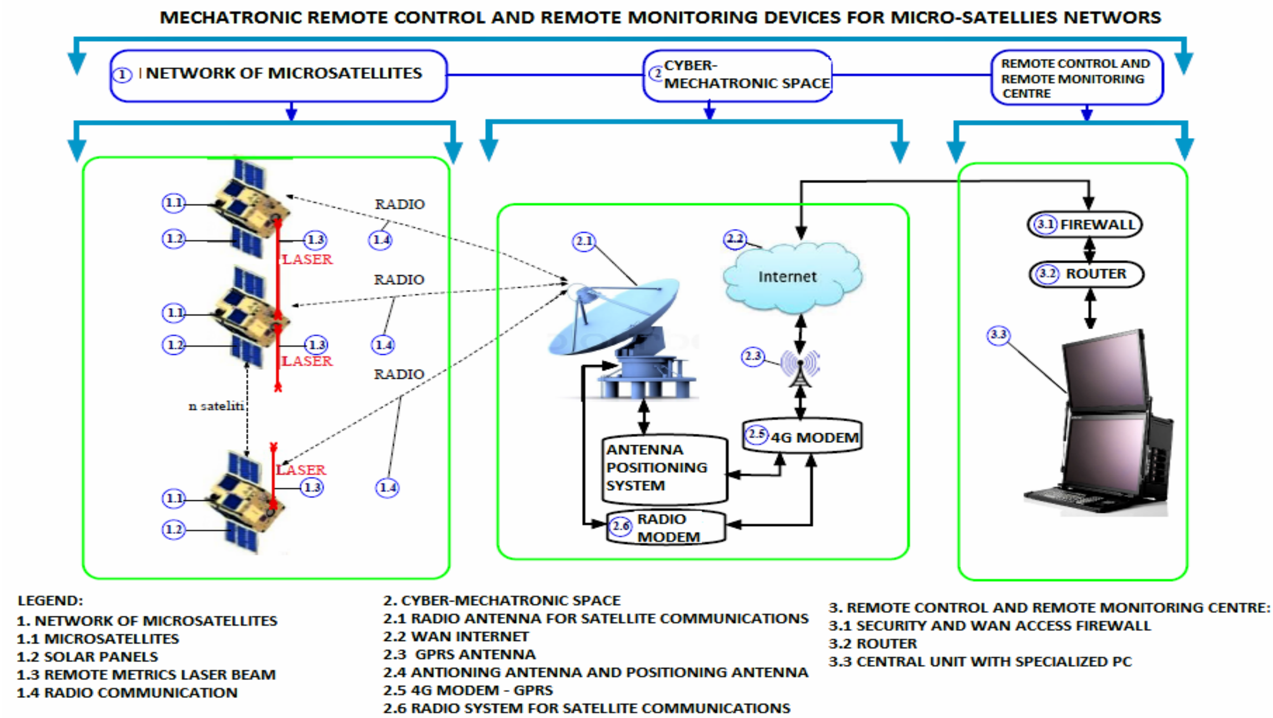

Figure 21. Cyber-mechatronic laser beam detection system for a micro-satellite network

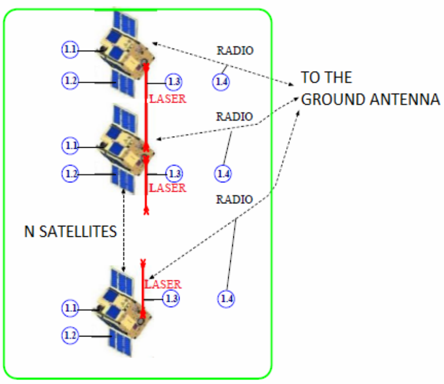

Figure 22. Microsatellites network

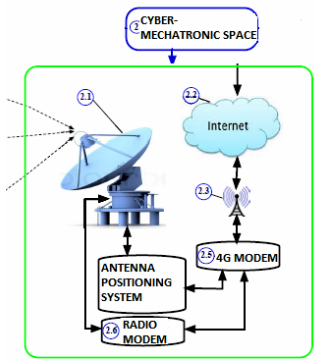

Figure 23. Cyber-mechatronic space subsystem

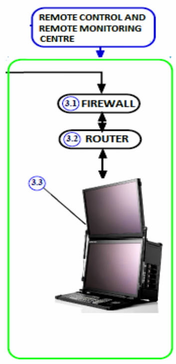

Figure 24. Mechatronic subassembly – Remote Control & Remote Monitoring Centre

In Figure 21 are already identified components of the cyber-mecatronic systemfor controlling a remittance of microsatellites and the connections between these components [9], [10].

In addition to interstellar communication and remote detection in order to determine the distance between them, which is an important parameter in most of the scientific missions encountered by such microsatellite systems, the main components of the terrestrial radio station for the detection and tracking of satellites are:

- the actual antenna, various types and configurations, depending on the frequency band chosen and the type of polarization of the radio signal emitted by the satellite;
- azimuth and elevation motor, made by two mechatronic rotor systems that can be operated independently so that the antenna can be oriented in any direction;
- rotary command-block digital positioning-positioning system including a data processing block and command of satellite antenna automatic orientation;
- the radio modem connected to the antenna output;
- GPRS 4G modem and GPS for automatic synchronization of the system with the GPS satellite watch;
- VSAT modem that provides system communications (optional block if the station is in an area without terrestrial internet infrastructure).

The Azimuth rotor allows a variation of up to 450°, while the Elevation rotor allows a maximum of 180°. For example, **Yaesu G-5500** also allows remote control of the position of one or more unidirectional antennas used for satellite connections and is controlled by two control cables each containing 6 conductors / cable.

The rear panel of the control equipment has 6 Azimuth terminals and 6 elevation terminals with which the rotor communicates with the control equipment.

By using the Network Time Protocol (NTP), you can synchronize the clocks of multiple command centres if you want to integrate other tracking and linking systems with different satellites.

7. CONCLUSIONS

The scientific paper presents the "new complex multiaplicative cyber-mix-mechatronic concept" used in the construction of "ultra-precise 3D remote control and remote monitoring cyber-mix-mechatronic systems" in industrial and laboratory processes.

This new concept and these new cyber-mix-mechatronic systems are a novelty, approaching "vector packs" for mathematical and informational processing both locally and remotely.

In the near future, the scientific work will integrate and develop cyber-mix-mechatronic systems and cyber security subsystems and structures in accordance with ISO / IEC 27.001: 2005 - Information Technology - Security Techniques.

REFERENCES

[1] Gheorghe Gh., Ingineria Cyber-Mix-Mechatronica, Bucureşti, Ed. CEFIN, 2016.

[2] Gheorghe I. Gheorghe, Mecatronica & Sistemele Cyber – Mecatronice, , Bucureşti, Ed. CEFIN, 2015.

[3] Gheorghe Gh., Micronanoingineria Adaptronica, Bucureşti, Ed. CEFIN, 2014.

[4] Gheorghe I.G., Cîrstoiu C.A., Istriţeanu S., Despa V., New Concepts and Solutions of Micro-Nano-Mechatronics and Micro-Nano-Integronics, Annals of DAAAM for 2011 & Proceedings of the „ Intelligent Manufacturing & Automation: Power of Knowledge and creativity”, pp. 77-78, Viena, Austria, 2011.

[5] Machado, J, Soares F., Celina P. et al., A Virtual Workbench Applied to Automation: Student’s Response Analysis, Controlo’2014 – Proceedings of the 11th Portuguese Conference on Automatic Control Vol: 321, Pp. 709-719, 2015.

[6] Machado, J., Campos, J. C., Sevcik, L. et al., Development of Dependable Controllers in The Context of Machines Design, Modern Methods of Construction Desig n, pp:125-131,2014.

[7] Zhou, K., Ye Cen, Wan J., Liu B. and Liang L.: Advanced Control Technologies in Cyber-physical System, 5th International Conference on Intelligent Human-Machine Systems and Cybernetics (INMSC), 2013.

[8] Silva M.; Pereira F.,Soares, F. et al.,An Overview of Indust rial Communication Network, New Trends in Mechanism and Machine Science from Fundamentals to Industrial Applications, Vol. 24, pp: 933-940, 2015.

[9] Saikalis G. et al., Virtual Embedded Mechatronics System, SAE Technical Paper, 2006.

[10] Lee E. A. Cyber-physical systems design challenges, International Symposium on oriented items/ components/ services distributed using real-time computational technique (ISORC), Orlando, FL, pp. 363-369, 2008.

The Scientific Bulletin of VALAHIA University
MATERIALS and MECHANICS –Vol. 15, No. 13

DOI 10.1515/bsmm-2017-0020

INTELLIGENT 3D VIDEO-LASER SYSTEM FOR MEASURING DISTANCE AND AVOIDANCE OF OBSTRUCT OBSTACLES INTEGRABLE INTO ROBOTIC PLATFORMS

Dorin ANGELESCU, **Gheorghe Ion GHEORGHE**

Valahia University of Târgovişte - Mechanical Engineering Doctoral School, Targoviste, Romania

E-mail: dorin.angelescu@incdmtm.ro

Abstract. *Outcome of the scientific concerns from the Doctoral School of Mechanical Engineering and Mechatronics at Valahia University of Târgovişte in the field of unconventional measurements using non-contact laser technique, the scientific work "Intelligent 3D video-laser system for measuring distance and avoidance of obstruct obstacles integrable into robotic platforms" is a work in progress being in the experimental phase of single-channel testing. The system is designed for robotic platforms for special interventions in high-risk work environments, with the main goal of an active, real-time 3D spatial stereo interface for the operator who manages the robotic platform remotely. 3D imaging and real-time measurements of distances provide the operator of the robotic intervention platform with the ability to perform extremely precise maneuvers. The scientific work ultimately results in an intelligent integral system that can predict the emergence of an obstacle to the robotic platform movement, thus determining the distance in real time to it. The measuring distance is between 0 m - 40 m, with an accuracy of +/- 0.5 cm being synchronized with the video system with a clear visual area from 0.05 m to infinity. The 3D video laser system can simultaneously shoot movie or single images of the obstacle, storing data in 3D, photo or video digital formats, both locally in non-volatile memory or externally thru any GPSR network to the operator and / or to a control center. In later development, the measurement system will be coupled to a GPS network for auto location of position and architected with a self-defense and offensive module mounted on the mobile robotic platform. Thus, this complex project combines in a unified knowledge of Mechatronics, Integronics, Cyber-Mix Mechatronics, Artificial Intelligence and Information Technology.*

Keywords: *Integrated 3D System, Laser Measurement, Intelligent Technology*

1. INTRODUCTION

The scientific work has gone from a set of requirements and technical characteristics resulting from a complex market study that covered the vast majority of areas where such systems can be used or even produced in the event of switching to serial production [1, 2]. This system is part of a more complex work, actually a part of a complex mechatronic robotic platform with direct application in security and surveillance activities [3]. The robot will be used in order to avoid human loss in complex and dangerous situations.

The system presented in this paper is the practically the vision and orientation part of the robotic platform interfaced with the operator. Video and measurements, as accurate as possible, are creating a precise virtual reality transmitted remotely in real time to the operator which will be able to execute complex operations without being near the danger zone [4, 5].

The most important role of the intelligent 3d video-laser system is to transmit to the operator all "on site" data, extremely precise and in real time [5]. The 3D vision must be as accurate as possible so it is doubled with a precise laser measurement module in order for the operator to estimate as precise as possible the distances to the obstacles as well as distances to the objectives to which the operator intervenes through the robot (for example artisanal bombs, strange parcels etc.).

2. PRESENTATION

2.1. General presentation

Thus, we can list some of the features of the intelligent 3d video-laser system. The Laser Module must be equipped with a laser that must be Class 1, ensuring maximum safety for the eyes. The wavelength of the laser is 905 nm (ensuring both eye protection and as little interference with ambient light as possible). The measuring distance range should be between 0m and 40m. The accuracy is ± 0.5cm and the displayed resolution on the screen is ± 0.001m. The data can be measured both in meters and in miles or yards through a selectable system. The system must also have the electronic compass function prepared to be integrated with a future GPS auto localization system of the robotic platform. The supply voltage, strictly related to the portability of the instrument is a dual 9Vdc and 5Vcc sources, made by means of two batteries respectively on the laser module (9Vcc) and on the data processing and display modules(5Vcc). Power supplies are rechargeable battery type.

The display side is integrated with a PiTFT 480x320 3.5" TFT + Touchscreen LCD, the operating controls being also included in this way thru software touch buttons on screen. The image of the object to be measured will be displayed in real-time on the color LCD display simultaneously with the measured values and data. The camera uses a video camera that captures the image through a Video-lens ensemble formed by a modified 50 mm/2 Olympus lens system. The clear adjustments of the optical system, synchronized with the measuring point, are providing the operator with a clear and sharp view of between 50 cm and infinity. The Video-lens ensemble has the best quality BaK 4 (Schott glass) and anti-reflective FMC coatings.

The optical system provides the distance information of the measured element (being or not an obstacle), displaying in real time the images captured by the optical device. The user-selectable measured values are also displayed over the image itself. The system is provided with the ability to capture real-time pictures or movies of the measurements/activity of the robotic platform actions, in the real-time context and to record the history of all measurements/activities on a non-volatile SD / MMC / SDIO card. The system will be able to use the GPRS system to use IOT-like functions for transmitting real-time measured data and video to any location or measurement lab. The system is especially designed as an open system, which can be further improved at a later stage by coupling to GPS satellite systems both for auto-positioning and more precise geo-position of the measured element.

2.2. Component elements and analysis

The intelligent 3D video-laser system is conceived as an “open system” in order to be able upgradable and reconfigurable for future improved versions. It is realized with mostly OEM modules interconnected thru a strong Central Computing System and controlled by dedicated software. The system consists of 7 main OEM modules interconnected to each other according to the block diagram shown in Figure 1.

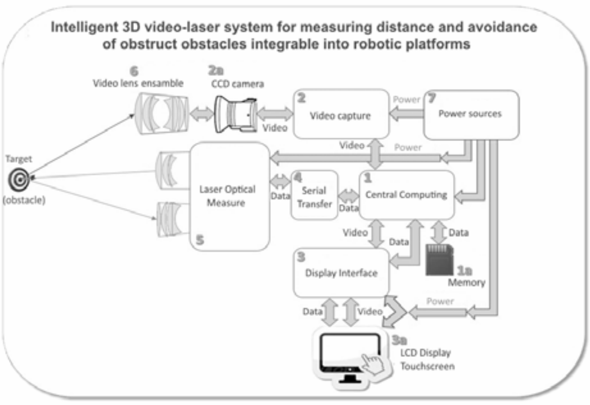

Figure 1. Block diagram

Modules are reprogrammable and controllable by software via the Central Computing System (1). This approach was chosen because of the particular elasticity of such a structure in terms of the functions required for the operation in the desired regime, but also for the enormous possibilities of reconfiguration / upgrading with new functions that will prove necessary in the future. Thus, the software configuration will direct the flow of information transmitted by the block (5) via the reformatting and serial transfer block (4) to the central computing system (1). Synchronously with this data stream, via the module (6) the target image is optically transferred to the module (2a, 2) to the video capture module, thus creating another set of video image data. This stream will enter the Central Computing System (1) and will be transferred through the display interface (3) to the LCD display (module 3a). Thus, in graphical memory and implicitly on the screen, we will have the two types of information shared in graphical windows, respectively the calculated data related to the measurements made and the actual image of the measured target/obstacle. At this level, capture of non-volatile data will also be performed. Nonvolatile memory (1a) is an SD / MMC card. This includes operating system, interfacing software, and signal formatting software, data computing software, and saved data.

The LCD screen (3a) will also be the operator interface with the system via the existing touchscreen and a mouse or joystick. Modules 1, 1a, 2, 2a, 3, 3a, 6 will be doubled for the final 3D stereo version. A more realistic Fritzing diagram is shown in Figure 2.

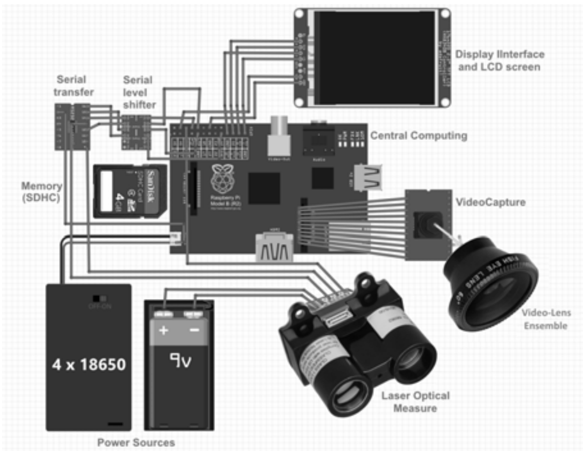

Figure 2. Fritzing diagram - the hardware interconnection of the modules

The modules presented are analysed below, as the prototype is now as a work in progress in the testing phase. Further modifications could be done until the final stereo version of the system. The intelligent 3D video-laser system is composed from the following modules:

Central Computing module ● Due to the large amount of information processed and the need to manage a very powerful graphical interface for real-time image processing, the system is grouped around an ARM 1176JZF CPU with 512 G RAM and Broadcom Videocore IV video card (with Open GL functions). The PI OEM computing system uses as a operating system a free and dedicated Linux distribution Raspian open source (ver.150312).

The central computing system has the following ports available:
• USB = 2 - USB 2.0 ports;
• Video Output = Composite RCA and HDMI;
• Audio Output = 3.5mm and HDMI;
• Non-volatile memory = SD / MMC card slot;
• Network Port = 10/100 RJ-45;
• Low signal peripherals = 8 × GPIO, UART, I²C bus, SPI bus with two select chips;
• Camera port = Micro-camera type RAS-33;

This has ensured great connectivity with the rest of the hardware, all reducing to the way they are configured, controlled, and used only by using specific software components to accomplish all the desired functions. The software is made in C ++, Java and Python. Such a system has the great advantage that it can be configured, changed, modified and further upgraded with new features and utilities that will be the subject of future system upgrades, as decided in the original theme. It thus becomes an "open" system to almost all the foreseen or unforeseen later ideas.

This module enables, via an existing HDMI port, its synchronous pairing with the 2.8 "LCD display to a large display or TV for ease of work in the concept phase or later for reprogramming, reconfiguration, or downloading and viewing data on non-volatile SD / MMC / SDIO card type.

Video capture module ● The Central Computing module also connects with the RAS-33 micro-camera interface. The communication is made on the separate port, thus releasing the serial port RS232 required for processing the measurement information. The micro camera is HD (High Resolution) with a 5 Megapixel sensor. This allows to capture images with any resolution up to 2592 pixels x 1944 pixels, and the video files have all HD format with 1080p or 720p resolutions. The high-speed, configurable software (OpenGL) interface is particularly fast, providing real-time viewing of the target with a frequency of over 24 frames per second, providing a smooth view of the image and adjacent information displayed on the screen (measurements and separate indications of the interface). Moreover, it can quickly manage the execution of rescue functions (frame or video stream-saving) on the non-volatile SD / MMC / SDIO card type. Thus, at the end of the activity of the robotic platform all video and data will be available, if required.

Interface / Display module ● The system must be 3D so it must use stereo images for the operator. The actual work in progress uses only one video channel, being extremely easy at the end of the tests to reproduce the second channel (being identical). We have decide to use separate channels for the stereo images so the left and the right channels will be identical but completely separate in order to assure the best frame rate possible for the visual comfort of the operator. On future progress of work there are also provided separate transmission GPRS channels, taking into account the same reason. Therefore it has been decided to use a 2.8 "TFT colour LCD 320x240 pixel 16-bit colour display (easily to integrate into future 3D glasses or 3D helmets). It uses a high-speed SPI interface on the SC system with a separate controller for the Broadcom IV Video Card. The video card, in this context, provides the information taken from the camera and from the measurements into real-time flow as planned. There will be displayed both the measured values and the real-time image of the measured target (16-bit colour) on the synchronous LCD (in a dedicated design interface). A screen containing a capacitive touchscreen has been chosen in order to minimize the number of mechanical buttons in this test phase, (the optimal number, shape and functions of the buttons will be determined in the final phase of the project for better ergonomics and ease of use). There are at this stage a number of buttons strictly required for operation:
- Soft button to start the measuring program;
- Soft button to exit the measurement program;
- Software Configuration Test Hardware Button;
- Frame/frames-saving button for target image;

Certainly, additional buttons may appear during tests depending on other events or actions or applications that will be considered interesting and useful to the operator. It is also possible to talk about an interface open to almost any subsequent buttons upgrade, of course with limited positions per page (window) according to the actual dimensions of the screen, in the context of its surface accessibility and visibility.

These buttons will be operated by using a mouse or joystick like device. In this phase the touch screens are available to finger touch but in the future (integrated into 3D glasses or helmets) it won't.

Serial Transfer module ● Two-way conversion of the 5V / 3V serial TTL signal is required to provide data transfer between Laser Optical Measure and the Central Computing System. This ensures the transfer of data between the two modules and their coherent reformatting ensuring high transfer speeds.

Laser Optical Measurement module ● This SEN-14032 OEM module contains the optic part made up of two anti-reflective double-coated optical systems for the laser pulse emission and laser pulse receiver. The information received by this module is transmitted via the Serial Transfer System to a serial input of the Central Computing module. From here, the central computing system, using a specialized software (done in C ++ for the PC connection), takes control over these data, processes and makes it available to the various peripherals (PC computer, LCD screen, SD card) used by the operator.

Video-Lens Ensemble module● To ensure a good target visibility, the lens ensemble is formed by a modified 50 mm/2 Olympus lens system and a real field of view of 60 degrees (wide) and FMC coatings. This is required both to have a better image of the target and to reduce light disturbances from side light sources. The system has a clear view within a range from 0.5m to infinity.

Power Supply module ● The system has a dual power supply. A stationary power supply module from 220 Vca / 50 Hz and a portable battery type supply. The stationary module provides an output of 9 VDC and a 5 VDC output. The portable module consists of a 5V / 12A and 9V / 890mA battery.

2.3. Soft and Interface (Beta version)

For easier realization and miniaturization, OEM configurable software modules have been used through micro PI (Raspberry PI) computing platforms.

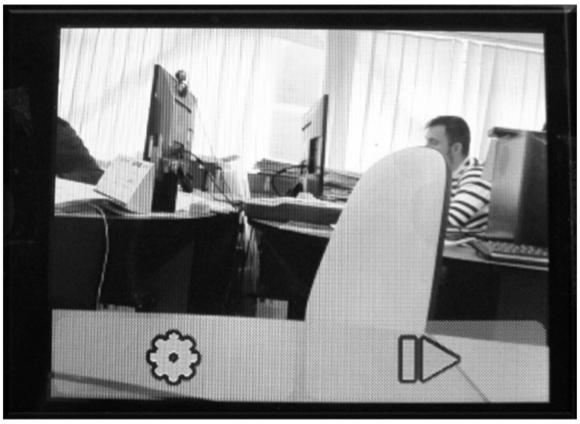

Figure 3. Main Menu LCD screen

The modules are in most cases interconnected with flexible connections and ribbons, allowing the boards to be arranged and assembled as ergonomically as possible and in as little volume as possible. Thus, the entire system is expected to not exceed the size of 100X90x70mm (mono version).

Figure 4. Main Menu PC (serial port selection)

At this point we are in the testing and experimentation phase of communication between modules. The graphical interface already has a first shape and can control the process of acquiring images and movies as well as managing the stored database. Figures 3, 4, 5, 6 and 7 show sequences from the main menu (beta version) for LCD screen, and sequences from the main menu for the PC measuring part.

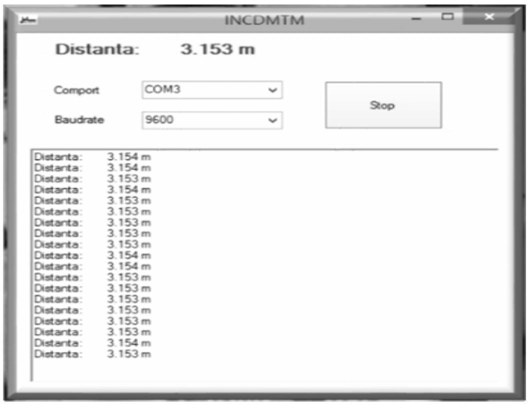

Figure 5. Main Menu PC (distance measurement interface)

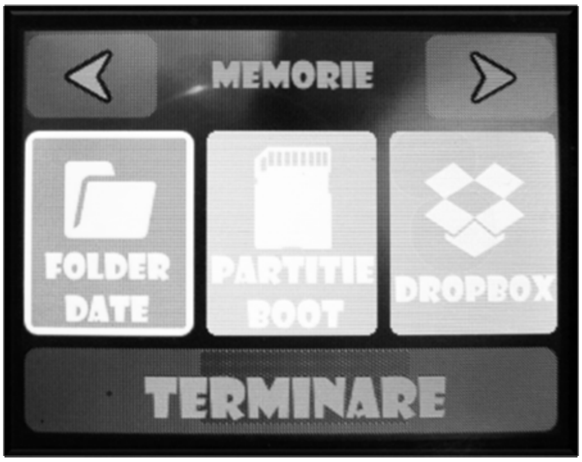

Figure 6. Main Menu LCD (storage options)

The interface already has an IOT connection type option, currently under laboratory conditions using the Internet thru UTP connection and using the Dropbox facility to complete the transfer functions and formats.

Figure 7. Main Menu-LCD (exit menu)

The GPRS part is not yet implemented and will be added later. Also, the transfer and display functions were completed on a Windows interface and, at the end of the

PC tests, ported on RaspianPI.
All software is Beta testing version, and are continuously modified and optimised according to effective tests results.
The mechanical part of the system was made in SolidWorks format .stl specially configured for 3D print execution on the existing printer, the OBJET 3D Stratasys (Figure 8).

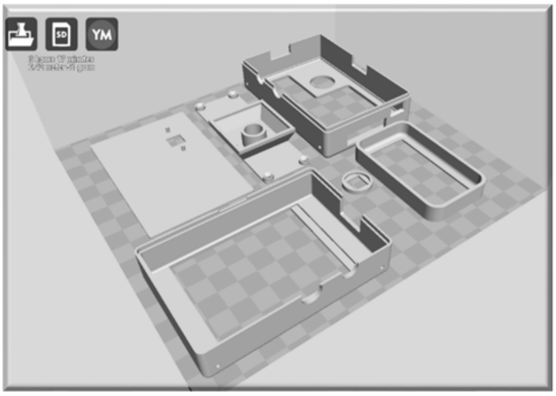

Figure 8. Housing of the central computer system and camera

This being partial forms of the cases, dedicated to testing actions and not for the final versions. Plastic was used because of the low mass, which is desirable for the entire system assembly at least in this prototype phase. It has also been taken into account, for the future development, the possibility of executing versions of cases suitable for future possible environments and high operating conditions.

3. CONCLUSIONS

Although we cannot yet finalize the final conclusions in the true sense of the word, given that the system is still in tests, we can still make some pre-conclusions. Thus, it can be said that the system itself, the modules used and the basic idea from which it was started are correct and functional. It can be said that the system can not only be completed in the proposed parameters but also improved later (not only with GPS module and functions).
At the same time, as the scientific work evolves, new adaptations and improvements are emerging, which confirms that its original concept is well-chosen and can look optimistic towards a swift and correct completion. The final conclusions will really be at the end of the scientific work which will be the subject of another scientific paper.

REFERENCES

[1] Eben Upton and Gareth Halfacree, Raspberry Pi User Guide 2nd Edition, John Wiley & Sons Ltd., The Atrium, Southern Gate, Chichester, West Sussex, PO19 8SQ, United Kingdom, 2014.

[2] Gheorghe Ion Gheorghe, Anghel Constantin, Sergiu Dumitru, Microingineria Mems & Nems Inteligente, Editura CEFIN, Bucuresti, Romania, 2013.

[3] Gheorghe Ion Gheorghe, Adaptronica Sistemelor Inteligente, Editura AGIR, Bucuresti, Romania, 2014.

[4] Matt Richardson and Shawn Wallace, Getting Started with Raspberry Pi. Published by O'Reilly Media, Inc., 1005 Gravenstein Highway North, Sebastopol, CA 95472, United States of America, 2013

[5] Gheorghe Gheorghe, Simona Istriteanu, Veronica Despa, Alexandru Constantinescu, Adrian Voicu, Mechatronics, Integronics and Adaptronics, Bucharest CEFIN Ed., 2012.

[6] Cay Horstmann and Rance D. Necaise, Python for Everyone, John Wiley & Sons Ltd., The Atrium, Southern Gate, Chichester, West Sussex, PO19 8SQ, United Kingdom, 2014

[7] Y. Daniel Liang, Introduction to Java Programming 8-th edition, Pearson Higher Education. Upper Saddle River, New Jersey, 07458, 2011

[8] Gheorghe Ion Gheorghe, Carmen Adriana Cirstoiu, Simona-Elena Istriteanu, Veronica Despa, New concepts and solutions of micro-nano-mechatronics and micro-nano-integronics, Annals of DAAAM & Proceedings, 2011/1/1

[9] Adrian Voicu, Gheorghe Gheorghe, Liliana Laura Badita, Adriana Carmen Cirstoiu, 3D measuring of complex automotive parts by multiple laser scanning, Applied Mechanics and Materials, 2013.

[10] Gheorghe Ion Gheorghe, Anghel Constantin, Iulian Ilie, New Cyber-mixmechatronic Concept for the Realization of Smart Cybernetic Systems with Applications in the Industry, Economy and Society Scientific Bulletin of Valahia University - Materials and Mechanics, ISSN (Online) 2537-3161, No. 11, Vol. 14 / 2016.